HIGH THROUGHPUT CHARACTERIZATION OF CELL RESPONSE TO POLYMER BLEND PHASE SEPARATION

A Dissertation
Presented to
The Academic Faculty

By

Pedro José Zapata B.

In Partial Fulfillment
of the Requirements for the Degree
Master of Science in the
School of Chemical and Biomolecular Engineering

Georgia Institute of Technology
July, 2004

HIGH THROUGHPUT CHARACTERIZATION OF CELL RESPONSE TO POLYMER BLEND PHASE SEPARATION

Approved by:

J. Carson Meredith, Advisor

Mark R. Prausnitz

Andreas S. Bommarius

July 07. 2004

ACKNOWLEDGMENTS

As with most of the graduate students close to finish their thesis, I waited until the very last minute to write this section. And while it may seem as a sign of laziness, it represents maybe the most difficult episode of the entire work. There are so many people to thank that I'm sure I will forget some. Anyway, here I go:

First of all, I would like to thank my advisor Dr. J. Carson Meredith. His orientation, unwavering support, and especially, his infinite patience were essential during the course of this work. I have never met anybody with more broad-ranging knowledge and interests. I have to say that his enthusiasm to custom build every single piece of equipment needed in our lab is contagious and makes you feel it is possible to do everything you want to do, you just have to try.

I would like to thank all the members of the thin-film and colloid research group. To Joe-Lahai Sormana, the best yahoo pool "runner-up" I've ever seen, thanks for all the laughs and "free" entertainment provided during these years, although I still believe you should *not* consider a professional singer career. Krishna Tej Marla whose impressive physical insight is only matched by his affinity for chemical potentials, and that alone is worthy of respect. I expect one day he, or his wife to be precise, can teach me how to prepare fine vegetarian dishes. A especial note goes out to one of the world's most infamous postdocs, Dr. Santanu Chattopadhyay. He alone has enough titles for the rest of our group to become MS, PhD or even postdoc. Unfortunately, for us of course, marriage has stopped his fabulous career in search for his n+1 postdoc title. For him my warmest regards and sincere wish that he has a wonderful life in company of his wife. Jing Su, who, to my knowledge, is the only biomedical researcher that masters more programming languages than a computer science engineer. I'm very grateful for all his

detailed explanations about cells and bioengineering. To the rest of the group a million thanks, and to all the group my most sincere wishes that you have unimpeded progress to successful careers here and beyond the halls of GeorgiaTech.

I'm also very grateful with Dr. Andrés García and the members of his group for all their support, and for allowing me to use their research facilities throughout the course of this work. Special gratitude goes to Benjamin Keselowsky and Kristin Michael for bearing the thousands of questions I asked every single time I stepped inside their lab. Without their help I would be still wandering in the lab trying to figure out what to do, and this thesis would not have turned out the same way.

I would like also to acknowledge Dr. Andreas Bommarius and Dr. Mark Prausnitz for being part of my committee.

My most special gratitude, however, goes to those without whom this would not have been possible whatsoever: My parents. Gracias por su amor y apoyo incondicional, sin ellos este logro no habría sido possible. Ustedes han sido, son, y serán siempre mi más grande inspiración. My brother, and exceptional person in every single way and my role model, "gracias monín". Gladys, gracias por su paciencia infinita durante estos 24 años y por ser parte de nuestra familia. And Hélène, thanks for your encouragement, thanks for your endless motivation, thanks for listening, thanks for being an inspiration, but specially thanks for being part of my life, "Gros bisous".

TABLE OF CONTENTS

	Page
Acknowledgements	**iii**
List of Tables	**ix**
List of Figures	**x**
Summary	**xviii**
Chapter I: Introduction	**1**
Chapter II: Background and theoretical basis	**8**
2.1. Overview	8
2.2. Background	9
2.2.1. General concepts about cells and ECM	9
2.2.2. Cell adhesion and spreading	11
2.2.3. Cell-surface interactions	13
2.2.4. Biomaterials	15
2.2.5. Degradable polymers	17
2.2.6. Degradation, erosion, biodegradation, bioerosion	19
2.2.7. Degradable polymeric biomaterials	19
2.2.7.1. Poly(lactic acid) and poly(glycolic acid)	22
2.2.7.2. Polycaprolactone	24
2.2.8. Polymer blends	25
2.2.9. Combinatorial methods and high throughput screening techniques	27
2.2.9.1. Composition-gradient libraries	28

2.2.9.2. Thickness gradient libraries 30

2.2.9.3. Temperature-gradient libraries 30

2.3. Theoretical basis (polymer blends) 31

2.3.1. Thermodynamics and phase behavior of polymer blends 31

2.3.2. Phase separation, UCST and LCST 36

References 48

Chapter III: Preparation and characterization of pcl/pdla polymer blend thin film libraries 53

3.1. Introduction 53

3.2. Experimental methods 58

3.2.1. Composition-gradient library preparation 58

3.2.2. Temperature gradient libraries (annealing) 64

3.2.3. Characterization of temperature/composition libraries 68

3.2.3.1. Ellipsometry 68

3.2.3.2. Fourier transform infrared spectroscopy (FTIR) 69

3.2.3.3. Atomic force microscopy (AFM) 70

3.2.3.4. Cross polarized optical microscopy 70

3.3. Results and discussion 71

3.3.1. Library film thickness (ellipsometry) 71

3.3.2. Library composition (FTIR) 73

3.3.3. Library surface roughness (AFM) 79

3.3.4. Microdomain geometry and distribution characterization (cross polarized optical imaging) 87

3.3.4.1. Image enhancement 88

3.3.4.2. Image analysis 91

3.4. Summary 103

3.5. Conclusion 104

References 105

Chapter IV: Effect of PCL/PDLA libraries surface topography on cell behavior 107

4.1. Introduction 107

4.2. Materials and experimental methods 110

4.2.1. Cells 110

4.2.2. Cell culture 111

4.2.3. Bioassays 113

4.2.3.1. Cell adhesion and spreading (morphology) 114

4.2.3.2. Cell proliferation 116

4.2.3.3. Protein expression 119

4.2.3.3.1. Alkaline phosphatase expression 119

4.2.3.3.2. Osteocalcin expression 120

4.2.3.4. Mineralization 121

4.2.3.5. Viability 121

4.3. Results and discussion 122

4.3.1. Cell attachment and morphology 122

4.3.2. Proliferation 131

4.3.3. Protein expression and mineralization 143

4.3.4. Cell viability 149

4.4. Summary 150

4.5. Conclusion 151

References 152

Chapter V: Conclusion 158

Chapter VI: Recommendations and further work **160**

Appendix A: Polymer blend mass balance **163**

LIST OF TABLES

Table 2.1. Applications of synthetic materials and modified natural materials in medicine.

Table 2.2. Half-life of some classes of polymers.

Table 2.3. Mechanical properties of some degradable polymers.

Table 4.1. Biological reactions to topography.

Table A.1. Initial values for the mixing step of the combinatorial library preparation procedure.

Table A.2. Calculated rates based on the initial values presented in table A.1 (infusion rate equals the average between the sampling and withdrawal rates, as stated in section 3.2.1).

Table A.3. PCL and PDLA mass fractions inside the mixing vial as a function of time.

Table A.4. PCL and PDLA relative mass fractions after film casting.

LIST OF FIGURES

Figure 2.1. Cell-substratum contact sites. a) Focal adhesion points, strong adhesive sites, are mainly found at the boundaries of cellular extensions. The integrin connects the cytoskeleton with the substratum via fibronectin. b) Close contacts (less strong adhesive sites). c) Localization of the different adhesive sites. MF: microfilaments, M: cell membrane, AP: adhesive protein, FN: fibronectin, ECMC: extracellular matrix contact, C: close contact, F: focal adhesion.

Figure 2.2. Cell spreading as a function of substratum surface free energy (γ_S, wettability). Dotted line represents cell spreading in the absence of proteins. Solid line represents cell spreading in the presence of serum proteins.

Figure 2.3. Chemical structures of degradable polymers.

Figure 2.4. *In vitro* degradation of PGA. Retained tensile strength vs. time. Without its unique crystalline behavior, PGA would degrade much faster.

Figure 2.5. *In vitro* degradation of L-PLA. Retained tensile strength vs. time.

Figure 2.6. *In vivo* degradation of absorbable sutures. PDS® and MAXON® are commercial PLA-PGA sutures.

Figure 2.7. Representation of the preparation of composition-gradient libraries using the gradient-film coating technique.

Figure 2.8. Representation of the method to prepare thickness-gradient libraries. The substrate is moved with a particular acceleration rate to create a gradient in film thickness.

Figure 2.9. Dependence of the Gibbs free energy on the composition (at T and P constant).

Figure 2..10. Temperature vs. Composition diagram showing binodal and spinodal regions determined by different stable, metastable and unstable states. One-phase region = outside binodal region. two-phase region = inside binodal region.

Figure 2.11. Entropy of mixing as a function of composition (cellulose acetate–cellulose nitrate mixture).

Figure 2.12. Lattice model of a polymer mixture. Structure units of equal size.

Figure 2.13. Formation of new contacts of the type A-B after mixing pure components A and B.

Figure 2.14. Multiple molecule-molecule interaction representation (mixture AB, pure component B and pure component A). Cohesive energy density model.

Figure 2.15. Schematic diagram for a polymer blend that exhibits upper critical solution temperature behavior (UCST).

Figure 2.16. Schematic diagram for a polymer blend that exhibits lower critical solution temperature behavior (LCST).

Figure 2.17. Temperature dependence of the interaction parameter: curve (1), contribution due to contact energy dissimilarity; curve (2), contribution due to free volume dissimilarity; curve (3), χ_S for mixtures with UCST *and* LCST. Dashed line corresponds to χ_C.

Figure 2.18. Mechanisms of phase separation: Nucleation and growth (top) and spinodal decomposition (bottom).

Figure 3.1. a) Strain-at-failure of PCL-PDLA blends as a function of composition. b) Yield stress as a function of blend composition for a PCL/PDLA polymeric blend.

Figure 3.2. Plot of Young's modulus as a function of PCL/PDLA blend composition (solid line). Kerner-Uemura-Takayanagi model: assuming perfect adhesion (dotted line) and zero adhesion (dashed line).

Figure 3.3. LCST cloud point curve for the PCL/PDLA system. One-phase region below LCST boundary (parabola-like curve). Two-phase region above LCST boundary.

Figure 3.4. Schematic of the polymer gradient mixing procedure (A→PCL, B→PDLA).

Figure 3.5. Illustration of the polymer-gradient deposition procedure.

Figure 3.6. Representation of the film coating step.

Figure 3.7. Relative mass fraction profiles of PCL and PDLA over the composition gradient library (Appendix A).

Figure 3.8. Static contact angles for a) piranha cleaned <100> silicon (24.38°±0.45°) and b) piranha cleaned + buffer oxide etched <100> silicon (69.24°±0.97°). Angles were measured using ImageJ image analysis software (NIH, public domain).

Figure 3.9. PCL/PDLA composition gradient library. Left side (hazy region): crystalline PCL rich regime. Right side (clear region): amorphous glassy PDLA regime. Transition occurs across the library as a result of the composition gradient.

Figure 3.10. Schematic of a linear temperature-gradient heating stage.

Figure 3.11. Illustration of a finished combinatorial library with coupled temperature and composition orthogonal gradients. The white line represents the LCST regime boundary, where phase separation takes place.

Figure 3.12. Heating stage surface temperature measurements. a) Temperature as a function of position (values are presented as mean ± SEM, n=9. Error bars are delimited with inverted cone markers). b) Temperature contour map showing "constant temperature lines" (constant Y).

Figure 3.13. Graphic representation of the ellipsometry test locations (red dots) over the composition gradient library.

Figure 3.14. Thickness measurements by ellipsometry for PCL/PDLA composition gradient libraries (red dots). The straight line corresponds to a linear fit of the ellipsometry data (R^2=0.993). *X*=0 mm and *X*=24 mm correspond to ϕ_{PCL}≈0.82 and ϕ_{PCL}≈0 respectively. Each data point represents the average thickness of 3 measurements over 3 different libraries. Error bars denote the standard uncertainty (±SEM, n=9).

Figure 3.15. Chemical structures of PCL and PDLA.

Figure 3.16. FTIR spectra of PCL/PDLA composition-gradient films: a) annealed library, b) non-annealed library. Each curve represents a different spot over the library (inset). ($\Delta\phi_{PCL}$≈0.82 to 0).

Figure 3.17. PCL mass fraction vs. position over a *non-annealed* linear-gradient PCL/PDLA library. The solid blue line represents the expected mass fraction of PCL (mass balance). Red dots represent the average value of the PCL concentration calculated at the same location in 2 separate libraries. Standard uncertainty given by error bars (±SEM, n=2).

Figure 3.18. PCL mass fraction vs. position over an *annealed* linear-gradient PCL/PDLA library. The solid blue line represents the expected mass fraction of PCL (mass balance). Green dots represent the average value of the PCL concentration calculated at the same location in 2 separate libraries. Standard uncertainty given by error bars (±SEM, n=2).

Figure 3.19. Root-mean-square surface roughness of three separate annealed composition-gradient libraries, obtained from topography maps of contact AFM mode. a), b) and c) denote libraries 1, 2 and 3 respectively.

Figure 3.20. a) Root-mean-square surface roughness profile of a PCL/PDLA annealed composition-gradient library. Values presented as averages ± SEM (indicated by error bars delimited by inverted cone markers, n=3). b) Contour map of the average root-mean-square surface roughness values over the composition-gradient library.

Figure 3.21. AFM images of a two-hour annealed PCL/PDLA library. Approximate composition and temperature of the scanned area are 26%PCL/74%PDLA and 120 °C respectively. a) Force modulation mode

map. b) Contact mode topography map. Scanned area: 100 μm x 100 μm.

Figure 3.22. AFM images of a two-hour annealed PCL/PDLA library. Images a) and c) correspond to force modulation maps, and images b) and d) to contact mode topography maps. Approximate compositions of the scanned areas are 39%PCL/61%PDLA for images a) and b), and 53%PCL/47%PDLA for images c) and d). Temperature is 120 °C for all images. Scanned area: 100 μm x 100 μm.

Figure 3.23. Three dimensional extensions of AFM topography maps of two-hour annealed PCL/PDLA libraries. a) 26%PCL/74%PDLA, PCL-rich droplet-like domains dispersed in a continuous PDLA-rich matrix. b) 39%PCL/61%PDLA, PCL-rich domains in a continuous PDLA-rich matrix. c) 53%PCL/47%PDLA, merged PCL-rich domains forming a bi-continuous PCL/PDLA matrix. The approximate annealing temperature of the sampled regions is 120 °C. Scanned area: 100 μm x 100 μm.

Figure 3.24. 2D and 3D topography maps of two-hour annealed PCL/PDLA libraries. a) 32%PCL/68%PDLA 110 °C, PCL-rich domains segregated in a PDLA-rich surrounding. b) 40%PCL/60%PDLA 100 °C, bi-continuous PCL/PDLA structure. Scanned area: 100 μm x 100 μm.

Figure 3.25. Three dimensional topography maps of two-hour annealed PCL/PDLA libraries. a) 70%PCL/30%PDLA 100 °C. b) 10%PCL/90%PDLA 95 °C. Scanned area: 100 μm x 100 μm.

Figure 3.26. Original polarized microscope picture of a phase separated PCL/PDLA blend. Bright and dark regions correspond to crystalline PCL and amorphous PDLA respectively. Encircled area shows uneven image lighting.

Figure 3.27. a) Generated approximation of the lighting pattern of the image shown in figure 3.26 (pseudo-clearfield map). Encircled area shows uneven image lighting. b) Light equalized and contrast enhanced image (grayscale). Encircled area highlights the light equalized region.

Figure 3.28. Overlay plane of the PCL/PDLA library region shown in figure 3.27b. Red pixels correspond to category 1 (PCL-rich) and black pixels to category 0 (PDLA-rich).

Figure 3.29. Filtering procedure of the original overlay plane to remove small PDLA domains from PCL rich regions.

Figure 3.30. Outlines of the measured regions generated during the image analysis procedure. Inset: particle size distribution.

Figure 3.31. Schematic of the maximal (F_{max}) and minimal (F_{min}) Feret's diameters of a random shape particle.

Figure 3.32. a) PCL surface coverage profile of a temperature-annealed PCL/PDLA composition-gradient library. Values presented as averages ± SEM (indicated by error bars delimited by inverted cone markers, n=4). b) Contour map of the PCL surface coverage values over the composition-gradient library.

Figure 3.33. a) PCL domain feret's diameter profile across a temperature-annealed PCL/PDLA composition-gradient library. Values presented as averages ± SEM (indicated by error bars delimited by inverted cone markers, n=4). b) Contour map of the PCL domain feret's diameter values over the composition-gradient library.

Figure 3.34. Variation of the PCL/PDLA surface microstructure as a function of temperature and composition. Bright=PCL-rich, dark=PDLA-rich. Numbers in parenthesis indicate PCL fraction (ϕ_{PCL}) and temperature (T) in ºC respectively (ϕ_{PCL},T).

Figure 4.1. Simplified graphic representation of the developmental stages of MC3T3-E1 osteoblast-like cells.

Figure 4.2. Blue autofluorescence emission of a PCL/PDLA library excited with a 379-401 nm source. Brighter sections correspond to PDLA structures.

Figure 4.3. Fluorescence microphotography (green channel) of a 2-day proliferation assay of MC3T3-E1 cells on TCPS using the ABSOLUTE-S™ SBIP cell proliferation protocol.

Figure 4.4. Fluorescence microphotography (green channel) of a 2-day proliferation assay of MC3T3-E1 cells on TCPS using a modification of the ABSOLUTE-S™ SBIP cell proliferation protocol.

Figure 4.5. Representative immunofluorescence images of some of the 2-day proliferation trial runs effectuated to determine optimal BrdU concentration (Green: BrdU, Red: EthD-2). From left to right: 10 μg/ml, 50 μg/ml and 100 μg/ml. Original magnification 20x.

Figure 4.6. MC3T3-E1 attachment density over a PCL/PDLA combinatorial library after a 6-hour culture period. Cell density presented as cells/cm^2 (average values over 5 libraries). Black line denotes the LCST boundary.

Figure 4.7. Static contact angle for a) pure PDLA (60.44º ± 0.37º) and b) pure PCL (78.54º ± 0.81º). Angles were measured using ImageJ image analysis software (NIH, public domain).

Figure 4.8. Overexposed images of MC3T3-E1 osteoblasts adhered on different locations of combinatorial PCL/PDLA libraries. Brighter and darker background structures correspond to PDLA-rich and PCL-rich domains respectively. Highlighted areas show cell attachment points onto PDLA structures. Original magnification 60x.

Figure 4.9. Cytoskeleton organization and predominant morphologies of MC3T3-E1 immature osteoblasts at different composition/temperature regimes over PCL/PDLA combinatorial libraries (6-hour culture). Cells were stained with rhodamine phalloidin for F-actin stress fibers (red), and Hoechst for DNA (blue). Original magnification 40x.

Figure 4.10. Positive control for attachment and morphology assays. F-actin: red, nucleus: blue. 6-hour culture on TCPS. Original magnification 40x.

Figure 4.11. Cell boundary outline by polygonal selection using segmented line sections (yellow line surrounding the cell marked with the arrow. Line sections are delimited by the white dots on the boundary).

Figure 4.12. Contour map of average circularity values of MC3T3-E1 cells cultured for 6 hours over 5 distinct combinatorial libraries.

Figure 4.13. Circularity of MC3T3-E1 cells cultured over PCL/PDLA combinatorial libraries for 6 hours. Values presented as averages ± SEM, n=5. SEM is represented by inverted cone marker error bars.

Figure 4.14. Phosphor-imager scans of the surface of PCL/PDLA combinatorial libraries cultured with MC3T3-E1 cells and immunostained for BrdU (proliferation assay). Darker regions correspond to areas of possible high cell proliferation rate (higher emission levels in the 500-530 nm wavelength range).

Figure 4.15. Immunofluorescence staining for proliferation of MC3T3-E1 osteoblasts over a PCL/PDLA combinatorial library after a 3-day culture. Cells were stained with Alexa Fluor® 488 (green) for BrdU incorporated into proliferated cells, and EthD-2 (red) to quantify total number of cells. Numbers in parenthesis indicate PCL mass fraction and temperature in ºC. Cell passage 5. Original magnification 40x.

Figure 4.16. TCPS positive control for the 3-day proliferation assay. Proliferated cells: green. Arrows indicate non-proliferated cells (stained only with EThD-2). Original magnification 40x.

Figure 4.17. 3-day and 4-day negative control cultures for proliferation assays. Arrows in the green filter images indicate the positions of cells as seen by EthD-2 staining (red filter images). Original magnification 40x.

Figure 4.18. Top: Proliferated to total number of cells ratio over a combinatorial PCL/PDLA library as a function of temperature and composition after a 3-day culture (cell passage 5). Values presented as averages ± SEM (n=6 blue mark, n=5 grey mark, n=4 green mark, n=3 violet mark, n=2 red mark). Bottom: Average proliferation ratio contour map.

Figure 4.19. Top: Proliferated to total number of cells ratio over a combinatorial PCL/PDLA library as a function of temperature and composition after a 4-day culture (cell passage 7). Values presented as averages ± SEM

(n=6 blue mark, n=5 grey mark, n=4 green mark, n=3 violet mark). Bottom: Average proliferation ratio contour map.

Figure 4.20. Top: Proliferated to total number of cells ratio over a combinatorial PCL/PDLA library as a function of temperature and composition after a 5-day culture (cell passage 4). Values presented as averages ± SEM (n=5 grey mark, n=4 green mark, n=3 violet mark, n=2 red mark, n=1 no mark). Bottom: Average proliferation ratio contour map.

Figure 4.21. Top: Proliferated to total number of cells ratio over a combinatorial PCL/PDLA library as a function of temperature and composition after a 8-day culture (cell passage 4). Values presented as averages ± SEM (n=6 blue mark, n=5 grey mark, n=4 green mark, n=2 red mark, n=1 no mark). Bottom: Average proliferation ratio contour map.

Figure 4.22. Alkaline phosphatase stained PCL/PDLA combinatorial libraries after 5-day culture with MC3T3-E1 cells (TCPS control is shown on the right). Dark areas near the LCST cloud point boundary correspond to alkaline phosphatase enhancing regimes.

Figure 4.23. Left: Combinatorial PCL/PDLA library stained for alkaline phosphatase after a 7-day culture with MC3T3-E1 cells (the white line represents the LCST boundary). Right: Positive control TCPS. Cell passage 6.

Figure 4.24. Left: Combinatorial PCL/PDLA library stained for alkaline phosphatase after a 8-day culture with MC3T3-E1 cells (the white line represents the LCST boundary). Right: Positive control TCPS. Cell passage 6.

Figure 4.25. Left: Combinatorial PCL/PDLA library stained for alkaline phosphatase after a 9-day culture with MC3T3-E1 cells (the white line represents the LCST boundary). Right: Positive control TCPS. Cell passage 5.

Figure 4.26. Von Kossa stain for MC3T3-E1 mineralization after a 14-day culture. Left: Combinatorial PCL/PDLA library (the red line represents the LCST cloud point boundary). Right: Positive control TCPS. Cell passage 4.

Figure 4.27. Von Kossa stain for MC3T3-E1 mineralization over combinatorial libraries after a 14-day culture (the red line represents the LCST cloud point boundary). Cell passage 4.

Figure 4.28. Viability comparison of different regions over totally confluent PCL/PDLA combinatorial libraries. a) 14-day test, lower border of the library. b) 13-day test, middle region of the library. c) 14-day test, middle region of the library. Viable cells: Green (stained with calcein AM), dead cells: Red (stained with EthD-1).

Figure A.1. Evolution of PCL and PDLA mass fractions during the mixing step.

Figure A.2. Relative PCL and PDLA mass fractions over a 24 x 24 mm silicon substrate as a function of position. $X_{A,0} = X_{B,0} = X_0 = 0.5$ (PCL and PDLA solutions with identical mass fractions).

Figure A.3. Right: PCL and PDLA mass fraction evolution during the mixing phase of the gradient library preparation ($X_{A,0}$ = 0.4 and $X_{B,0}$ = 0.05). Left: relative PCL and PDLA mass fractions over a 24 x 24 mm silicon substrate as a function of position ($X_{A,0}$ = 0.4 and $X_{B,0}$ = 0.05).

SUMMARY

Since the inception of the use of synthetic materials to interact with or replace biological systems, the field of biomaterials research has been one of intense work and constant innovation. Nowadays, the search of bioactive materials that regulate cell function in a desired manner is perhaps one of the most coveted goals in this area. However, the highly complex and interactive environment of biological systems has made of this task a very demanding one, especially because of the vast variable space involved. New experimental techniques, such as combinatorial methods, that overcome limitations of actual archetypes of material research have permitted to effectively address this large amount of variables.

Combinatorial techniques are utilized in this work to prepare *combinatorial libraries* of the blend of the biodegradable polymers Poly(ε-caprolactone) and Poly(lactic acid). These libraries present continuous composition and temperature gradients in an orthogonal fashion that permit to obtain multiple surface morphologies with controllable structures due to the blend's low critical solution phase behavior (LCST).

The goal of this study is to investigate the effect of surface morphology on cell behavior. The varied surface topography of the combinatorial libraries is used as a valuable tool that permits to assay the interaction between MC3T3-E1 cells and hundreds of different values of surface properties, namely, surface roughness and microstructure size. The outcome of this tool is a rapid screening of the effect of surface topography on cell behavior that is orders of magnitude faster than the standard 1-sample for 1-measurement techniques.

The results obtained show that cells are very sensitive to surface topography, and that the final effect of surface properties on cell function is intimately related with the

stage of the cell developmental process. Meaning that, for instance, the region with optimal characteristics to elicit enhancement of cell attachment is not necessarily the same that promotes cell proliferation.

This study imparts an improved understanding of an often neglected factor in biomaterials performance: surface topography. The results provide a new insight into the importance of taking into consideration both chemistry and physical surface features for superior biomaterials design.

CHAPTER I

INTRODUCTION

Polymers have had a strong and direct impact on our way of life during the past 50 years. Nowadays, from disposable cups to ultra strong airplane structures, polymers are present in almost any conceivable application and their use keeps growing in innumerable dissimilar fields. Certainly, biomedicine is not the exception. However, the use of synthetic polymers in this field is still cautious and narrow due to the extreme complexity of the interaction and response of biological systems to polymer surfaces. These limitations are mainly associated with polymer properties such as *biostability* and *biocompatibility*, which are directly related with long-term applications (i.e., orthopedic implants), where maintaining mechanical and thermal properties of the synthetic material inside the body's environment (biostability), causing the minimal immunogenic phenomena and inflammatory response (biocompatibility) is desirable.

With new trends in the use of polymers in medicine another important factor to take into account has emerged: *degradability*. Degradability, as well as biocompatibility, is essential for short-term applications such as temporary vascular grafts; drug delivery; and scaffolds for tissue engineering, a quickly developing branch of bioengineering; where synthetic materials that act as a temporary mechanical support for natural tissue must gradually degrade and weaken under physiological conditions. Ultimately, these degradable synthetic scaffolds are entirely replaced by natural tissue.

The number of approved degradable synthetic polymers by the U.S. Food and Drug Administration (FDA) is incredibly meager, since potential toxicity and secondary effects of the degradation products have to be carefully considered. Only a few of these

FDA approved degradable polymers are used routinely for a considerable range of applications in medicine. The most widely employed are poly(glycolic acid) and poly(lactic acid), which degrade by random hydrolysis into glycolic and lactic acids (harmless physiological metabolites); and Poly(ε–caprolactone) [1-3]. However, following the continued interest in obtaining new biomaterials with desirable properties, a new breed of biocompatible, bioerodible and degradable polymers is arising. Poly(malic acid) is one of these and stands out as an attractive material for biomedical applications, given that it is biocompatible and degrades to nontoxic malic acid. Besides, functionalization of its side-chain carboxylic groups can lead to obtain an extensive set of polymers and copolymers with different hydrophobic/hydrophilic balances, useful for biocompatible devices [4].

No matter what the application of the biomaterial is, its *surface properties* play a *critical* role because they control the biological response to the material. Hydrophobicity or hydrophilicity; smoothness, roughness or porosity; presence or absence of ionic groups; elements exposed at the surface; and bioerodability or biostability are some of the most significant surface properties [5]. Surfaces with the ability to control and regulate physiological and cellular responses are possibly the most critical need when developing new biomaterials.

Extensive research has been done on cell-polymer interactions, focusing mainly on how the surface chemistry of the synthetic material affects cell function, overlooking the role of the substratum physical features on such interactions. Awareness that cell shape and surface topographic features are somehow interlocked dates back to the 1930s. However, it wasn't until 1964 when clear signs of the effect of surface structure on cell shape led to propose the hypothesis that cells react to the contour of the environment on which they are grown [6]. Moreover, cell shape seems to greatly affect cell *function*. Folkman and Moscona [7] modified the surface *chemistry* of plastic culture

dishes in way that allow manipulation of the shape of bovine endothelial cells, showing it was critical for DNA synthesis and cell growth. Subsequent studies, based on the fact that cell shape is inherently related to surface structural features, proved that variations in cell shape due to micrometric and nanometric topography alter important cell functions such as gene expression, signaling, protein synthesis and growth [8-19].

The main challenge to discovering polymers with the optimum combination of chemical and physical surface properties to affect cell function in a desired way resides in the tremendous number of variables involved. This large variable space of parameters that can be adjusted to achieve changes in surface chemistry and structure overwhelms conventional single-sample for single-measurement techniques. High-throughput procedures have been developed in some limited fields to effectively screen large numbers of variables, i.e., combinatorial screening for catalyst research and drug discovery, and parallel PCR [20] used in genotyping. Similar approaches have been used for synthesis of novel degradable polymers in order to find structure-property correlations with cell interactions [21]. These techniques, while important for synthesis and control of bulk polymer chemistry, do not allow the rich variation in surface chemistry and structure that is desired. To overcome this problem combinatorial methods for preparing polymer “combinatorial libraries” with continuous surface property gradients have been developed [22, 23]. These methods are a streamlined way to search large ranges of composition and processing parameters [24] that allows *fast* and *effective* investigation, as hundreds to thousands of distinct chemistries and microstructure properties can be evaluated simultaneously.

This thesis aims to expand on the applications of the gradient-library technology to a wider range of bioassays. We will explore the effect of surface topography of biodegradable polymer blends on mouse osteoblast-like MC3T3-E1 cells, utilizing polymeric composition–temperature gradient libraries as a fast and effective screening

strategy. Rapid characterization of the polymer blend characteristics (i.e., composition and surface roughness) and cell response due to polymer-cell interactions (i.e., adhesion, proliferation, etc.), can be achieved. Specifically, the study will focus on identifying synergistic effects in libraries of the FDA-approved poly(ε-caprolactone) *(PCL)* and poly(D,L-lactide) *(PDLA)* when cultured with MC3T3-E1 cells. These polymers hold very dissimilar material properties (i.e. crystallinity, glass transition temperature, and tensile modulus) [25], and exhibit varied surface microstructures at different temperatures (phase separation) when blended, as a result of a low critical solution temperature (LCST) phase behavior and PCL crystallization [3, 26]. These naturally-occurring phase-separation processes will be utilized to generate a rich array of dissimilar surface chemistries and microstructures on a single sample (library), whose physical size is comparable to that of a microscope slide.

REFERENCES

1. **Simon C.G., Khatri C.A., Wight S.A., Wang F.W., *Preliminary report on the biocompatibility of a moldable, resorbable, composite bone graft consisting of calcium phosphate cement and poly(lactide-co-glycolide) microspheres.* Journal of Orthopaedic Research, 2002. 20: p. 473-482.**

2. **Ratner B.D., Hoffman A.S., Schoen F.J., and Lemons J.E., ed. *Biomaterials Science: An introduction to materials in medicine*. 1 ed. 1996, Academic Press: San Diego, CA. 484.**

3. **Meredith J.C., Sormana J.L., Keselowsky B.G., García A.J., Tona A., Karim A., and Amis E.J., *Combinatorial Characterization of Cell Interactions with Polymer Surfaces.* Journal of Biomedical Materials Research, 2003. 66A: p. 483-490.**

4. **Bizzarri R., Chiellini F., Solaro R., Chiellini E., Cammas-Marion S., and Guerin P., *Synthesis and characterization of new malolactonate polymers and copolymers for biomedical applications.* Macromolecules, 2002. 35: p. 1215-1223.**

5. **Allcock H.R., Lampe F.W., *Contemporary polymer chemistry*. 2 ed. 1990, New Jersey: Prentice Hall. 624.**

6. **Curtis A., Varde M., *Control of cell behaviour: topographical factors.* J Nat Cancer Res Inst, 1964. 33: p. 15-26.**

7. **Folkman J., Moscona A., *Role of cell shape in growth control.* Nature, 1978. 273: p. 345-349.**

8. **Huang S., Ingber D.E., *Shape-Dependent Control of Cell Growth, Differentiation, and Apoptosis: Switching between Attractors in Cell Regulatory Networks.* Experimental cell research, 2000. 261: p. 91-103.**

9. **Chung T.W., Liu D.Z., Wang S.Y., and Wang S.S., *Enhancement of the growth of human endothelial cells by surface roughness at nanometer scale.* Biomaterials, 2003. 24: p. 4655-4661.**

10. **Chen C.S., Mrksich M., Huang S., Whitesides G.M., Ingber D.E., *Geometric control of cell life and death.* Science, 1997. 276: p. 1425-1428.**

11. **Miller C., Shanks H., Witt A., Rutkowski G., and Mallapragada S., *Oriented Schwann cell growth on micropatterned biodegradable polymer substrates.* Biomaterials, 2001. 22: p. 1263-1269.**

12. **Thomas C.H., Collier J.H., Sfeir C.S., and Healy K.E., *Engineering gene expression and protein synthesis by modulation of nuclear shape.* PNAS, 2002. 99: p. 1972-1977.**

13. **Schwartz Z., Lohmann C.H., Vocke A.K., Sylvia V.L., Cochran D.L., Dean D.D., and Boyan B.D., *Osteoblast response to titanium surface roughness and 1α,25-(OH)2D3 is mediated through the mitogen-activated protein kinase (MAPK) pathway.* Journal of Biomedical Materials Research, 2001. 56: p. 417-426.**

14. **Lohmann C.H., Sagun R., Sylvia V.L., Cochran D.L., Dean D.D., Boyan B.D., and Schwartz Z., *Surface roughness modulates the response of MG63 osteoblast-like cells to 1,25-$(OH)_2D_3$ through regulation of phospholipase A_2 activity and activation of protein kinase A.* Journal of Biomedical Materials Research, 1999. 47: p. 139-151.**

15. **Boyan B.D., Batzer R., Kieswetter K., Liu Y., Cochran D.L., Szmuckler-Moncler S., Dean D.D., and Schwartz Z., *Titanium surface roughness alters responsiveness of MG63 osteoblast-like cells to 1α,25-$(OH)_2D_3$.* Journal of Biomedical Materials Research, 1998. 39: p. 77-85.**

16. **Chicurel M.E., Singer R.H., Meyer C.J., and Ingber D.E., *Integrin binding and mechanical tension induce movement of mRNA and ribosomes to focal adhesions.* Nature, 1998. 392: p. 730-733.**

17. **Huang S., Chen C.S., and Ingber D.E., *Control of Cyclin D1, $p27^{Kip1}$, and Cell Cycle Progression in Human Capillary Endothelial Cells by Cell Shape and Cytoskeletal Tension.* Molecular Biology of the Cell, 1998. 9: p. 3179-3193.**

18. **Wójciak-Stothard B., Madeja Z., Korohoda W., Curtis A., and Wilkinson C., *Activation of macrophage-like cells by multiple grooved substrata. Topographical control of cell behavior.* Cell Biology International, 1995. 19(6): p. 485-490.**

19. **Singhvi R., Kumar A., Lopez G.P., Stephanopoulos G.N., Wang D., Whitesides G.M., and Ingber D.E., *Engineering cell shape and function.* Science, 1994. 264: p. 696-698.**

20. **Chicurel M.E., *Faster, better, cheaper genotyping.* Nature, 2001. 412: p. 580-582.**

21. **Brocchini S., James K., Tangpasuthadol V., and Kohn J., *Structure-property correlations in a combinatorial library of degradable materials.* Journal of Biomedical Materials Research, 1998. 42: p. 66-75.**

22. **Meredith J.C., Smith A.P., Karim A., and Amis E.J., *Combinatorial Materials Science for Polymer Thin-Film Dewetting.* Macromolecules, 2000. 33: p. 9747-9756.**

23. **Meredith J.C., Karim A., and and Amis E.J., *High-Throughput Measurement of Polymer Blend Phase Behavior.* Macromolecules, 2000. 33: p. 5760-5762.**

24. **Meredith J.C., *A Perspective on High-Throughput Polymer Science.* Journal of Materials Science, 2003. in press (October 2003 Issue).**

25. **Engelberg I., Kohn J., *Physicomechanical properties of degradable polymers used in medical applications: A comparative study.* Biomaterials, 1991. 12: p. 292-304.**

26. **Meredith J.C., Amis E.J., *LCST phase separation in biodegradable polymer blends: poly(D,L-lactide) and poly(ε-caprolactone).* Macromol. Chem. Phys., 2000. 201(6): p. 733-739.**

CHAPTER II

BACKGROUND AND THEORETICAL BASIS

2.1. OVERVIEW

The field of medical and biomedical material research is an innovative area of endless and intense work. Its goal: to create synthetic and/or natural materials with very specific properties (i.e., biological interaction, biocompatibility, physicochemical characteristics, etc), that can be successfully used in the highly complex and interactive in vivo biological environment (biomaterials). Hence, a great deal of the work being done in this area is focused on exploring the effect of distinct surface characteristics on cell behavior and function (cell-surface interactions).

The amount of dissimilar surface properties that can affect cell behavior and function is extremely broad. A few examples are modulation of cell attachment, spreading, and growth using polymer surfaces with diverse functional groups [1]; control of cyclin D1 and cell cycle progression with chemically patterned surfaces [2]; upregulation of cell proliferation and specific gene expression with changes in surface roughness [3]; promotion of contact guidance using textured surfaces [4]; changes in cytoskeletal organization with variation of surface wettability [5]; and control of cell proliferation with variation of polymer crystallinity [6]. However, as mentioned above, these are only a *few* of the myriad of different surface characteristics that can affect an even broader number of cell properties, making the characterization of a particular material a very difficult task. In addition, the steady increase of available materials to explore (specially polymers and polymer blends), coupled with standard measuring

techniques (single-sample for single-measurement), make more difficult to generate a unifying hypothesis on materials surface properties and their effect on different types of cells.

Combinatorial techniques stand as one feasible option to address this problem, as they allow assaying vast amounts of variables in a *simultaneous* fashion. These techniques have been successfully used in several other fields (section 2.2.9) and have gained recognition as an optimal approach for experiments where large amounts of variables are involved.

Combinatorial methods are starting to be widely used in the bioengineering and biotechnology fields, and have already been proven to facilitate the study of the effect of surface properties on cell behavior and function. For example, Meredith et al [7] have use combinatorial libraries of polymer blends with low critical solution temperature phase behavior to create surface morphology variations that affect cell behavior. Brocchini et al [8] and Washburn and coworkers [6], have also demonstrated the power of combinatorial techniques by using combinatorial libraries to assay cell proliferation as a function of surface chemistry and surface crystallinity respectively.

2.2. BACKGROUND

2.2.1. GENERAL CONCEPTS ABOUT CELLS AND ECM

Cells are highly organized structures composed by organelles that perform very specialized functions (i.e., production of glyco and lipoproteins, DNA synthesis, and production of proteolytic enzymes). The remainder of the cell comprises the cytoplasm and the cell membrane, which surrounds both the organelles and the cytoplasm.

Different regions of the cell membrane correspond to different functions, such as mechanical attachment, adsorption, secretion, and communication with other cells [9, 10].

Microfilaments in the cytoplasm, made of actin, myosin, actinin, and tropomysoin, create a network, called cytoskeleton, that is responsible for cell adhesion and locomotion [10]. This network is connected to the membrane via integrin structures, which are receptors consisting of heterodimeric proteins with two membrane-spanning subunits [11]. Integrins play an important role on cell behavior as they have the ability to transduce bi-directional signals that engage reciprocal interactions between cells [12, 13]. They also mediate cell adhesive interactions by binding to ligand motifs of adhesive proteins (i.e., fibronectin and vitronectin), that, in turn, bind to solid substrates, extracellular matrix components, and other cells.

The extracellular matrix (ECM) is an intricate network of secreted extracellular macromolecules consisting primary of fibrous proteins embedded in a hydrated polysaccharide gel. ECM helps to hold cells and tissues together, and provides an organized lattice within which cells can migrate and interact with each other (paracrine cell signaling) [10]. The extracellular matrix occurs in two forms: interstitial matrix (i.e., connective tissue) and basement membrane (i.e., epithelium) [9]. Besides providing mechanical support for cellular anchorage, the diverse functions ECM include: control of cell growth, determination of cell orientation, support for cell proliferation and tissue renewal, maintenance of cell differentiation, etc.

2.2.2. CELL ADHESION AND SPREADING

The vast majority of cell types undergo apoptosis (cell death) when deprived of adhesion to the ECM [14]. Hence, cell adhesion is generally regarded as a crucial survival factor for cells.

In a physiological environment, protein adsorption (section 2.2.3) always precedes cellular adhesion. These preadsorbed proteins, in combination with proteins produced by the cell, and depending on the substratum characteristics, govern the strength and type of the adhesive sites. There are three regular types of adhesive sites between cells and solid substrata [15]:

- Focal adhesion: Represents a very strong adhesion that generally involves binding to fibronectin. Corresponds to a 10-20 nm gap habitually observed at the cell boundaries.

- Close contact: Corresponds to a 30-50 nm gap generally surrounding the focal adhesions.

- Extracellular matrix contacts: Formed by strands and fibers of ECM material that connect the ventral cell wall with the underlying substratum. Gap > 100 nm.

A schematic of the types of cell-surface adhesive sites is presented in Figure 2.1.

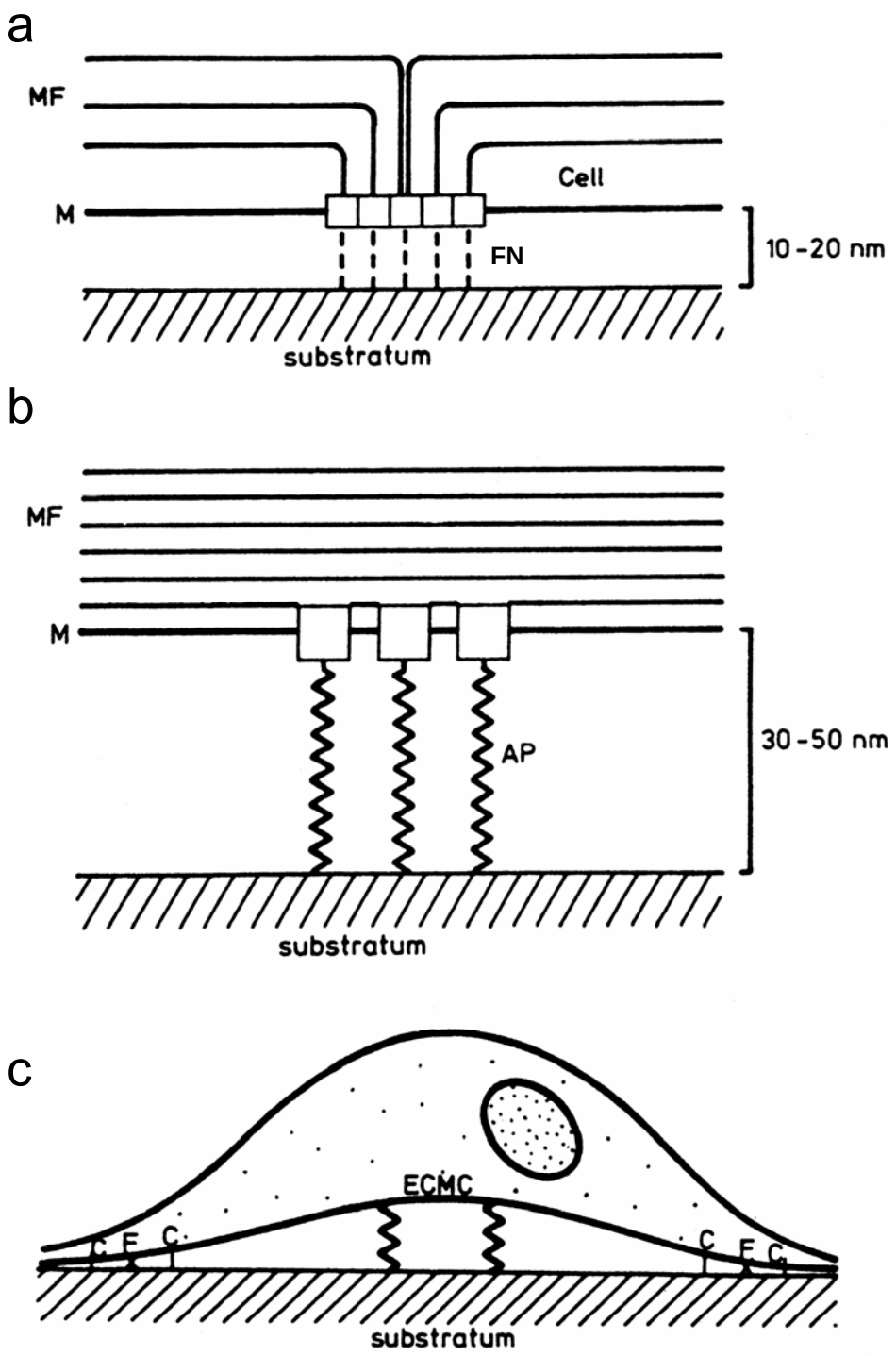

Figure 2.1. Cell-substratum contact sites. a) Focal adhesion points, strong adhesive sites, are mainly found at the boundaries of cellular extensions. The integrin connects the cytoskeleton with the substratum via fibronectin. b) Close contacts (less strong adhesive sites). c) Localization of the different adhesive sites. MF: microfilaments, M: cell membrane, AP: adhesive protein, FN: fibronectin, ECMC: extracellular matrix contact, C: close contact, F: focal adhesion [9].

As mentioned before, cells can also adhere to the ECM or to other cells. The contacts formed in these kinds of interactions differ significantly from those found in cell-surface interactions, and are characterized by four regular adhesive sites: gap junction (nexus), formed by an array of plaque-like connections between the plasma membranes of adjacent cells (gap ~ 4 nm); desmosome, mechanical attachment formed by the thickened plasma membranes of two adjacent cells, containing dense material in the intercellular (gap ~ 30-50); hemidesmosome, equivalent to desmosomes between cells and ECM; and tight junction, formed when adjacent cell membranes adhere to each other (gap < 5 nm).

Once cells attach to a surface they spread onto it as a result of the combined process of continuing adhesion and cytoplasmic contractile meshwork activity. Spreading induced stress promotes the generation of actin stress fiber and cytoskeleton development. Cell adhesion and spreading are directly influenced by the physicochemical characteristics of the underlying solid surface.

2.2.3. CELL-SURFACE INTERACTIONS

The importance of proteins in biomaterials science stems primary from their inherent tendency to deposit on surfaces as a strongly bound adsorbate layer, and the noticeable influence these deposits have on cell-surface interactions.

Generally, synthetic foreign materials acquire bioreactivity only after first interacting with dissolved proteins. Adsorbed proteins transform an inert, non-thrombogenic material in to a biologically active surface that can modulate cell adhesion, spreading, and function [16].

It is thought that the particular properties of surfaces, as well as the specific properties of individual proteins, together determine the organization of the adsorbed

protein layer, and that the nature of this layer, in turn, determines the cellular response to the adsorbed surfaces. For example, it has been observed that poor cell spreading is achieved on hydrophobic substrata while good cell spreading is promoted over hydrophilic substrata in *both* the absence and presence of serum proteins (figure 2.2) [17]. The substratum characteristics are reflected in the composition and conformation of different kinds of adsorbed proteins, namely, serum proteins and cell-produced proteins, thus presenting different molecular groups to adhering and spreading cells.

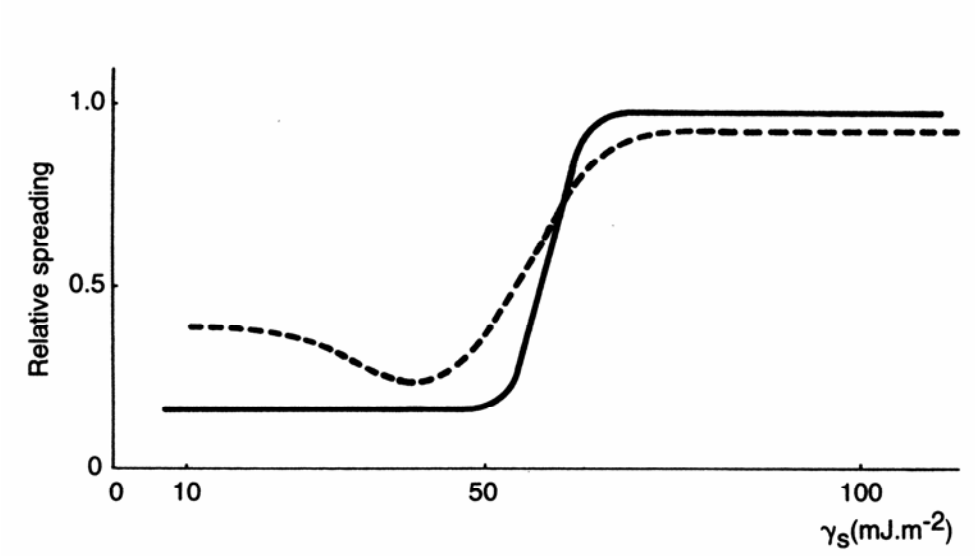

Figure 2.2. Cell spreading as a function of substratum surface free energy (γ_S, wettability). Dotted line represents cell spreading in the absence of proteins. Solid line represents cell spreading in the presence of serum proteins [17].

Other material properties such as negatively charged surface groups, surface topography, roughness, texture, and porosity, have been shown to elicit unquestionable influence on multiple cell events [1, 8, 18, 19].

2.2.4. BIOMATERIALS

The inception of the use of non-living substrata to replace living tissue can be traced back to more than 2000 years ago when Aztecs, Chinese, and Romans used gold inserts to replace lost or damaged teeth. Later on, through history, glass and wood followed as the materials of choice. However, it wasn't until the second half of the last century when a vast upsurge in the diversity of materials to replace or interact with living tissue was witnessed. Nowadays, these substrata or external materials, habitually referred to as *biomaterials*, are utilized in diverse applications (i.e., cell culture devices, bioreactors, bioelectronics, etc). Yet, their primary and most notorious use resides in the medical field [20].

Perhaps the most well known and widespread applications of biomaterials in medicine are substitute heart valves to correct degenerated, damaged, or congenitally diseased heart valves; artificial hip joints to mend acute joint wear due to excessive stress, or because degenerative or rheumatologic disease; intraocular lenses to replace cloudy and cataractous natural lenses; and dental implants. However, there is a vast variety of other clinical applications for biomaterials, each one with its own specific requirements. For example, bone implants are favored by materials that elicit intimate and synergistic cell-material interactions (osteoconductivity). On the contrary, to avoid thrombogenic effects, materials used in cardiovascular applications must remain biologically inactive or, in other words, "invisible" to cells. Table 2.1 lists a few traditional synthetic materials of common use in medicine to repair and/or replace body parts.

Table 2.1. Applications of synthetic materials and modified natural materials in medicine [20].

Application	Types of materials
Skeletal system	
Joint replacements (hip, knee)	Titanium, Ti-Al-V alloy, stainless steel, polyethylene
Bone plate for fracture fixation	Stainless steel, Co-Cr alloy
Bone cement	Poly(methyl methacrylate)
Bony defect repair	Hydroxylapatite
Artificial tendon and ligament	Teflon, Dacron
Dental implant for tooth fixation	Titanium, alumina, calcium phosphate
Cardiovascular system	
Blood vessel prosthesis	Dacron, Teflon, polyurethane
Heart valve	Reprocessed tissue, stainless steel, carbon
Catheter	Silicon rubber, Teflon, polyurethane
Organs	
Artificial heart	Polyurethane
Skin repair template	Silicone-collagen composite
Artificial kidney (hemodialyzer)	Cellulose, polyacrylonitrile
Heart-Lung machine	Silicone rubber
Senses	
Cochlear replacement	Platinum electrodes
Intraocular lens	Poly(methyl methacrylate), silicone rubber, hydrogel
Contact lens	Silicone-acrylate, hydrogel
Corneal bandage	Collagen, hydrogel

Polymers, exceptionally versatile materials, have been widely used in countless different applications in medicine and bioengineering because of their adaptableness and excellent physicochemical properties. Moreover, today, polymers are taking the vanguard in the biomaterials field as constant evolution of polymer design and synthesis is coupled with a steady improvement of manufacturing processes. The result is robust and enduring materials that are more stable and durable than their predecessors, and that can withstand the harsh body environment preserving their physical and chemical characteristics. However, there's a type of polymeric materials with the opposite

durability and stability character that, lately, is getting a great deal of attention in medicine and bioengineering, namely, degradable polymers.

2.2.5. DEGRADABLE POLYMERS

Contrary to general beliefs, there are certain conditions and applications where polymers with *reduced* long-term chemical resistance (*degradable* polymers) are sought. Disposable products and plastic packaging are maybe some of the few examples where the use of degradable polymers is known to be beneficial, as they ease waste management due to their rapid chemical degradation and structure breakdown. However, degradable polymers are becoming of increasing significance in a myriad of dissimilar areas and applications that, perhaps, are not that well known, or where the use of degradable materials was thought to be detrimental. Medicine, bioengineering, and pharmaceuticals are good examples of fields where prompt decomposition of polymeric materials can bring out desired effects.

What is the definition of a degradable polymer? Well, the answer is not simple since at the end all polymers degrade one way or another; some of them after incredibly long periods of time (table 2.2). Thus every polymer would have to be considered as degradable. To eliminate this vagueness an additional criterion met by degradable polymers but not by non-degradable ones has to be introduced. Measuring degradation in terms of a relative time, like the duration of an application or the human life time, instead of an absolute time is a plausible one. Usually, if a polymer doesn't degrade within the average human life time it is not considered as degradable.

Table 2.2. Half-life of some classes of polymers [21].

Polymer class	Half-life
Poly(anhydrides)	0.1 h
Poly(ortho esters)	4 h
Poly(esters)	3.3 years
Poly(amides)	83,000 years

The criterion of a relative time to define polymer degradability led to the definition of a *Deborah number*. Deborah numbers, which are dimensionless, were first used to classify viscoelastic materials into more viscous ones and more elastic ones, and also for characterization of polymer swelling. In the case of degradable/non-degradable polymers a Deborah number that allows distinguishing between them can be defined as follows [22]:

$$D = \frac{\text{time of degradation}}{\text{human lifetime}} \tag{2.1}$$

Small values for D ($D \rightarrow 0$) would be characteristic of highly degradable polymers and large ones ($D \rightarrow \infty$) of nondegradable polymers. Evidently, the Deborah values sought for a degradable polymer depend directly on the type of application of such polymer. In this manner, for example, for an absorbable suture $D<<<<1$; whereas for a packaging plastic $D<<1$.

2.2.6. DEGRADATION, EROSION, BIODEGRADATION, BIOEROSION

There's still no agreement on a single definition for erosion and degradation. Likewise, the meaning of the prefix *bio* is not well established, leading to the frequently interchangeable use of terms "erosion" and "bioerosion" or "degradation" and "biodegradation". It is therefore necessary to define the usage of these terms in the context of this work.

Degradation is the process of polymer chain break by cleavage of the polymer backbone. Consequently degradation leads to a size reduction of the polymer chains. *Erosion*, on the other hand, is the mass loss of a polymer matrix due to the loss of monomers, oligomers or even pieces of nondegraded polymer. Erosion can be the result of chemical, physical or biological effects (it is obvious that degradation is a part of polymer erosion) [23, 24].

Biodegradation should be used only when a biological agent, i.e. an enzyme, is a central component of the degradation course [25]. Therefore, the degradation of poly(lactic acid) into lactic acid caused by hydrolytic cleavage of the polymer backbone should not be described as "biodegradation", since there's little or no evidence of active enzyme participation this process. In the case of *bioerosion* the *bio* suffix indicates that the erosion process, as defined before, occurs under physiological conditions, as opposed to other physical or chemical erosion processes such as high temperature, UV exposure or contact with strong acids or bases [20].

2.2.7. DEGRADABLE POLYMERIC BIOMATERIALS

Degradable materials for use in medical and biomedical applications, or that have to be in contact with biological systems, must fulfill more rigid requirements in

terms of their biocompatibility than their nondegradable counterpart. Potential toxicity of the degradation products and subsequent metabolites *must* also be considered, being the practical outcome of this that only a limited number of *nontoxic* materials have been effectively used to manufacture degradable biomaterials.

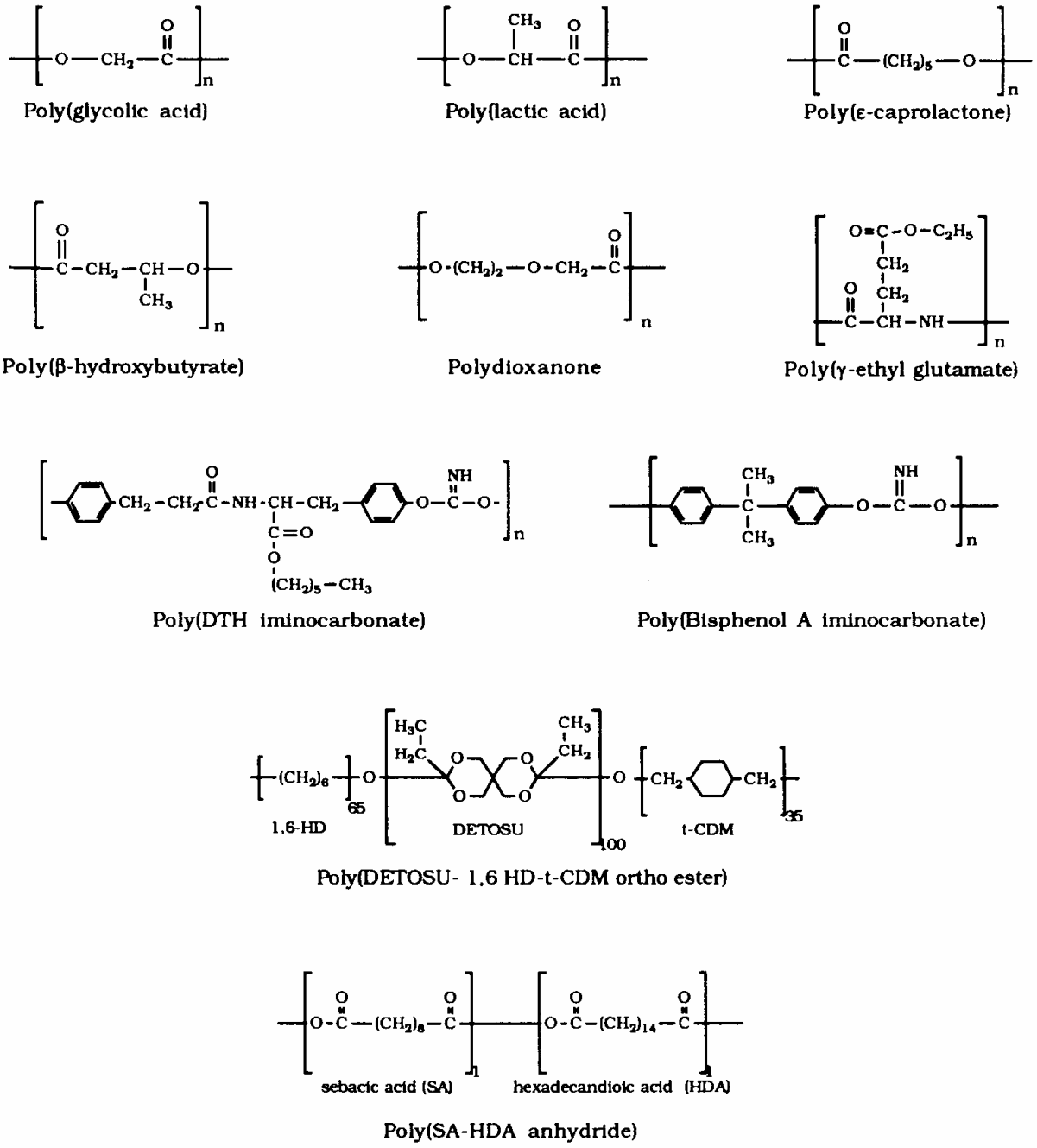

Figure 2.3. Chemical structures of degradable polymers [20, 26].

Hundreds of hydrolytically unstable polymers have been suggested as degradable biomaterials. However, detailed investigations of degradation rates and mechanisms, thorough toxicological studies, and in depth evaluations of physical and chemical properties have been done, until now, for just a minute fraction of those polymers. Poly(lactic acid) and poly(glycolic acid) are examples of some of these few widely investigated polymers [20, 26].

Table 2.3. Mechanical properties of some degradable polymers [27].

Polymer	Glass transition (°C)	Melting temperature (°C)	Tensile strength (MPa)	Tensile modulus (MPa)	Flexural modulus (MPa)	Elongation	
						Yield (%)	Break (%)
Poly(glycolic acid) (MW: 50,000)	3.5	210	n/a	n/a	n/a	n/a	n/a
Poly(lactic acids)							
L-PLA (MW: 50,000)	54	170	28	1200	1400	3.7	6.0
L-PLA (MW: 100,000)	58	159	50	2700	3000	2.6	3.3
L-PLA (MW: 300,000)	59	178	48	3000	3250	1.8	2.0
D,L-PLA (MW: 20,000)	50	-	n/a	n/a	n/a	n/a	n/a
D,L-PLA (MW: 107,000)	51		29	1900	1950	4.0	6.0
D,L-PLA (MW: 550,000)	53	-	35	2400	2350	3.5	5.0
Poly(β-hydroxyburyrate) (MW: 422,000)	1	171	36	2500	28.50	2.2	2.5
Poly (ε-caprolactone) (MW: 44,000)	-62	57	16	400	500	7.0	80
Polyanhydrides[a]							
Poly(SA-HDA anhydride) (MW: 142,000)	n/a	49	4	45	n/a	14	85
Poly(ortho esters)[b]							
DFTOSU : t-CDM : 1,6-HD (MW: 99,700)	55	-	20	820	950	4.1	220
Polyiminocarbonates[c]							
Poly(BPA iminocarbonate) (MW: 105,000)	69	-	50	2150	2400	3.5	4.0
Poly(DTH iminocarbonate) (MW: 103,000)	55		40	1630	n/a	3.5	7.0

[a] A 1 : 1 copolymer of sebacic acid (SA) and hexadecanedioic acid (HDA) was selected as a specific example.
[b] A 100:.35:6S copolymer of 3,9-bis(ethylidene 2,4,8,10-tetraoxaspiro(5,5) undecane) (DETOSU), trans-cyclohexane dimethanol (t-CDM) and 1,6-hexanediol (1,6-HD) was selected as a specific example.
[c] BPA: Bisphenol A; DTH: desaminotyrosyl-tyrosine hexyl ester.

It is remarkable that a large portion of the presently studied degradable polymers are polyesters. Research has led to new tentative degradable polymers that can find practical applications as biomaterials in the near future, namely, polyanhydrides;

polyhydroxybutyrate (PHB), polyhydroxyvalerate (PHV), and their copolymers; polycaprolactone; poly(ortho esters); poly(amino acids) and “pseudo”-poly(amino acids); polycyanoacrylates; and polyphosphazenes. Some of their structural formulas and mechanical properties, including those of poly(lactic acid) and poly(glycolic acid), are shown in figure 2.3 and table 2.3 respectively.

Whether or not these alternative backbone structures can challenge the dominant position of polyesters remains to be seen.

The next 2 sections show some characteristics of the polymers used in this work, namely, Poly(lactic acid) and Poly(ε-caprolactone).

2.2.7.1. POLY(LACTIC ACID) AND POLY(GLYCOLIC ACID)

Poly(lactic acid) (PLA) and poly(glycolic acid) (PGA), which are also referred to as polyglycolide and polylactide, are currently the most widely investigated and commonly used bioerodible polymers.

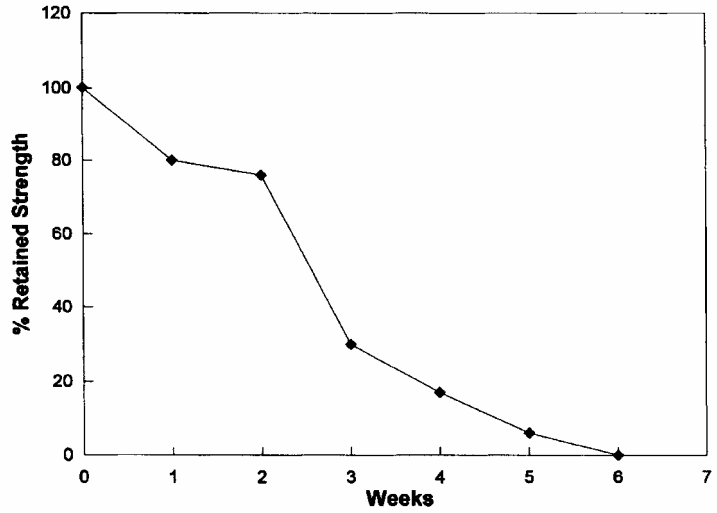

Figure 2.4. *In vitro* degradation of PGA. Retained tensile strength vs. time [28]. Without its unique crystalline behavior, PGA would degrade much faster.

PGA, relative to other biodegradable polymers, is highly crystalline, with a crystallinity range reported in the range of 35-75%. The molecular and subsequent crystalline structure of PGA allow very tight chain packing and consequently give to the material some very unique mechanical, physical, and chemical properties. For example, its specific gravity is around 1.5-1.7 which is very high for a polymeric material. It also has a high melting point and low solubility in most organic solvents.

PGA, which is the simplest linear aliphatic polyester (figure 2.3), degrades by hydrolysis of the easy accessible and hydrolytically unstable aliphatic-ester linkages. The degradation time, usually a few weeks (figure 2.4), depends on multiple factors like molecular weight, degree of crystallinity, crystal morphology, and physico-chemical characteristics of the environment.

To adapt to a wider range of potential application the material properties of PGA, it has been copolymerized with the more hydrophobic PLA. In thin films, for example, the hydrophobic of PLA limits the water uptake to about 2% and decreases the rate of backbone hydrolysis compared to pure PGA.

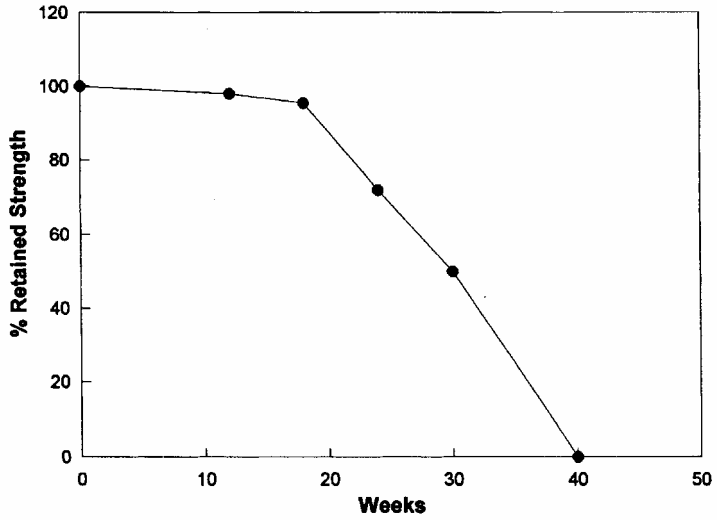

Figure 2.5. *In vitro* degradation of L-PLA. Retained tensile strength vs. time [22].

While structurally very similar to PGA, PLAs have quite different chemical, mechanical and physical properties due to the presence of a pendant methyl group on the alpha carbon (figure 2.3). This makes the PLA a chiral molecule and the D, L, and DL isomers are possible. The two stereoregular isomers D-PLA and L-PLA are made from D(+)-lactide and L(-)-lactide respectively; while D,L-PLA is a racemic mixture of the optically active L(-) and D(+) isomers. A fourth morphological form —meso-PLA— rarely used in practice, has both the L(-) and the D(+) configurations on the same dimmer molecule. D-PLA and L-PLA are semicrystalline polymers, while D,L-PLA Is a completely amorphous material. Commonly, L-PLA is more frequently employed than D-PLA, since the hydrolysis of L-PLA generates L(+) lactic acid, which is the natural occurring stereoisomer of lactic acid.

The methyl group in PLA makes the carbonyl of the ester link sterically less accessible to hydrolytic attack, which; depending on certain factors like the type of PLA, its molecular weight, and its degree of crystallinity; makes the PLAs typically more hydrolytically stable than PGA when exposed to the same environment (figure 2.5). It's important to note that D,L-PLA degrades faster than L-PLA due to its lack of crystallinity.

2.2.7.2. POLYCAPROLACTONE

Poly(ε-caprolactone) (PCL) is a semicrystalline degradable polymer with a relatively low melting point (T_m) ~60°C [29, 30]. The molecular structure of PCL consists of a single relatively polar ester group and five nonpolar methylene groups (figure 2.3). This gives to PCL certain unique properties, namely; mechanical characteristics similar to polyolefins, due to its high olefinic content; and degradability, due to the presence of hydrolytically unstable aliphatic-ester links. This, combined with its high solubility and low

melting point, makes PCL compatible with numerous other polymers, giving it the exceptional ability to easily form blends [31].

Polycaprolactone degrades at a slower pace than PLA (figure 2.6), one reason why it is used in applications where the polymer has to maintain its physico-chemical properties for more than a few weeks, i.e. drug delivery.

Regarded as a non toxic and tissue-compatible material by extensive toxicological studies, and with a unique blend of characteristics, polycaprolactone stands out as one of the most versatile degradable biomaterials.

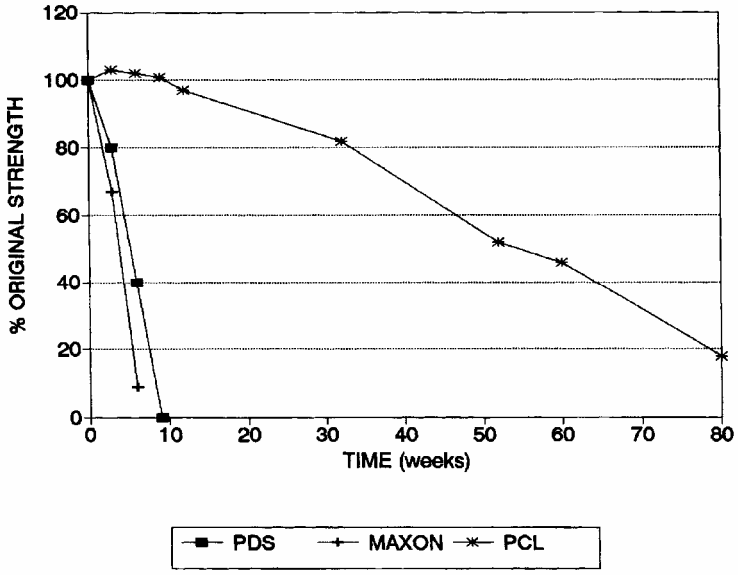

Figure 2.6. *In vivo* degradation of absorbable sutures [22]. PDS® and MAXON® are commercial PLA-PGA sutures.

2.2.8. POLYMER BLENDS

Polymers are rarely used in pure form, but are rather blended in most commercial applications. Polymer blends are the result of mixing together two or more polymers or copolymers [32]. In contrast to copolymers, where the constituents are

linked by strong covalent bonds, the components in physical blends adhere through weaker secondary intermolecular forces such as van der Waals forces, dipole interaction or hydrogen bonding.

Generally, polymer blends exhibit properties that can markedly vary from those of the individual polymers [33], which is why they are used commercially to combine the unique characteristics of several materials into one product. For example, brittle polymers can be strengthened by incorporating into their microstructure soft elastomeric components that can act as “stress concentrators”, due to their lower tensile modulus. The embedded stress concentrators in the more brittle continuous phase permit elastic energy storage or ductile yield mechanisms that increase its resistance to fracture [29]. Therefore, polymer blends can be a cost effective way of modifying properties of materials, as contrasted against chemical modification routes; hence, a major thrust of polymer development efforts has been focused on blends.

The resultant properties of a blend depend heavily on the physico-mechanical properties of the components, as seen on the Fox equation for miscible blends (equation 2.2); as well as the blend microstructure, the interface between the phases, and the processing conditions [30, 34].

$$\frac{1}{Tg} = \sum_{i=1}^{n} \frac{\omega_i}{Tg_i} \tag{2.2}$$

Where Tg, Tg_i are the glass transition temperatures of the blend and polymer i respectively, and ω_i is the mass fraction of polymer i.

Polymer blends can be either miscible or immiscible [32]. The miscible blends are divided into homologous blends (blends of the same polymer, such as a mixture of polystyrene fractions of different molecular weight) and heterogeneous blends, i.e., polyphenylene ether (PPE) with polystyrene (PS). Within the immiscible blends there is a

subgroup of compatible polymers which due to small interfacial tension, are morphologically stable, i.e., finely dispersed mixtures of polyolefins [35]. Immiscible blends can display different phase-separated morphologies, including co-continuous, semi-continuous, (see section 2.3.1), or droplet morphologies where isolated droplets of one of the components are present in a continuous matrix of the other component. The rich variety of phase-separated morphologies, which is dependent on both composition and temperature, adds a great deal of complexity to their investigation. For example, a simple binary blend has an exhaustive number of temperature, composition, and processing time-dependent morphologies that each has unique bulk and surface properties.

2.2.9. COMBINATORIAL METHODS AND HIGH THROUGHPUT SCREENING TECHNIQUES

Combinatorial methods and high throughput screening techniques can be seen as experimental methodologies that offer the ability to *efficiently* evaluate large numbers of variables in a single experiment. These methods have been used successfully for several years in the pharmaceutical industry, changing literally the way new drugs are discovered. Nowadays, they are embraced by almost every pharmaceutical company. However, pharmaceuticals is not the only area where combinatorial approaches have had a major impact. Other applications where combinatorial techniques have had a major impact are biodegradable materials characterization [8], genomics [36], liquid chromatography [37], optimization of new catalysts [38-41], and development of new optical and magnetic materials [42] have been also benefited by their use. Today these methods are receiving increasing attention in every area where rapid and reliable generation of experimental data as a function of multiple variables is needed.

The immense advantage of combinatorial methods resides in that they allow *simultaneous* synthesis and evaluation of "libraries" that encompass large variable spaces (i.e., chemical and physical properties of polymer blends), overcoming the enormous limitations of evaluating one variable at a time that is characteristic of traditional experimental approaches. This can lead to accelerated discovery of new materials, properties, or synthetic routes with low experimental variance.

Despite relying on the same general idea, combinatorial methods can differ considerably from application to application. In pharmaceuticals, for example, where the goal is to synthesize a new drug or improve an existing one, carefully selected *discrete* libraries are used to explore relevant compositions. On the other hand, polymers are sometimes better explored by *continuous* libraries since they are easily prepared over large ranges of compositions, temperatures, or thicknesses under the *same* environmental conditions, i.e., humidity. In a discrete library approach, each sample on the library would have to be cautiously controlled resulting in a dependence on complex robotics for mixing and annealing [43]. However commercial instruments to prepare polymeric continuous libraries that reproduce conditions such as phase transitions, reactions, transport properties and interfacial phenomena are not available.

Novel procedures like the gradient-film coating technique [44] have been developed recently to allow preparation of continuous polymer libraries. The gradient-film coating technique permits preparation of libraries with thickness and composition *continuous gradients*.

2.2.10. COMPOSITION-GRADIENT LIBRARIES

The preparation of composition-gradient libraries, as discussed in the literature [44, 45], involves three steps (figure 2.7):

- Gradient mixing
- Deposition
- Film spreading

During the gradient mixing step (figure 2.7a), a solution of polymer A is gradually infused inside a vial containing a solution of polymer B, generating a time dependant concentration gradient. An automated sampling system continuously extracts a very small amount of this concentration-changing solution, so at the end of the process a sample with a composition gradient of both polymers is obtained.

In the deposition step (figure 2.7b) the gradient sample is “painted” as a thin stripe along a substrate. Then it is spread as a film using a knife-edge coater that moves the substrate, with the gradient stripe below a stationary blade, in a direction perpendicular to the stripe painting direction (figure 2.7c) at a constant velocity. The solvent evaporates after a few seconds, leaving behind a thin film with a continuous composition gradient (A-rich in one end and B-rich in the opposite end).

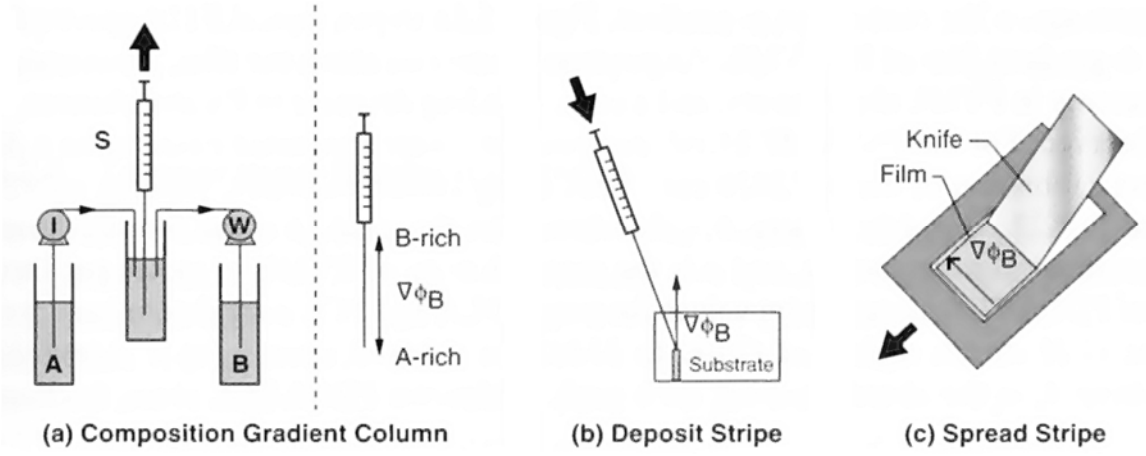

Figure 2.7. Representation of the preparation of composition-gradient libraries using the gradient-film coating technique [44, 45].

2.2.11. THICKNESS GRADIENT LIBRARIES

The steps involved in the making of thickness-gradient libraries are the same as the second and third steps of the process to make composition-gradient libraries, previously described. The main differences are that the stripe that is painted on the substrate has a homogeneous composition and that the coating is *not* done at constant speed (acceleration ≠ 0).

The change in velocity during the coating step is the key to obtain differences in thickness along the film. An increase in velocity leads to an increase in the volume of fluid that passes below the blade per unit time (figure 2.8). This results in increasing film thickness with increasing coating speed.

Composition-gradient libraries can be coupled with thickness-gradient ones by simply carrying out the spreading step of the composition-gradient library preparation (figure 2.7c) at variable speed. The result is a library with orthogonal composition and thickness gradients.

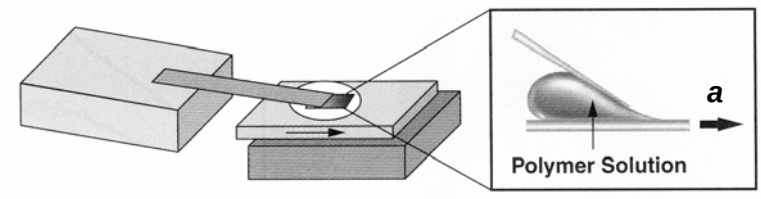

Figure 2.8. Representation of the method to prepare thickness-gradient libraries [45, 46]. The substrate is moved with a particular acceleration rate to create a gradient in film thickness.

2.2.12. TEMPERATURE-GRADIENT LIBRARIES

The effect of different process temperatures on polymer properties can be investigated creating libraries with continuous temperature gradients. To achieve this

samples are placed along a temperature-gradient stage [46]. The temperature distribution over the stage is a function of its geometry and the location of the heat source and heat sink elements. For example, a rectangular stage with a heat source in one of its ends and a heat sink (coolant circulation) in the opposite one will generate a linear temperature gradient, if heat loss from the stage edges is neglected.

Temperature gradients can be coupled with composition or thickness gradients, increasing several orders of magnitude the amount of dissimilar process conditions that can be simultaneously studied in one library.

2.3. THEORETICAL BASIS (POLYMER BLENDS)

2.3.1. THERMODYNAMICS AND PHASE BEHAVIOR OF POLYMER BLENDS

Thermodynamics of polymer blends is based on the classical theories of polymer solutions developed by Flory, Huggins, Prigogine, Patterson, Sanchez and others as well as on the theories of phase equilibrium and phase separation in solids developed by Cahn, Prigogine and other authors [47, 48].

In general, studies of “biomedical” polymer blends have focused on specific physical and chemical properties, overlooking the more fundamental thermodynamics of polymer mixing. This is particularly true considering the temperature-dependence of the phase behavior, which is often overlooked in biomedical studies. However, the thermodynamic behavior of polymer blends determines critical equilibrium properties such as compatibility of the components, morphological features, rheological behavior, microphase structure, surface microstructure, and mechanical characteristics of blends [47].

The phase behavior of a polymer blend evolves according to the equilibrium conditions (long-term lowest energy state) and the stability of the initial mixture. When thermodynamics dictates that a single (miscible) phase is the equilibrium, the single-phase system is stable. Any initial inhomogeneity introduced during processing will eventually disappear as the components mix. On the other hand, an initially homogeneous mixture of two immiscible polymers will ultimately approach a phase-separated morphology (inhomogeneous). The equilibrium state and the mechanism of approach to that state are determined by stability considerations according to the following three possibilities:

- The initial mixture is stable in the relation to all other possible phases, and no phase-separation occurs. The free energy of the initial mixture is at a minimum.

- The initial mixture is metastable, in which a lower free energy can be achieved by rearrangement of phases. The phase-separation requires energy input (a nucleation event) to be initiated.

- The initial mixture is unstable in relation to all possible other phase arrangements. An infinitesimally small fluctuation in composition or temperature will lead to spontaneous phase-separation.

When metastable phases are present, the system may stay in the equilibrium state for an indefinitely long time without the appearance of a new phase. If the nuclei of a new, more stable, phase are introduced into the system, the transition to the stable equilibrium state occurs. Of course, all of the phase-transformations (mixing or

separation) are limited by the dynamics of molecular rearrangement of the polymer molecules. Due to their large size and entanglement, polymers can show dramatically long times to reach equilibrium. A stable system is defined thermodynamically as

$$\frac{\partial^2 g}{\partial x_i^{\,2}} > 0 \tag{2.3}$$

where g is the molar Gibbs free energy and x_i is the molar fraction of component i in the blend. This relation is equivalent to the condition $\partial\mu_1/\partial x_1 > 0$, because

$$\frac{\partial \mu_1}{\partial x_2} = -x_2 \frac{\partial^2 g}{\partial x_2^{\,2}} \tag{2.4}$$

And since $\partial\mu_1/\partial x_2 = -x_2\,\partial^2 g/\partial x_2^{\,2}$, then:

$$\frac{\partial \mu_1}{\partial x_2} < 0 \tag{2.5}$$

$$\frac{\partial \mu_2}{\partial x_1} < 0 \tag{2.6}$$

Where μ_i is the chemical potential of component i in the blend.

The transition from a one-phase to a two-phase state is presented in figures 2.9 and 2.10. The boundary between metastability and instability is determined at the point at which $\partial\mu_1/\partial x_2 = 0$. The condition for stability (equations 2.5 and 2.6) for $\left(\partial\mu_1/\partial x_2\right)_{T,P} = -x_2\left(\partial^2 g/\partial x_2^{\,2}\right)_{T,P}$ can be given as:

$$\frac{\partial^2 g}{\partial x_2^{\,2}} > 0 \tag{2.7}$$

This inequality (equation 2.7) has geometric meaning. The function *g* vs. x_2 at constant T and P should be turned down by the convexity for stable systems (Figure 2.9, curve 1). If the curve has the shape 2 or 3 and between some values of x_2 there is a part with the convexity turned up, in this region (AB) the system cannot be in the state of stable equilibrium and decomposes into two phases.

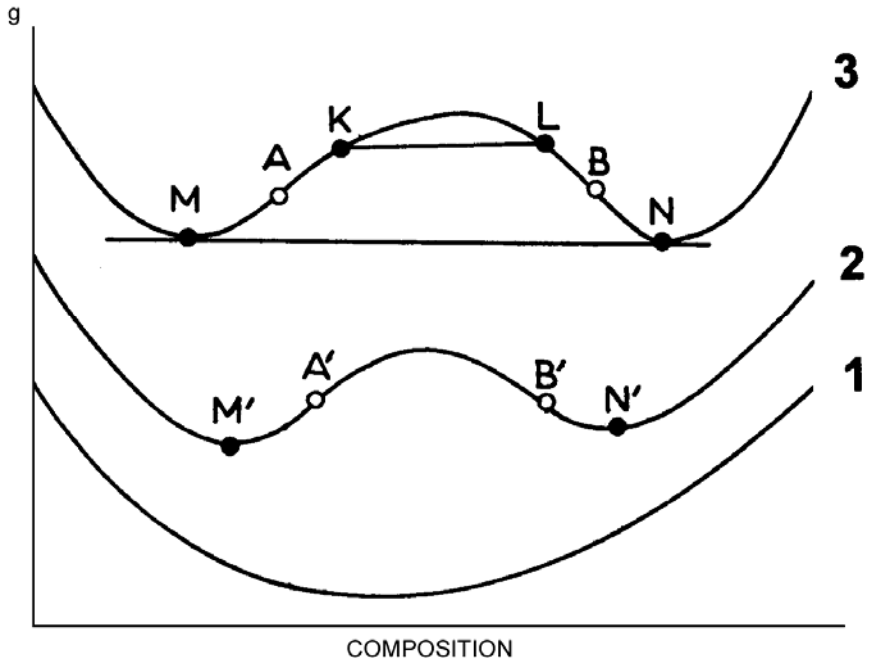

Figure 2.9. Dependence of the Gibbs free energy on the composition (at T and P constant) [47].

The molar fractions x'_2 and x''_2 in these two equilibrium phases can be calculated in the following way: According to Gibbs-Duhem $g = \mu_1 x_1 + \mu_2 x_2$. Differentiation of *g* by x_2 gives $\left(\partial g/\partial x_2\right)_{P,T} = \mu_2 - \mu_1$ or $\mu_2 = g - x_1\left(\partial g/\partial x_1\right)_{P,T}$. The condition of a true equilibrium in relation to the distribution of the component 2 between two phases is $\mu'_2 = \mu''_2$, or:

$$g' - x'_1 \frac{\partial g'}{\partial x'_1} = g'' - x''_1 \frac{\partial g''}{\partial x''_1} \tag{2.8}$$

$$g' - x'_2 \frac{\partial g'}{\partial x'_2} = g'' - x''_2 \frac{\partial g''}{\partial x''_2} \tag{2.9}$$

Subtracting equation 2.9 from equation 2.10, the condition of true equilibrium is found:

$$\left(\frac{\partial g''}{\partial x''_2}\right)_{T,P} = \left(\frac{\partial g'}{\partial x'_2}\right) \tag{2.10}$$

$$g' - g'' = \left(\frac{\partial g'}{\partial x'_2}\right)_{T,P} \left(x'_2 - x''_2\right) \tag{2.11}$$

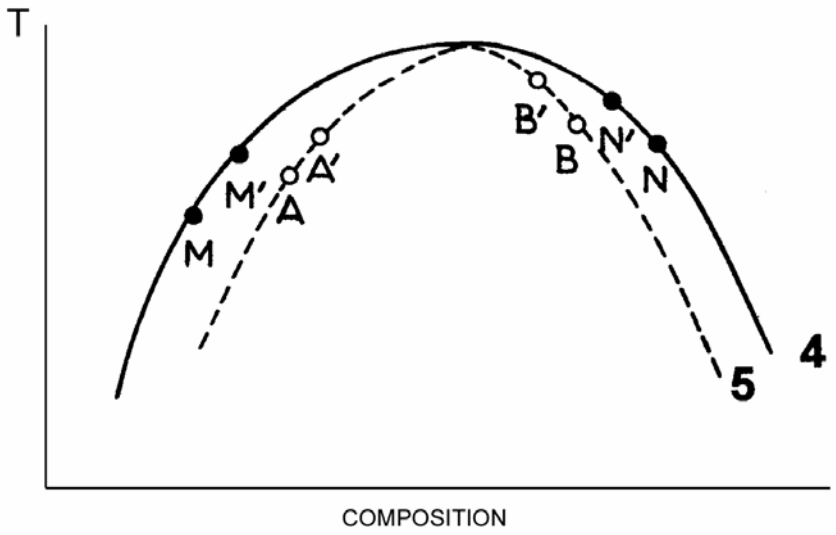

Figure 2..10. Temperature vs. Composition diagram showing binodal and spinodal regions determined by different stable, metastable and unstable states. One-phase region = outside binodal region. two-phase region = inside binodal region [47].

Geometrically equations 2.11 and 2.12 mean that values x_2 corresponding to two phases in the state of equilibrium, i.e., x'_2 and x''_2, have such magnitudes that functions g' and g'' have the common tangent MN (Figure 2.9). The segments MA and NB meet the state of the metastable equilibrium and are inclined to the transformation into a two-phase system. In the interval between two inflection points the condition $\partial g / \partial x_2 < 0$ is

valid. Therefore any solution, having had the fluctuation of concentration in these composition intervals, may spontaneously decompose at the current point K and L (figure 2.9). Such decomposition will be enhanced until the initial solution is separated into two solutions with compositions corresponding to the point M and N (figure 2.9).

In figure 2.10, which shows the different points of figure 2.9 in a temperature-composition diagram, the curve 4, called binodal, is the geometric place of points M and M', N and N', etc. for the curves g = f(x_2) corresponding to various temperatures. Binodal separates the regions of the stable and metastable states of the system. Each point of binodal meets the condition $\partial^2 g/\partial x_2^{\,2} > 0$ and $\mu'_2 = \mu''_2$. Curve 5 (figure 2.10), called spinodal, represents the geometric place of points A and A', B, and B', etc. Spinodal separates the regions of metastable and unstable states. At each point of spinodal $\partial^2 g/\partial x_2^{\,2} = 0$; and at the critical point $\partial \mu_1/\partial x_2 = 0$ and $\partial^2 \mu_1/\partial x_2^{\,2} = 0$. Therefore, in accordance with equation 2.4:

$$\frac{\partial^2 g}{\partial x_2^{\,2}} = 0; \quad \frac{\partial^3 g}{\partial x_2^{\,3}} = 0; \quad \frac{\partial^4 g}{\partial x_2^{\,4}} > 0 \tag{2.12}$$

2.3.2. PHASE SEPARATION, UCST AND LCST

It has been shown that a polymer blend can form either one phase or multiple phases depending on its stability, which is as well related to the composition of the blend and temperature-pressure conditions. But how do we practically determine the stability and equilibrium phases? According to the general principles of thermodynamics, the formation of a thermodynamically stable system is characterized by a decrease in Gibbs free energy, ΔG:

$$\Delta G = \Delta H - T\Delta S \tag{2.13}$$

The necessary but not sufficient condition for the system stability is that $\Delta G < 0$, which can be attained if $\Delta H < 0$ and $T\Delta S > 0$, or if $\Delta H < 0$ and $|T\Delta S| > |\Delta H|$. However, experimental determination of ΔG for polymer blends is particularly difficult, since traditional methods such as those used in polymer-solvent systems are not applicable to polymer mixtures. Initially it was suggested that during mixing of two polymers having a high molecular mass, the change in enthalpy is responsible for mixing, and that contribution of entropy of mixing to ΔG should be extremely small. For this case, the system was considered miscible (compatible) if $\Delta H < 0$, following the rule for miscibility of a polymer solution in low-molecular mass liquids (regular solution), and immiscible (incompatible) if $\Delta H > 0$. However, it has been shown that for polymer blends this condition is not true and that contribution of entropy cannot be neglected. Multiple works [49-51] have evaluated the entropy of mixing of two polymers and shown that it is not always close to zero ($\Delta S \to 0$) as proposed before, but it can also diminish ($\Delta S < 0$), which is characteristic of miscible polymers [49], or increase ($\Delta S > 0$) (figure 2.11).

Is necessary to note that the consideration that thermodynamic compatibility or incompatibility of the components, which is the main characteristic of polymer blends, is governed by the phase diagram of the system; is in principle incorrect. The reason is that compatibility depends on many other factors besides temperature and composition. In general there are almost no fully incompatible or compatible pairs of polymers, but various conditions exist at which a polymer pair can be miscible or immiscible. The degree of miscibility is dictated by the chemical constitution of mixed components, and may be very broad, or, on the contrary, very narrow.

The term "compatibility" is widely used in literature. However, it is also used to describe good adhesion between the constituents, average of mechanical properties and other characteristics of blends. It is then more accurate to describe the thermodynamic

behavior of polymer mixtures by using the term "miscibility". Miscibility is used to describe polymer-polymer blends with similar behavior to that of a single phase system. However, it does not imply ideal molecular mixing but, suggests that the level of molecular mixing is adequate to yield similar macroscopic properties as those expected for a single-phase material.

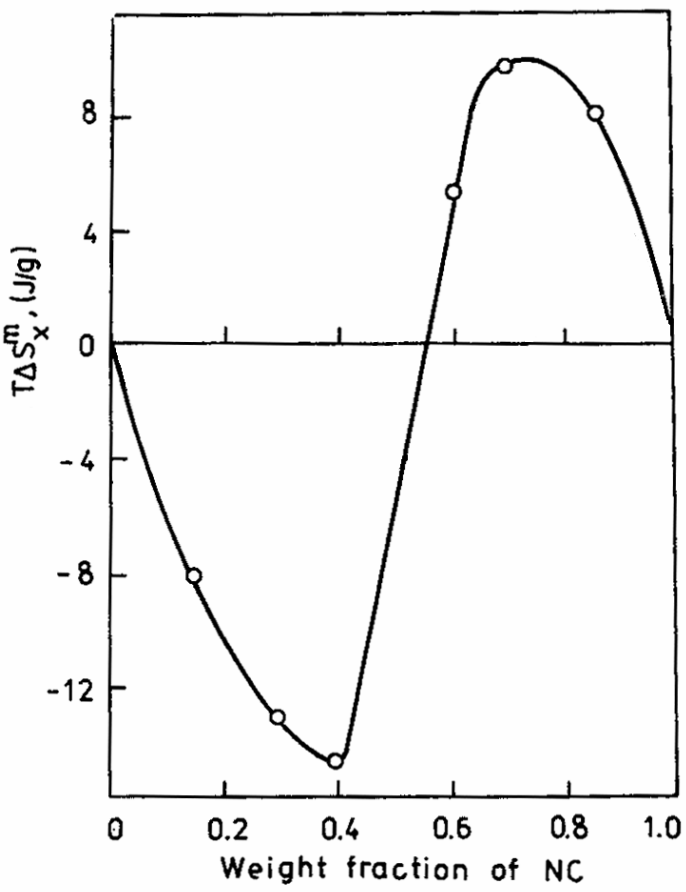

Figure 2.11. Entropy of mixing as a function of composition (cellulose acetate–cellulose nitrate mixture) [49].

The first attempt to thermodynamically describe polymer blends was made by Flory [50] and Huggins [52] based on approximations to the regular solution theory, conserving important considerations of this theory such as mixtures of perfectly spherical

molecules of equal size, and assuming that *no volume change* takes place during mixing; proposed the following equation for the Gibbs free energy of mixing (Flory-Huggins equation):

$$\Delta G = \frac{RT}{V_S}\left[\frac{\varphi_A}{r_A}\ln\varphi_A + \frac{\varphi_B}{r_B}\ln\varphi_B + \chi_{AB}\varphi_A\varphi_B\right] \tag{2.14}$$

Where V_s is the volume of segment taken equal to the volume of repeating unit of the polymer chain (the same for both polymers), r_A and r_B are the numbers of segments of polymer A and B, $r_i = V_i/V_S$ (V_i is the molar volume of component *i*), φ_A and φ_B are volume fractions of components, χ_{AB} is a thermodynamic interaction parameter, called the Flory-Huggins interaction parameter, related to the interaction between different segments of volume V_S.

Initially χ_{AB} was related only with the heat or energy change on mixing ΔH (pure enthalpic contribution), proportional to the change in interaction energy $\Delta\omega$, defined as the energy involved in the formation in the mixture of new contacts of the type A-B that replace some of the initial A-A and B-B contacts of the pure components, where the A and B units occupy the cells of a “regular lattice” with coordination number *z* (figure 2.12). This interaction was assumed to be effective only between nearest neighbors only (figure 2.13), and can be described by the following quasi-chemical process:

$$1/2(A-A) + 1/2(B-B) \quad \rightarrow \quad (A-B) \tag{2.15}$$

$\Delta\omega$ can be defined in terms of the contact energies ε_{ij} required to break the links showed in equation 2.16:

$$\Delta H \propto \Delta\omega = \varepsilon_{AB} - \frac{1}{2}(\varepsilon_{AA} + \varepsilon_{BB}) \tag{2.16}$$

$$\chi_{AB} = \frac{z\Delta\omega}{RT} \tag{2.17}$$

Where z is the lattice coordination number.

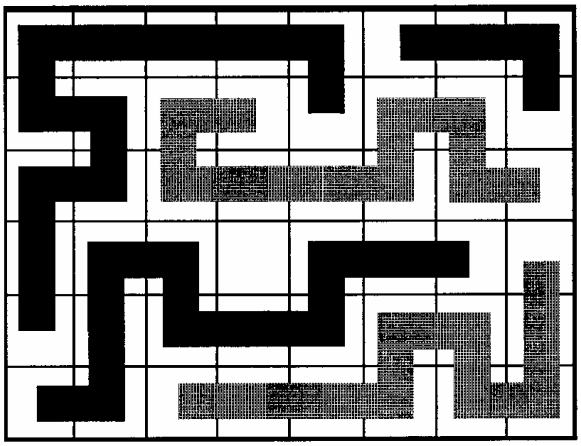

Figure 2.12. Lattice model of a polymer mixture. Structure units of equal size [53].

χ_{AB} represents an antipathy between the molecules of different type since it is the ratio of the positive interchange energy, acting against mixing, to the thermal energy favoring mixing [54].

A different approximation for χ_{AB}, referred as the Scott's approach, is based on the cohesive energy density of the blend components (C_{ii}), where multiple molecule-molecule interactions are considered (figure 2.14) instead of just pair interactions. The cohesive energy for each component is given by:

$$C_{AA} = \frac{n_A z \varepsilon_{AA}}{2V_A}; C_{BB} = \frac{n_B z \varepsilon_{BB}}{2V_B} \tag{2.18}$$

Where n_i is the number of molecules of component i.

The cohesive energy of the mixture is approximated to a geometric mean of the cohesive energies of the pure components:

$$C_{AB} = \sqrt{C_{AA} C_{BB}} \tag{2.19}$$

And the change in energy due to mixing is given by:

$$\Delta E \approx (C_{AA} + C_{BB} - 2C_{AB}) = \left(\sqrt{C_{AA}} - \sqrt{C_{BB}}\right)^2 \tag{2.20}$$

$\sqrt{C_{ii}}$ is defined as the solubility parameter of component *i* δ_i. Therefore:

$$\Delta E \approx \left(\delta_A - \delta_B\right)^2 \;\; \therefore \;\; \chi_{AB} \approx \frac{V_s}{RT}\left(\delta_A - \delta_B\right)^2 \tag{2.21}$$

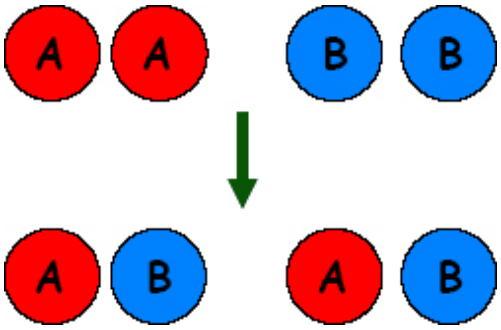

Figure 2.13. Formation of new contacts of the type A-B after mixing pure components A and B.

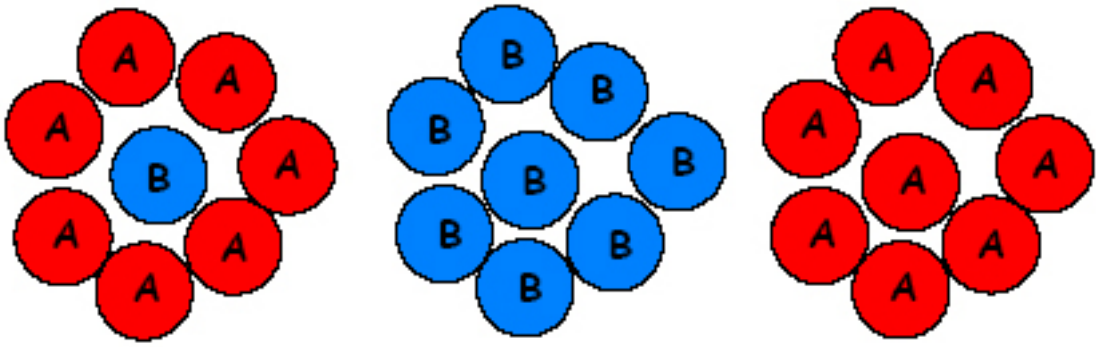

Figure 2.14. Multiple molecule-molecule interaction representation (mixture AB, pure component B and pure component A). Cohesive energy density model.

It's worth noting that the Scott's approach expression predicts that a polymer pair is miscible only when their solubility parameters are almost equal.

Scott's approach (equation 2.22) shows that the interaction factor χ_{AB} is always positive and decreases monotonically as temperature increases ($\chi_{AB} = f(1/T)$). This means that the third term on the right hand side of the Flory equation (equation 2.15) is positive. The other two terms constitute the negative combinatorial entropy of mixing ($-\Delta S$), also referred as "translational entropy" which for polymer mixing is *very small* and vanishes in the limit of infinite molecular weight ($r_A, r_B \to 0$). Hence:

$$\Delta G = \frac{RT}{V_S}\left[\frac{\varphi_A}{r_A}\ln\varphi_A + \frac{\varphi_B}{r_B}\ln\varphi_B + f\left(\frac{1}{T}\right)\varphi_A\varphi_B\right] \begin{cases} \frac{\varphi_A}{r_A}\ln\varphi_A + \frac{\varphi_B}{r_B}\ln\varphi_B \to \text{Small and negative} \\ f\left(\frac{1}{T}\right)\varphi_A\varphi_B \to \text{Always positive} \end{cases}$$

Consequently $\Delta G > 0$ at low temperatures, meaning that the system is unstable and segregates into two separate phases. As temperature rise the positive term involving the interaction factor starts to become less and less significant until $\Delta G < 0$, and the phases become miscible. This is called the Upper Critical Solution Temperature behavior or UCST (figure 2.15), where the upper critical solution temperature is the maximum temperature of the boundary between the one-phase and the two-phase regions. Binodal and spinodal curves meet at the UCST.

Experimental work showed mismatches in the value of χ_{AB} determined from independent measurements of ΔG and ΔH, leading to a modification of the theory and a reinterpretation of $\Delta\omega$ as an *interchange free energy* with an enthalpic contribution $\Delta\omega_H$ (as seen on equation 2.18) plus an entropic one $\Delta\omega_S$ [54, 55]. Therefore:

$$\Delta\omega \rightarrow \Delta\omega_G = \Delta\omega_H - T\Delta\omega_S \tag{2.22}$$

$$\chi_{AB} = \chi_H + \chi_S \;\; ; \;\; \chi_H = \frac{z\Delta\omega_H}{RT} \quad \chi_S = -\frac{z\Delta\omega_S}{k} \tag{2.23}$$

The entropy $\Delta\omega_S$ was found to be positive, corresponding to idea of an increase in entropy due to the forming of new contacts A-B, and thus χ_S was a negative correction [54]. This allowed the interaction parameter to be negative as well [53]. The new model of the interaction factor, in the form $\chi_{AB} = a/T + b$, shows the same monotonically decreasing behavior as temperature increases as the initial model (equation 2.18). UCST behavior is still described by this model.

Further work on polymer solutions and blends [51] showed that the "small negative correction" χ_S can also be positive and a lot larger than χ_H, which means an inexplicable, large increase of order on forming A-B contacts (the positive sign on χ_S corresponds to a negative sign in $\Delta\omega_S$). Additional experimental data [56] showed evidence that certain solutions present a critical solution temperature at *high* temperatures, above which phase separation into two phases takes place. This behavior cannot be explained by the initial theory, and suggested that the entropic contribution of the interaction parameter could be positive —as seen before experimentally—, and could outweigh by a large margin the combinatorial entropy (ΔS). The new critical temperature is called Lower Critical Solution Temperature or LCST since it lies at the bottom of a two-phase region (figure 2.16).

The presence of LCST and a positive entropic contribution of the interaction factor can be explained by the effect of the dissimilarity in free volume between the pure polymers and the blend (not taken into account in the initial theory). It is observed generally that a homogeneous mixing of two polymer results in a volume shrinkage. This

decrease in the “free volume” available for local motions of the monomers, called “densification”, leads to a reduction of lattice sites which as well reduces the translational (or combinatorial) entropy [53].

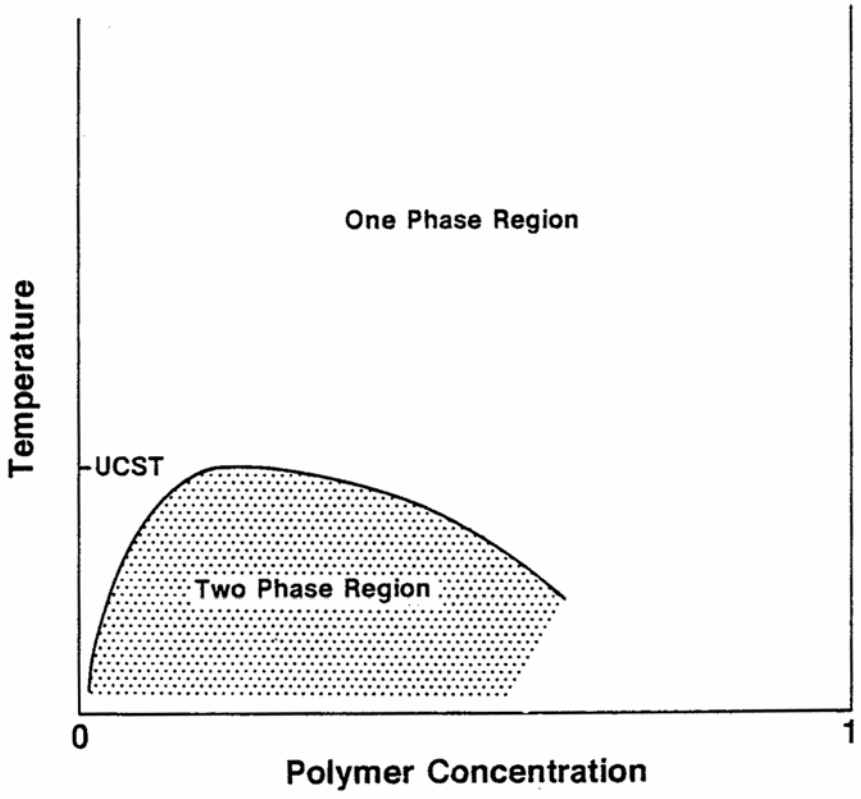

Figure 2.15. Schematic diagram for a polymer blend that exhibits upper critical solution temperature behavior (UCST) [48].

Figure 2.17. Shows the different behaviors of χ_{AB} depending on the effect of energy and volume dissimilarities. Curve 1 shows an enthalpic dominant effect over the entropic contribution ($\chi_H >> \chi_S$), especially at low temperatures. In curve 2, mainly at high temperatures, the entropic effect due to the volume dissimilarity (free volume effect) overcompensates the initially dominating attractive interactions ($\chi_S >> \chi_H$).

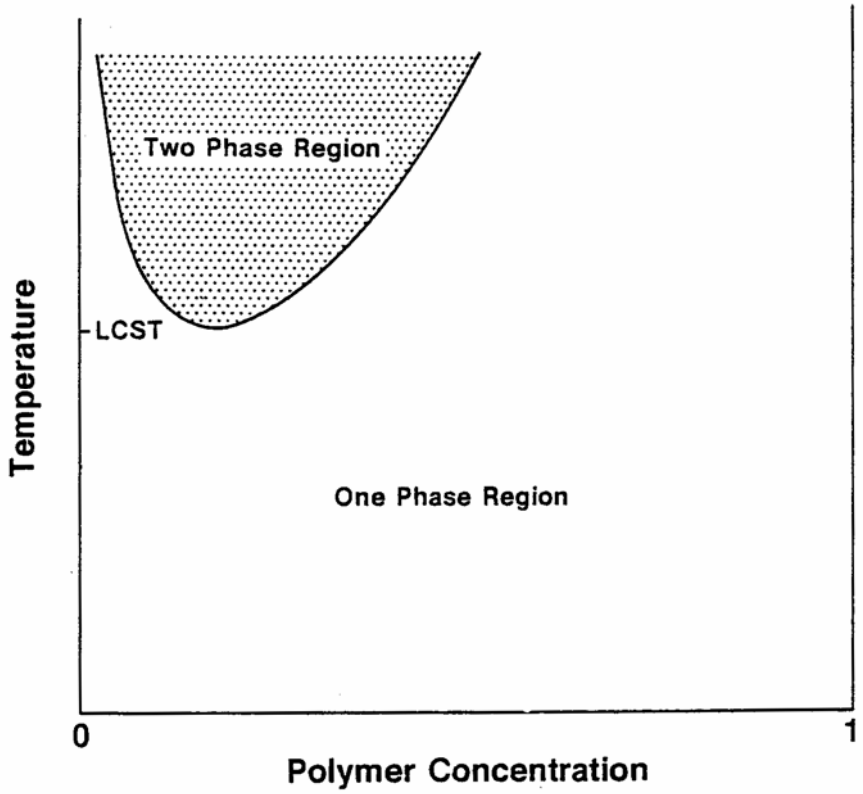

Figure 2.16. Schematic diagram for a polymer blend that exhibits lower critical solution temperature behavior (LCST) [48].

Curve 1 is typical for blends that present UCST behavior, since high positive values of χ_{AB} that outweigh the combinatorial entropy, inducing phase separation, exist at low temperatures. On the other hand, the interaction factor of blends that show LCST behavior follows curve 2, since high values of χ_{AB} occur at high temperatures. Therefore UCST is driven by unfavorable energetic effects (high energy dissimilarity), and LCST is entropically driven (unfavorable or high volume dissimilarity which leads to densification). The value of χ_{AB} at which a two-phase region starts is called the critical interaction factor χ_C.

Curve 3 in figure 2.17 is characteristic of systems that show both LCST and UCST behavior, where attractive interactions dominate at low temperatures and entropic effects at high ones. In this case χ_{AB} crosses χ_C twice.

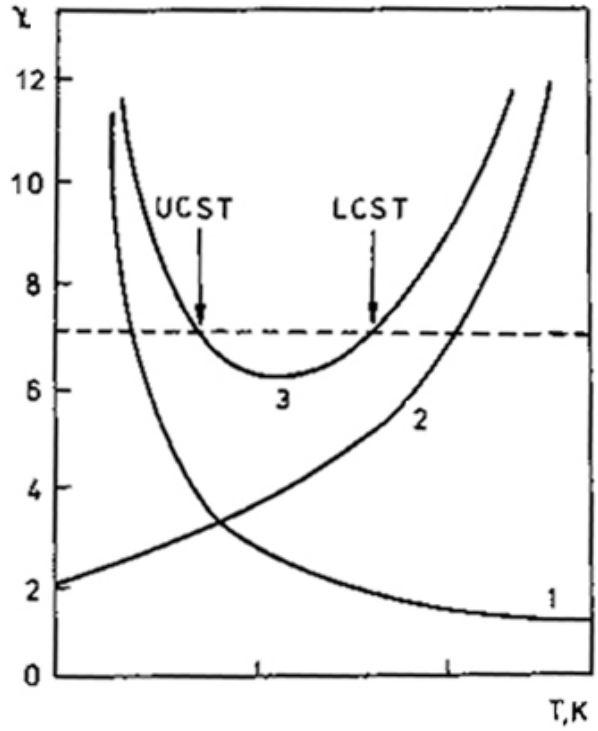

Figure 2.17. Temperature dependence of the interaction parameter: curve (1), contribution due to contact energy dissimilarity; curve (2), contribution due to free volume dissimilarity; curve (3), χ_S for mixtures with UCST *and* LCST [47, 54]. Dashed line corresponds to χ_C.

Phase separation can occur by two different mechanisms, namely, spinodal decomposition, and nucleation and grow. The mechanism followed depends on the location of the binary mixture in the two-phase diagram. Therefore if the temperature jump that brings the mixture inside the two-phase region falls in between the binodal and spinodal curves (equivalent to any point in between points M and A or N and B in figure 2.9) nucleation and growth will take place, if on the contrary it falls inside the spinodal region (region in between points A and B figure 2.9), then spinodal decomposition will

occur. However, the final structure is *always* the same independent of the mechanism by which phase separation started (figure 2.18) [53].

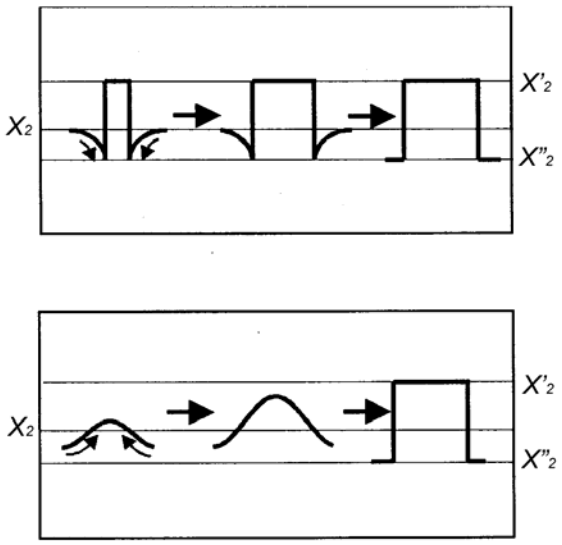

Figure 2.18. Mechanisms of phase separation: Nucleation and growth (top) and spinodal decomposition (bottom) [53].

In summary, due to the fact that the translational entropy is usually extremely small (vanishing in the limits of high molecular weights), positive values of the interaction parameter almost always lead to incompatibility. If the interaction parameter is negative, then mixing takes place.

Additional models based on the Flory-Huggins theory that present different approximations to the thermodynamic parameter of interaction, and equation-of-state models to describe the phase behavior of polymer blends, like the Sanchez-Lacombe, Walker-Vause and Holten-Anderson models can be found elsewhere [47, 48, 53, 55].

REFERENCES

1. **Lee J.H., Jung H.W., Kang I., and Lee H.B., *Cell Behaviour on Polymer Surfaces with Different Functional Groups.* Biomaterials, 1994. 15(9): p. 705-711.**

2. **Huang S., Chen C.S., and Ingber D.E., *Control of Cyclin D1, p27^{Kip1}, and Cell Cycle Progression in Human Capillary Endothelial Cells by Cell Shape and Cytoskeletal Tension.* Molecular Biology of the Cell, 1998. 9: p. 3179-3193.**

3. **Hatano K., Inoue H., Kojo T., Matsunaga T., Tsujisawa T., Uchiyama C., and Uchida Y., *Effect of surface roughness on proliferation and alkaline phosphatase expression of rat calvarial cells cultured on polystyrene.* Bone, 1999. 25(4): p. 439-445.**

4. **Soboyejo W.O., Nemetski B., Allameh S., Marcantonio N., Mercer C., and Ricci J., *Interactions between MC3T3-E1 cells and textured Ti6Al4V surfaces.* J Biomed Mater Res, 2002. 62: p. 56-72.**

5. **Webb K., Hlady V., and Tresco P.A., *Relative importance of surface wettability and charged functional groups on NIH 3T3 fibroblast attachment, spreading, and cytoskeletal organization.* J Biomed Mater Res, 1998. 41: p. 422-430.**

6. **Washburn N.R., Yamada K.M., Simon Jr. C.G., Kennedy S.B., and Amis E.J., *High-throughput investigation of osteoblast response to polymer crystallinity: influence of nanometer-scale roughness on proliferation.* Biomaterials, 2004. 25: p. 1215-1224.**

7. **Meredith J.C., Sormana J.L., Keselowsky B.G., García A.J., Tona A., Karim A., and Amis E.J., *Combinatorial Characterization of Cell Interactions with Polymer Surfaces.* Journal of Biomedical Materials Research, 2003. 66A: p. 483-490.**

8. **Brocchini S., James K., Tangpasuthadol V., and Kohn J., *Structure-property correlations in a combinatorial library of degradable materials.* Journal of Biomedical Materials Research, 1998. 42: p. 66-75.**

9. **Schakeraad J.M., *Cells: Their surfaces and interactions with materials*, in *Biomaterials Science: An introduction to materials in medicine*, H.A.S. Ratner B.D., Schoen F.J., and Lemons J.E., Editor. 1996, Academic Press: San Diego, CA. p. 484.**

10. **Alberts B., Bray D., Lewis J., Raff M., Roberts K., and Watson J.D., *Molecular Biology of the Cell*. 1989, New York: Garland Publishing, Inc. 1264.**

11. **Buck C.A., Horwitz A.F., *Integrin, a transmembrane glycoprotein complex mediating cell-substratum adhesion.* J. Cell. Sci. Suppl., 1987. 8: p. 231-250.**

12. **Miranti C.K., Brugge J.S., *Sensing the environment: a historical perspective on integrin signal transduction.* Nature Cell Biology, 2002. 4: p. 83-90.**

13. **Burridge K., Chrzanowska-Wodnicka M., *Focal adhesions, contractility, and siganling.* Annu. Rev. Cell Dev. Biol., 1996. 12: p. 463-519.**

14. **Meredith Jr. J.E., Fazeli B., and Schwartz M.A., *The Extracellular Matrix as a Cell Survival Factor.* Molecular Biology of the Cell, 1993. 4: p. 953-961.**

15. **Culp L.A., *Biochemical Determinants of Cell Adhesion.* Current Topics in Membranes and Transport, 1978. 2: p. 327-396.**

16. **Horbett T.A., *Proteins: structure, properties, and adsorption to biomaterials*, in *Biomaterials Science: An introduction to materials in medicine*, H.A.S. Ratner B.D., Schoen F.J., and Lemons J.E., Editor. 1996, Academic Press: San Diego, CA. p. 484.**

17. **Schakeraad J.M., Busscher H.J, Wildevuur C.R., and Arends J., *The influence of substratum surface free energy on growth and spreading of human fibroblasts in the presence and absence of serum proteins.* J Biomed Mater Res, 1986. 20(773-784).**

18. **Chehroudi B., Brunette D.M., *Effects of Surface Topography on Cell Behavior*, in *Encyclopedic Handbook of Biomaterials and Bioengineering*, D.J. Wise, Altobelli D.E., Yaszenski M.J., Gresser G.D., and Schwartz E.R., Editor. 1995, Dekker: New York. p. 813-842.**

19. **Curtis A., Riehle M., *Tissue engineering: the biophysical background.* Phys. Med. Biol., 2001. 46: p. R47-R65.**

20. **Ratner B.D., Hoffman A.S., Schoen F.J., and Lemons J.E., ed. *Biomaterials Science: An introduction to materials in medicine*. 1 ed. 1996, Academic Press: San Diego, CA. 484.**

21. **Park K., Shalaby W.S., and Park H., *Biodegradable hydrogels for drug delivery*. 1 ed. 1993, Lancaster: Technomic Pub Co. 252.**

22. **Domb J.A., Kost J., and Wiseman D.M., ed. *Handbook of biodegradable polymers*. 1 ed. Drug targeting and delivery, ed. A. Florence, G. Gregoriadis. Vol. 7. 1997, Harwood academic publishers: Amsterdam. 526.**

23. **Göpferich A., *Mechanisms of polymer degradation and erosion.* Biomaterials, 1996. 17: p. 103-114.**

24. **Vert M., Feijen J., Albertson A., Scott G., and Chiellini E., *Degradable polymers and plastics*. 1992, England: Redwood Press Ltd. 302.**

25. **Williams D.F, ed. *Definitions in Biomaterials: Proceedings of a Consensus Conference of the European Society for Biomaterials*. 1987, Elsevier Science: New York. 72.**

26. **Reed A.M., Gilding D.K., *Biodegradable polymers for use in surgery - poly(glycolic)/poly(lactic acid) homo and copolymers: 2. In vitro degradation.* Polymer, 1981. 22(4): p. 494-498.**

27. **Engelberg I., Kohn J., *Physicomechanical properties of degradable polymers used in medical applications: A comparative study.* Biomaterials, 1991. 12: p. 292-304.**

28. **Ginde R.M, Gupta R.K., *In-vitro chemical degradation of poly(glycolic acid) pellets and fibers.* Journal of Applied Polymer Science, 1987. 33(2411-2429).**

29. **Meredith J.C., Amis E.J., *LCST phase separation in biodegradable polymer blends: poly(D,L-lactide) and poly(ε-caprolactone).* Macromol. Chem. Phys., 2000. 201(6): p. 733-739.**

30. **Broz M.E., VanderHart D.L., and Washburn N.R., *Structure and mechanical properties of poly(d,l-lactic acid)/poly(ε-caprolactone) blends.* Biomaterials, 2003. 24: p. 4181-4190.**

31. **Kalfogu N.K., *Compatibility of low density polyethylene-poly(ε-caprolactone) blends.* Journal of Applied Polymer Science, 1983. 28: p. 2541-2551.**

32. **Allcock H.R., Lampe F.W., *Contemporary polymer chemistry*. 2 ed. 1990, New Jersey: Prentice Hall. 624.**

33. **Macaúbas P.H., Demarquette N.R., *Rheology as a Tool for Immiscible Polymer Blends Characterization:Interfacial tension and compatibilization*, in *RheoFuture*. 2002, Thermo Electron Coporation: Karlsruhe, Germany.**

34. **Utraki L.A., *Polymer alloys, blends.* 1990, Munich: Hanser Publishers. 356.**

35. **Harper C.A., ed. *Handbook of plastics, elastomers and composites*. 4 ed. 2002, McGraw-Hill Professional. 884.**

36. **Chicurel M.E., *Faster, better, cheaper genotyping.* Nature, 2001. 412: p. 580-582.**

37. **Holm A., Molander P., Lundanes E., and Greibrokk T., *Novel column oven concept for cold spot large volume sample enrichment in high throughput temperature gradient capillary liquid chromatography.* Journal of Separation Science, 2003. 26: p. 1147-1153.**

38. **Cawse J.N., Wroczynski R., *Combinatorial materials development using overlapping gradient arrays: Designs for efficient use of experimental resources*, in *Experimental design for combinatorial and high throughput materials development*, J.N. Cawse, Editor. 2003, John Wiley & Sons, Inc.: Hoboken. p. 109-127.**

39. **Wolf D., Baerns M., *An evolutionary strategy for the design and evaluation of high throughput experiment*, in *Experimental design for combinatorial and high throughput materials development*, J.N. Cawse, Editor. 2003, John Wiley & Sons, Inc.: Hoboken. p. 147-161.**

40. **Holeña M., Baerns M., *Artificial neural networks in catalyst developmen*, in *Experimental design for combinatorial and high throughput materials development*, J.N. Cawse, Editor. 2003, John Wiley & Sons, Inc.: Hoboken. p. 163-202.**

41. **Potyrailo R.A, Lemmon J.P., and Leib T.K., *High-Throughput screening of selectivity of melt polymerization catalysts using fluorescence spectroscopy and two-wavelength fluorescence imaging.* Analytical Chemistry, 2003. 75(17): p. 4676-4681.**

42. **Schneemeyer L.F., van Dover R.B., Madsen C.K., and Claypool C.L., *The compositional spread approach to high dielectric constant materials and materials for integrated optics*, in *Combinatorial materials development*, R. Malhotra, Editor. 2002, American Chemical Society: Washington, DC. p. 49-64.**

43. **Meredith J.C., *A Perspective on High-Throughput Polymer Science.* Journal of Materials Science, 2003. in press (October 2003 Issue).**

44. **Meredith J.C., Karim A., and and Amis E.J., *High-Throughput Measurement of Polymer Blend Phase Behavior.* Macromolecules, 2000. 33: p. 5760-5762.**

45. **Karim A., Sehgal A., Amis E.J., and Meredith J.C., *Combinatorial mapping of polymer blends phase behavior*, in *Experimental design for combinatorial and high throughput materials development*, J.N. Cawse, Editor. 2003, John Wiley & Sons, Inc.: Hoboken. p. 73-88.**

46. **Meredith J.C., Smith A.P., Karim A., and Amis E.J., *Combinatorial Materials Science for Polymer Thin-Film Dewetting.* Macromolecules, 2000. 33: p. 9747-9756.**

47. **Lipatov Y.S., Nesterov A.E., *Thermodynamics of polymer blends*. 1 ed. Polymer thermodynamics library. Vol. 1. 1997, Lancaster: Technomic Publishing Co., Inc. 450.**

48. **Sandler S.I., ed. *Models for thermodynamic and phase equilibria calculations*. 1 ed. Chemical Industries, ed. H. H. Vol. 52. 1994, Marcel Dekker, Inc: New York. 686.**

49. **Tager A.A., Scholokhovich T.I., and Bessonov J.S., *Thermodynamics of mixing of polymers.* European Polymer Journal, 1975. 11(4): p. 321-326.**

50. **Flory P.J., Eichinger B.E., and Orwoll R.A., *Thermodynamics of Mixing Polymethylene and Polyisobutylene.* Macromolecules, 1968. 1(3): p. 287-288.**

51. Tompa H., *Polymer solutions*. 1956, New York: Academic Press. 325.

52. Huggins M.L., *Physical chemistry of high polymers*. 1958, New York: Wiley. 175.

53. Strobl G., *The physics of polymers*. 2 ed. 1997, Berlin: Springer. 439.

54. Patterson D., *Free volume and polymer solubility.* Macromolecules, 1969. 2(6): p. 672-677.

55. Gedde U.W., *Polymer physics*. 1 ed. 1996, London: Chapman & Hall. 298.

56. Freeman P. I., Rowlinson J.S., *Lower critical points in polymer solutions.* Polymer, 1960. 1: p. 20-26.

CHAPTER III

PREPARATION AND CHARACTERIZATION OF PCL/PDLA POLYMER BLEND THIN FILM LIBRARIES

3.1. INTRODUCTION

In general it is not easy to find a polymer that meets all the desired characteristics for a particular application. For example polymers with ideal biodegradability and biocompatibility properties can have unfavorable mechanical properties, and vice versa. A way to address this problem in an effective manner and tune the material properties to satisfy the application requirements is to blend two or more polymers.

The mechanical response of polymers can be defined as a competition between plastic and elastic deformation [1]; therefore, blending can be a useful way to obtain materials with specific properties since the resultant properties of the blend can vary drastically in comparison to those of its constituents [2, 3]. For example, brittle polymers with high tensile modulus can be “strengthened” by blending them with more elastomeric (rubbery) ones. The result is a material with higher percentage of elongation at break, translated into enhanced resistance to fracture when compared to the brittle component, and with a higher tensile modulus (stiffer) when compared to the more elastomeric one. It can be readily seen then that mechanical properties can be tailored from soft elastomerics to rigid engineering plastics by blending different polymers.

In the same way blending can affect in a noticeably way several other characteristics such as hydrophobicity/hydrophilicity, degradation rate, solubility, and

surface structure and roughness, among many others; making it a valuable tool to adjust polymer behavior for specific purposes.

Biological tissues are often flexible and elastic, ranging from skin and muscle to bone and tendon; and biomaterials must be able to operate in a specific application by interacting with these biological systems. Therefore engineered biomaterials must have physicomechanical properties closely matching those of the biological structure they are intended to replace or interact with. In tissue engineering, for example, the main purpose is to create scaffolds, generally of polymeric materials, that provide a suitable environment for reconstruction of functional tissue [4]. Degradable polymers like polydioxanone, polyanhydrides and polyesters have been considered for such purposes [5], the latter being the most common used ones, specifically the derivatives of lactic and glycolic acids. These are among the few degradable polymers that have extensive regulatory approval by the FDA [6-9], and have been widely explored as three dimensional polymer scaffolds for cell transplantation [10].

Pure lactides and glycolides have high glass transition temperatures (above room temperature) and high tensile modulus (table 2.3, chapter 2) [7, 11, 12], being therefore hard and brittle and not suitable for many tissue engineering applications. A common approach to address this issue is to blend these materials with a lower modulus material to make them tougher and more flexible. As mentioned before, the lower modulus material can relieve stress from the higher modulus one when put under load or tension via plastic or elastic deformation. Poly(ε-caprolactone), also an FDA-approved polymer, has a low glass transition temperature, a modulus an order of magnitude lower than lactides and glycolides, and much higher elongation at break (table 2.3, chapter 2). This makes PCL a reasonable candidate for toughening lactide and glycolide-based polymers.

Mechanical testing of PCL/PDLA blends has been done by Broz and coworkers [12], showing that the mechanical properties of the blend can be tuned through the blend composition. The average modulus, tensile strength and strain-at-failure can be varied continuously by almost an order of magnitude. The results of these tests are in accordance to the expected behavior of a blend of high and low tensile modulus polymers. The strain-at-failure decreases monotonically from a PDLA mass fraction of 0 to 0.5, consistent with diluting the PCL matrix with PDLA inclusions; and reaches an almost constant value above a PDLA mass fraction of 0.5, consistent with the glassy PDLA phase forming a brittle matrix (figure 3.1a).

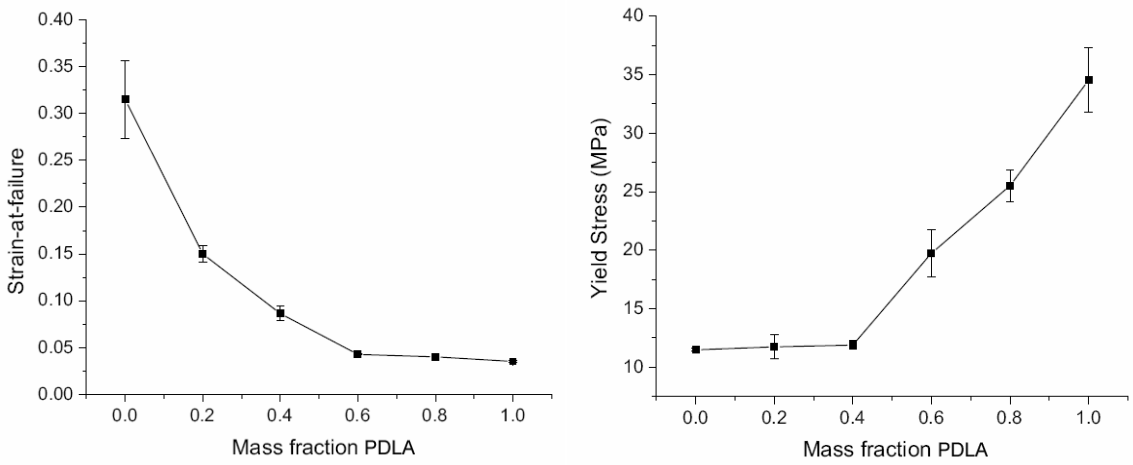

Figure 3.1. a) Strain-at-failure of PCL-PDLA blends as a function of composition. b) Yield stress as a function of blend composition for a PCL/PDLA polymeric blend [12].

Conversely, the yield stress has a near-constant value at concentrations of PDLA up to 0.4, suggesting toughening at the PCL/PDLA interface. Above that concentration the tensile stress increases in a monotonic way suggesting that PCL blending in this regime simply dilutes the PDLA matrix like the presence of voids in the material (figure 3.1b).

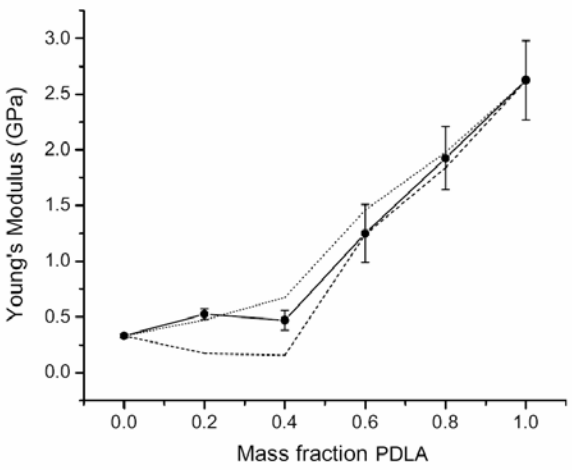

Figure 3.2. Plot of Young's modulus as a function of PCL/PDLA blend composition (solid line). Kerner-Uemura-Takayanagi model: assuming perfect adhesion (dotted line) and zero adhesion (dashed line) [12].

Blending of PCL with PDLA in fact shows improvements in mechanical properties from the tissue engineering point of view, namely, increasing in the strain-at-failure and decreasing in tensile strength. However phase behavior of PCL/PDLA blends is complicated and critically related with their mechanical properties. For example, Young's modulus plotted as a function of composition (figure 3.2) for PCL/PDLA blends is compared to predictions of the two variations of the Kerner-Uemura-Takayanagi model: one that assumes zero adhesion at the blend interface (dashed line figure 3.2), and one that assumes perfect adhesion (dotted line figure 3.2). The actual modulus (solid line figure 3.2) goes from fitting the perfect adhesion model in the range of 0 to 0.3 mass fraction of PDLA, to fit the zero adhesion model at PDLA mass fractions above 0.6; showing the effect of microphase structures.

The work by Broz et al [12] shows the potential of using PCL to mechanically enhance brittle lactides and glycolides. However, further development requires detailed knowledge of phase behavior of the blend, namely, the correlation of phase boundaries

(LCST and/or UCST) and their microstructure with process variables such as temperature and composition.

Meredith and Amis [7], reported the existence of a low critical solution temperature (LCST) phase transition for PCL/PDLA blends. Laser light scattering was used to measure the cloud points while scanning over different ranges of temperatures and compositions. The LCST cloud point curve, with critical point at 86°C and mass fraction of 36% PCL, is shown in figure 3.3.

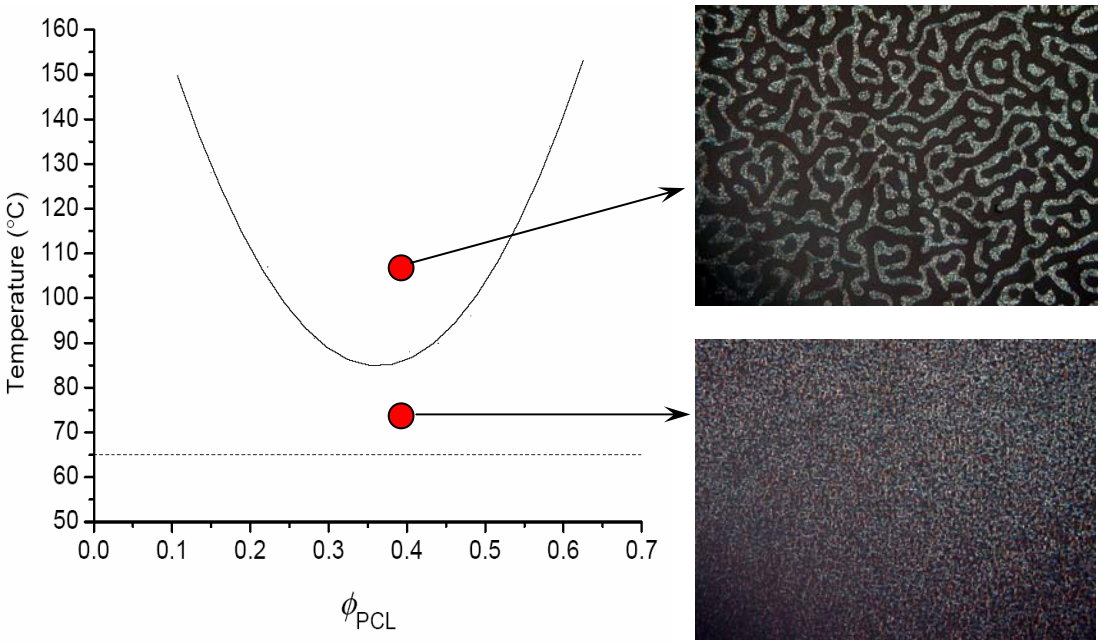

Figure 3.3. LCST cloud point curve for the PCL/PDLA system. One-phase region below LCST boundary (parabola-like curve). Two-phase region above LCST boundary [7].

Different surface morphologies dependent on both composition and temperature are reported throughout the two-phase region (figure 3.3). The control of these surface microstructures may lead to a successful manipulation of physicomechanical and interfacial properties of biomaterials based on PCL/PDLA blends. However, this approach is not without limitations, detailed characterization of surface microstructure,

i.e., roughness, microdomain dispersion, and interfacial adhesion at the microphase boundaries, as a function of temperature and composition has to be performed. The variable space involved in such characterization becomes a major blockade since it easily overpowers traditional experimental methods that rely on one-sample/one-measurement procedures. Novel combinatorial libraries [13, 14] with orthogonal composition and temperature gradients will be used to tackle this problem, covering extensive ranges of temperature and composition of PCL/PDLA blends in a single sample.

3.2. EXPERIMENTAL METHODS

3.2.1. COMPOSITION-GRADIENT LIBRARY PREPARATION

Thin film PCL/PDLA libraries with *linear* composition gradients were prepared following the gradient-film coating technique outlined in section 2.2.9.1.

For the mixing step, the infusion rate of PCL (I_{PCL}) was chosen to be half of the sum of the withdrawal (W) and sampling (S) rates, $I_{PCL} = (W + S)/2$, as required by the transient mass balance [13] (equation 3.1) to obtain a *linear* PCL/PDLA gradient:

$$X_{PDLA} = X_{PDLA,0}\left[\frac{(I_{PCL} - W - S)t + M_0}{M_0}\right]^{-\frac{I_{PCL}}{(I_{PCL}-W-S)}} \tag{3.1}$$

$$\therefore X_{PDLA} = X_{PDLA,0}\left[\frac{-I}{M_0}t + 1\right] \tag{3.2}$$

Where X_{PCL} and X_{PDLA} are the mass fractions of PCL and PDLA respectively. M_0 is the initial polymer solution volume inside the vial with mass fraction $X_{PDLA,0}$.

This gradient, however, takes account of the mass fraction of solvent that will evaporate after casting the film. The final mass fraction (or relative mass fraction) of PDLA in the dry coated film is given then by:

$$\phi_{PDLA} = \frac{X_{PDLA}}{X_{PDLA} + X_{PCL}} = \frac{X_{PDLA,0}\left[\frac{-I}{M_0}t + 1\right]}{X_{PDLA,0}\left[\frac{-I}{M_0}t + 1\right] + \left\{1 - \frac{X_{PDLA,0}\left[\frac{-I}{M_0}t + 1\right]}{X_{PDLA,0}}\right\} X_{PCL,0}} \tag{3.3}$$

$$\therefore \phi_{PDLA} = \frac{X_{PDLA,0}\left[\frac{-I}{M_0}t + 1\right]}{X_{PDLA,0}\left[\frac{-I}{M_0}t + 1\right] - X_{PCL,0}\left[\frac{-I}{M_0}t + 1\right] + X_{PCL,0}} \tag{3.4}$$

Where ϕ_{PCL} and ϕ_{PDLA} are the relative mass fractions of PCL and PDLA respectively. Equation 3.4 requires the initial mass fractions of PCL and PDLA to be identical in order to obtain a linear concentration gradient on the film. Thus $X_{PCL,0} = X_{PDLA,0} = X_0$, and:

$$\phi_{PDLA} = \left[\frac{-I}{M_0}t + 1\right] \tag{3.5}$$

Once the requirements for linear-composition-gradient libraries were defined, PDLA (Alkermes Medisorb 100DL high I.V. LACTIDE/GLYCOLIDE polymer, M_w=127000, M_w/M_n=1.56, lot No. 0103-442) and PCL (Aldrich Chemical Co., M_n=80000, M_w/M_n=1.425, lot No. 07526HI) were dissolved in chloroform (EM science, Merck KGaA

ACS grade), obtaining solutions with identical mass fraction X_0=0.05. The chloroform was previously "dried" by means of a molecular sieve (Type 3A, 8-12 mesh) and filtered with 0.45 μm filters to remove dust and small particles released by the molecular sieve.

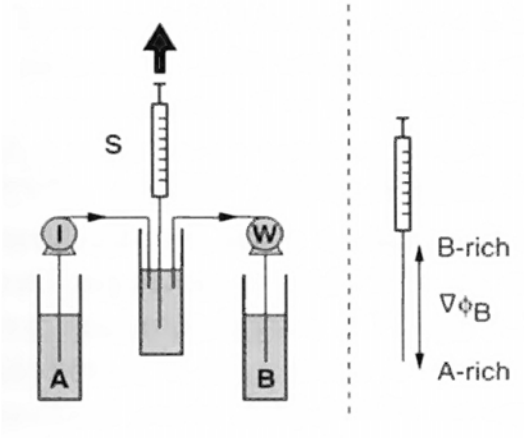

Figure 3.4. Schematic of the polymer gradient mixing procedure (A→PCL, B→PDLA) [14].

For the library preparation a 1.8ml glass vial was initially loaded with M_0=1ml of the 5% PDLA solution. As mixing began (t=*0*) the 5% PCL solution started being infused by an automated pump (kd scientific 210) at I=0.791 ml/min while, concurrently, another automated pump extracted solution from the vial at W=1.5 ml/min. A sample of V_S=84 μl was withdrawn with a small automated 1 ml syringe at a rate S=0.081 ml/min (total sampling time was t_S=62 s). A blunt point style needle gauge 18 (0.84 mm ID) and 6" long was used to prevent the sample going into the syringe avoiding mixing due to the change of diameter. Vigorous stirring inside the vial took place throughout the process ensuring homogeneous mixing. At the end of the mixing step a solution of PCL and PDLA remained inside the syringe needle with a linear composition gradient, ∇X_i, ranging from a PDLA-rich solution at the top (X_{PCL}=0, X_{PDLA}=0.05) to a PCL-rich solution at the bottom (X_{PCL}≈0.04, X_{PDLA}≈0.01) (figure 3.4).

Next, as soon as the mixing step was done, the gradient solution inside the needle was pumped out a rate of 5.6 μl/s, depositing a thin stripe along a 24 mm x 24 mm silicon <100> substrate (Silicon, Inc) (figure 3.5).

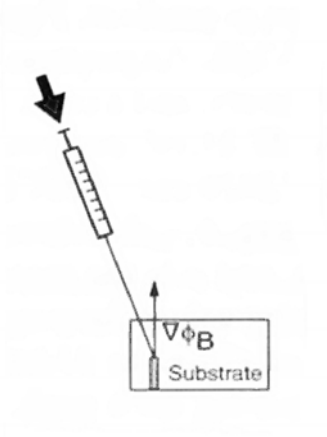

Figure 3.5. Illustration of the polymer-gradient deposition procedure [14].

The substrate with the composition-gradient stripe was swiftly placed below a stationary stainless steel blade previously positioned at an angle of 12° with respect of the substrate surface and 300 μm above it. A cross roller bearing table (Parker Daeldal) driven by a computer-controlled servomotor (Parker Compumotor) was used to move the substrate underneath the edge of the blade, at a velocity of 10.16 mm/s, in a direction orthogonal to the stripe painting direction (figure 3.6). As the substrate moved, the stripe was spread as a thin film of thickness 2 to 5 μm (after solvent dried).

An estimated linear PCL/PDLA gradient exists across the film, extending from a pure PDLA edge (ϕ_{PDLA}=1) to a PCL rich edge of ϕ_{PCL}≈0.82 and ϕ_{PDLA}≈0.18 [15] (any solvent residue was eliminated during the annealing process). Figure 3.7 illustrates the anticipated relative mass fraction profile of the film as a function of position over the library.

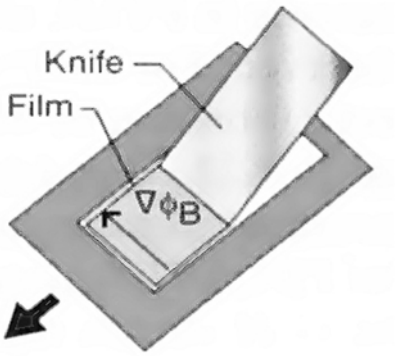

Figure 3.6. Representation of the film coating step [14].

The 24 mm x 24 mm silicon <100> squares (or “chips”) utilized as substrate were thoroughly cleaned, prior to the deposition step, in “piranha” solution (70% H_2SO_4/9% H_2O_2/21% H_2O) for 2 hours at 90 °C to allow complete wetting of the substrate surface. Following, the chips were etched in 6:1 Buffer Oxide Etch (HF/NHF_4, J.T. Baker) to generate a hydrophobic Si-H/Si surface that will aid in maintaining polymer adhesion to the chips for the duration of the cell culture experiments (section 4). After etched, the silicon chips were rinsed in DI water and blown with nitrogen.

To ascertain the appropriate etching time needed to avoid delaminating of the films from the silicon substrate, several chips with etching times of 1min to 8min were coated with polymer films, and submerged in aqueous solutions at 37 °C for at least 14 days to simulate cell culture conditions. After that, the chips were exposed to a series of different solutions that will be used during the bio assays, i.e. HCl 2N and surfactants like tritonX or TRIS. Etching times of 5min or more turned out to be enough to maintain the film attached to the silicon throughout the whole process.

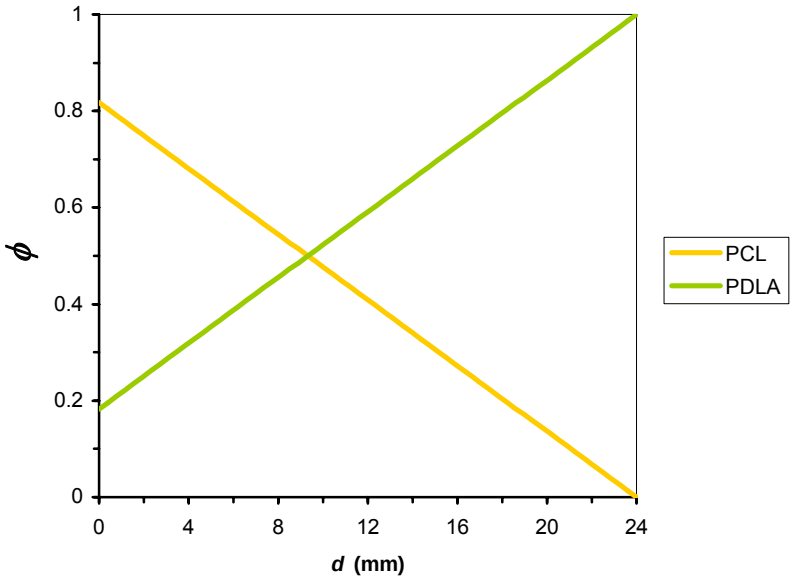

Figure 3.7. Relative mass fraction profiles of PCL and PDLA over the composition gradient library (Appendix A).

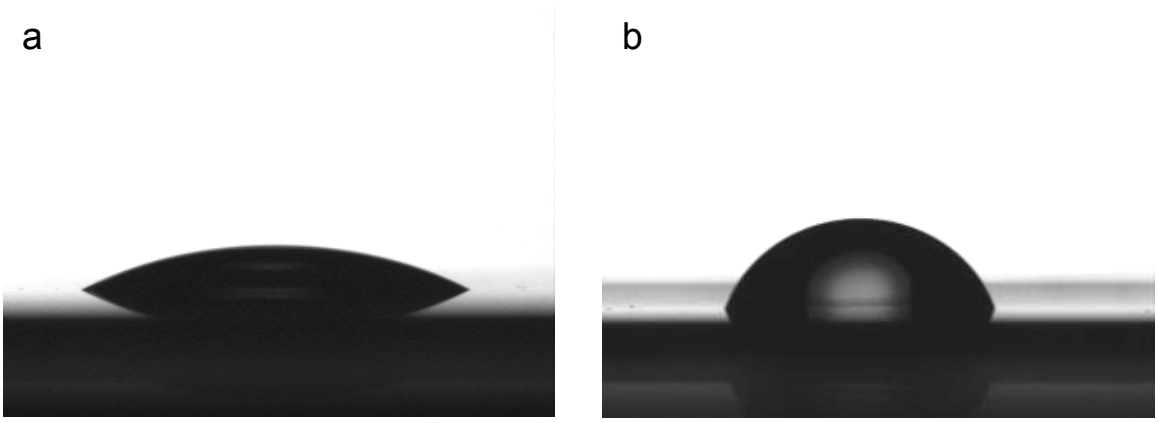

Figure 3.8. Static contact angles for a) piranha cleaned <100> silicon (24.38°±0.45°) and b) piranha cleaned + buffer oxide etched <100> silicon (69.24°±0.97°). Angles were measured using ImageJ image analysis software (NIH, public domain).

Static contact angle measurements to quantify the effect of the BOE etching process were performed with a goniometer (Rame-Hart 1000), obtaining 24.38°±0.45° for the piranha cleaned silicon and 69.24°±0.97° for the 5min piranha cleaned + BOE etched silicon (figure 3.8).

A photograph of an actual finished PCL/PDLA gradient library over a 24mmx24mm silicon substrate is shown in figure 3.9.

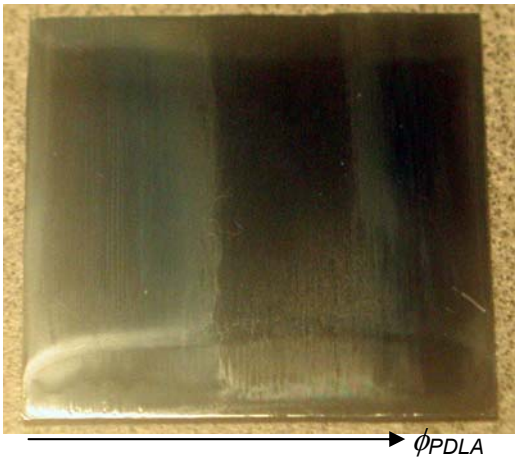

Figure 3.9. PCL/PDLA composition gradient library. Left side (hazy region): crystalline PCL rich regime. Right side (clear region): amorphous glassy PDLA regime. Transition occurs across the library as a result of the composition gradient.

3.2.2. TEMPERATURE GRADIENT LIBRARIES (ANNEALING)

As formerly stated, PCL/PDLA blends exhibit lower critical solution temperature (LCST) phase behavior [7]. As a result of this attribute thousands of dissimilar temperature-composition dependant interfacial properties can be found when inside the phase separated LCST boundary.

In order to explore a wide range of temperatures a temperature-gradient heating stage can be used to anneal and generate libraries with temperature distributions. Furthermore, composition gradients and temperature gradients can be overlapped to dramatically increase the number of distinct process conditions of a single sample (section 2.2.9.3).

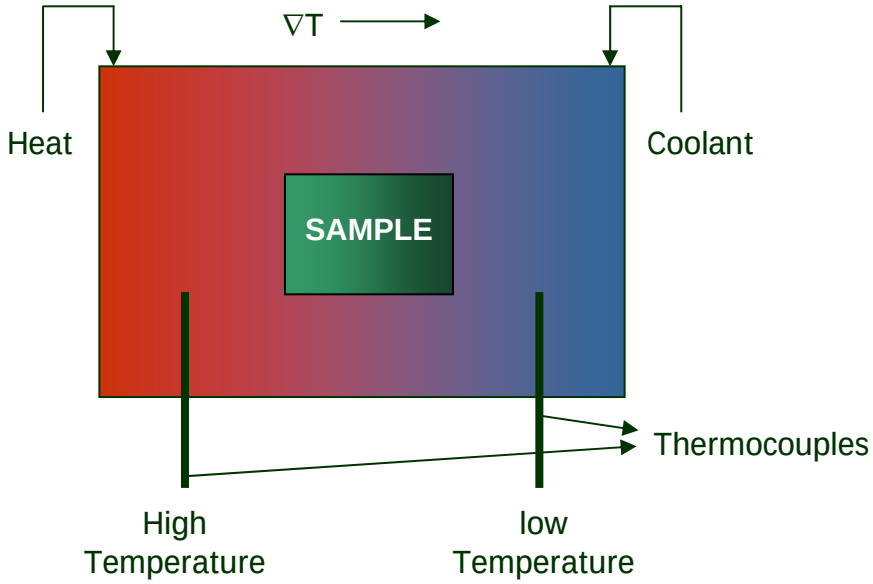

Figure 3.10. Schematic of a linear temperature-gradient heating stage.

Composition-gradient libraries were annealed for 2 hours over a custom rectangular aluminum heating stage with a linear temperature distribution [16] (assuming negligible heat loss along the edges). The adjustable temperature gradient was generated by a PID controlled heating element (chromalox CIR-1020 120V 150W) and a heat sink (water circulation from a controlled temperature water bath), placed at the end-points of the stage (figure 3.10).

The samples were carefully placed over the stage in a way that the composition gradient was orthogonal to the temperature gradient. The lower and upper temperatures of the stage were set to 140 °C and 58 °C respectively, creating a linear gradient of approximately 1.81 °C/mm along the stage. To minimize convective heat transfer and oxidation a small vacuum chamber was created on top of the heat stage with a viton® o-ring and a glass plate. Air was evacuated from the chamber though a small orifice at the bottom stage connected to a vacuum pump.

Once the annealing process was terminated the libraries were rapidly quenched to room temperature. The finished libraries have orthogonal composition and temperature gradients (figure 3.11) ranging from 0.18 < ϕ_{PDLA} < 1 and 76.3 °C < T < 120 °C respectively.

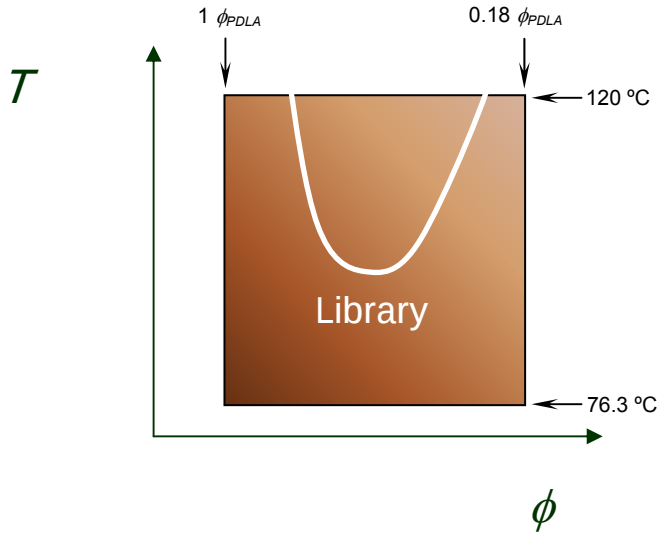

Figure 3.11. Illustration of a finished combinatorial library with coupled temperature and composition orthogonal gradients. The white line represents the LCST regime boundary, where phase separation takes place.

Numerous surface temperature measurements were made over the stage to validate the linear assumption in the temperature gradient. As anticipated, the temperature profile showed a linear fashion with variations extending from ±0.2 to ±0.8 °C for points placed along constant temperature lines (figure 3.12). The temperatures along the edges were in average 0.3 °C less than the temperature “inside” the stage, corroborating the edges small heat loss assumption.

It’s important to note that the temperature measurements were done without vacuum. Consequently, the expected temperature profile inside the vacuum chamber, during annealing, can be slightly different with respect to the measured values shown in figure 3.12.

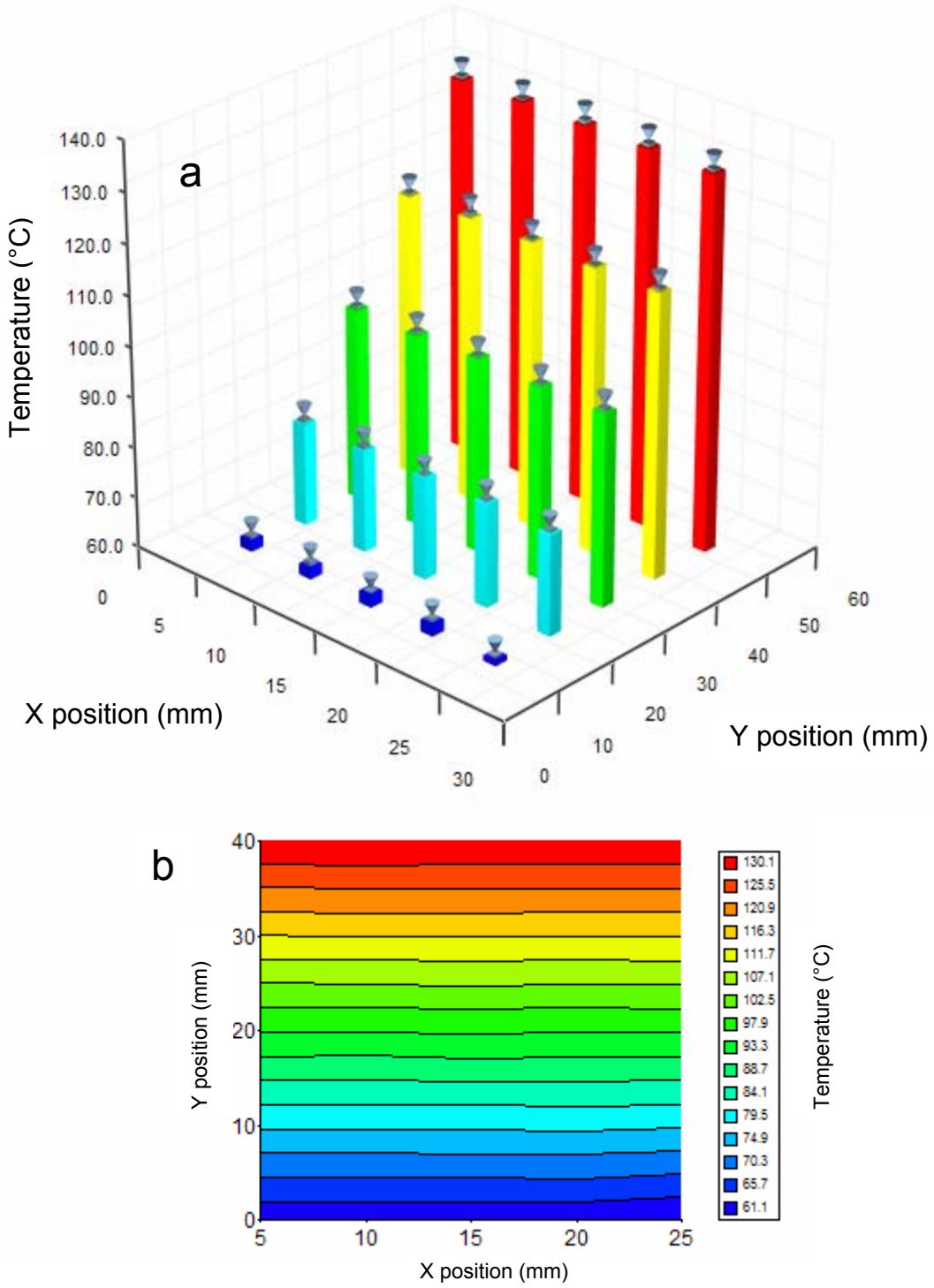

Figure 3.12. Heating stage surface temperature measurements. a) Temperature as a function of position (values are presented as mean ± SEM, n=9. Error bars are delimited with inverted cone markers). b) Temperature contour map showing "constant temperature lines" (constant Y).

3.2.3. CHARACTERIZATION OF TEMPERATURE/COMPOSITION LIBRARIES

As we know, the diverse surface morphology and microstructure created by the phase separation of the PCL/PDLA leads to a whole new set of physicomechanical properties that need to be characterized. However, for the purpose of this work we needed to focus only on the characterization of the different topographies along the library surface. Characterization of mechanical properties, for example modulus and strain-at-failure, are beyond the scope of this study and can be found elsewhere in the literature [12, 17].

3.2.3.1. ELLIPSOMETRY

The thickness of the combinatorial libraries was determined from measurements done with a wide spectral range V-VASE® variable angle spectroscopic ellipsometer (J.A. Woollam Co.) Relative phase, Δ, and amplitude, Ψ, changes on incident polarized light, induced by the reflection from the library thin film, were directly measured with the ellipsometer across a wavelength range of $200<\lambda<1700$ nm. Optical constants and film thickness were obtained using the software package WVASE32 (J.A. Woollam Co.), executing a point-to-point data fitting on the transparent Cauchy region ($700<\lambda<1100$ nm). The wavelength range corresponding to the Cauchy region (extinction coefficient k=0) for PCL/PDLA blends was previously established using an UV/visible spectrophotometer (Hewlett Packard). The fitting procedure was done using the refractive index of pure PCL and PDLA as “best guesses”, since neither the optical properties nor the thickness of the PCL/PDLA blend were known. Several iterations were

done to confirm that the minimum “best fit” determined by the Marquardt-Levenberg algorithm (used in WVASE32) was the sought value instead of a local minimum.

3.2.3.2. FOURIER TRANSFORM INFRARED SPECTROSCOPY (FTIR)

FTIR absorption spectra of the PCL/PDLA blends were registered with a Bruker IRscope II using a KBr beam splitter at room temperature. The sample area was purged with nitrogen to avoid appearance of water bands in the spectra. Zinc selenide (ZnSe), instead of silicon <100>, was used as the substrate of the composition-gradient libraries since it is more suitable for FTIR analysis as it is transparent down to approximately ν=600 cm^{-1}.

Spectra were measured and averaged 128 times at a resolution of 4 cm^{-1} for several locations of distinct composition over the library. Positioning of the sample was done by an automated moving stage with ±1μm accuracy. Bands in the CH_3 asymmetric/symmetric stretch region (ν=2970–2950/2880–2860 cm^{-1}) and the CH_2 asymmetric/symmetric stretch region (ν=2935–2915/2865–2845 cm^{-1}) were resolved using peak separation and analysis software (Peakfit®, Systat Soft.). Deconvolution and fitting was done using Peakfit®’s Gaussian amplitude IRF deconvolution procedure to obtain the area of the IR absorption peaks in the aforementioned regions. Ratios of these areas were used to determine the approximate composition of different spots over the library.

3.2.3.3. ATOMIC FORCE MICROSCOPY (AFM)

Surface topography characterization was performed using a Thermomicroscopes® Explorer scanning probe microscope (SPM), with a gold-coated silicon nitride V-shaped cantilever (part# MLCT-EXMT-A, Veeco metrology group). Data was acquired in contact mode and force modulation mode over a sampling area of 100 μm x 100 μm at a scanning rate of 200 μm/s. The force modulation or z-modulation is basically a secondary imaging mode derived from the standard contact mode, which measures relative elasticity/stiffness of surface features, facilitating the mapping of material distribution in composite systems and improving the detection of minute surface characteristics. Force Modulation imaging allows simultaneous acquisition of both topographic and material-properties maps.

Surface structure of different spots of the PCL/PDLA libraries were visualized from the z-modulation maps (force modulation mode), while average microdomain height and root-mean-square roughness, which is defined as the standard deviation of the surface height measurements over a scanned area, were determined from the topography maps (standard contact mode). The measurements were effectuated over a vibration isolating air table so as to minimize noise from the surroundings.

3.2.3.4. CROSS POLARIZED OPTICAL MICROSCOPY

Surface structure visualization was done via an automated Olympus BX51 cross polarized microscope. Cross polarization filters were operated at an angle of 45° (high extinction factor) to achieve high contrast between the glassy amorphous PDLA phase and the crystalline PCL phase. Pictures taken with a digital camera (Olympus C-3040) coupled to the microscope were processed and analyzed with ImageJ (NIH, public

domain) and SigmaScan Pro (Systat software), in order to identify and characterize parameters of the phase separated regions of the PCL/PDLA blends, such as: diameter of the phase separated structures and surface fraction of each component.

3.3. RESULTS AND DISCUSSION

3.3.1. LIBRARY FILM THICKNESS (ELLIPSOMETRY)

Ellipsometry was carried out *before* annealing the libraries, since it diminish the surface uniformity required to obtain the best possible model fitting (low mean squared error –MSE–), due to the dramatic increase of surface roughness generated by the blend phase separation. However, thickness is not expected to change appreciably due to polymer flow or diffusion during the 2 hour annealing process [16].

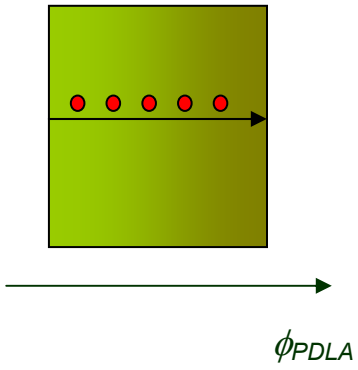

Figure 3.13. Graphic representation of the ellipsometry test locations (red dots) over the composition gradient library.

Measurements were performed at 5 different locations aligned orthogonally to the composition gradient, covering the whole composition range (figure 3.13). These

measurements were made over 3 different libraries and repeated three times (at 3 different locations) for each single library.

The results from the ellipsometry quantifications are condensed in a plot of thickness vs. chip position (figure 3.14).

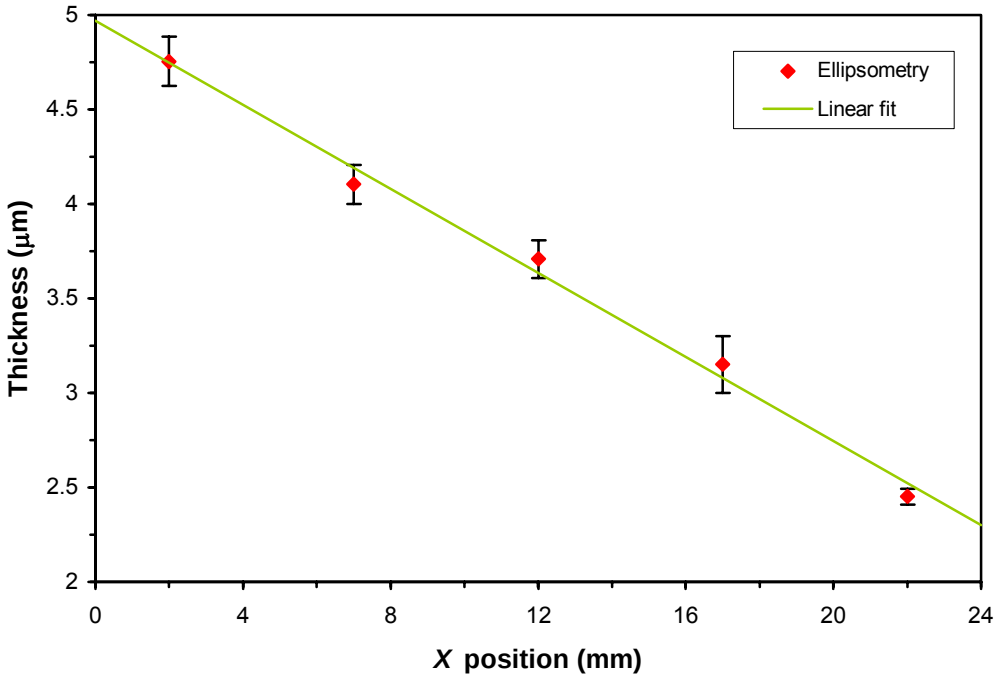

Figure 3.14. Thickness measurements by ellipsometry for PCL/PDLA composition gradient libraries (red dots). The straight line corresponds to a linear fit of the ellipsometry data (R^2=0.993). *X*=0 mm and *X*=24 mm correspond to ϕ_{PCL}≈0.82 and ϕ_{PCL}≈0 respectively. Each data point represents the average thickness of 3 measurements over 3 different libraries. Error bars denote the standard uncertainty (±SEM, n=9).

It is readily seen that the film thickness varies monotonically along the library width from approximately 4.95 μm on the PCL rich side to 2.23 μm on the PDLA rich one. A variation of this kind was expected, given the difference in viscosity between the PCL and PDLA solutions ($\mu_{PCL} > > \mu_{PDLA}$) and the linear composition profile across the library (FTIR, section 3.3.2).

The thickness of the libraries was deliberately high to avoid shifting of the LCST boundary to temperatures different than those of the bulk LCST [13, 18], and to prevent dewetting during the annealing step. Initial trials with very thin libraries cast over etched and non-etched silicon, and with thicker libraries prepared over “relative hydrophilic” silicon (etching times of 1min or less, including non-etched silicon), showed dewetting structures when annealed; suggesting that low film thicknesses and high surface energy substrates facilitate thermally induced dewetting.

3.3.2. LIBRARY COMPOSITION (FTIR)

FTIR spectra of several locations across the PCL/PDLA libraries were acquired along a line orthogonal to the composition gradient, following a similar fashion to that depicted in figure 3.13 for the ellipsometry procedure.

Spectra measured over numerous positions of non-annealed and annealed PCL/PDLA libraries are shown in figure 3.16 (only the CH_2 and CH_3 symmetric and asymmetric stretch regime is shown since peaks of interest are found in this wavenumber interval)

Characteristic peaks of the FTIR spectra, based on the structure of each component (figure 3.15), were chosen to follow the change of PCL and PDLA concentrations along the library.

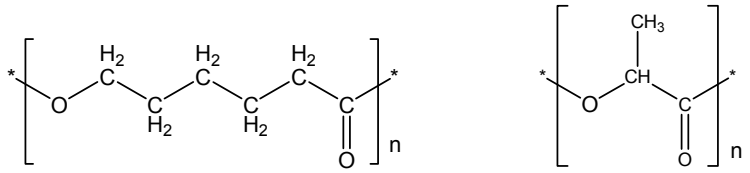

Figure 3.15. Chemical structures of PCL and PDLA.

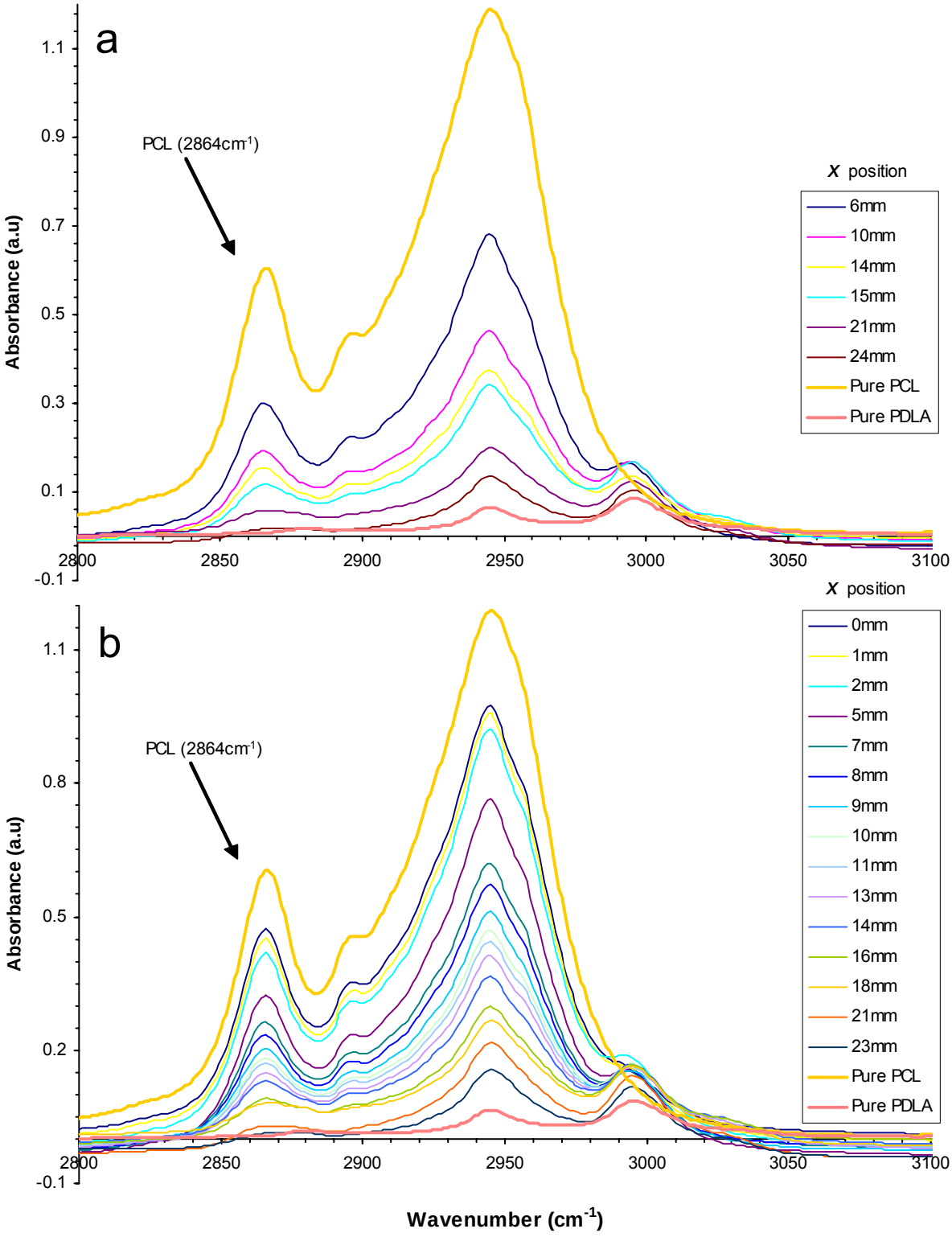

Figure 3.16. FTIR spectra of PCL/PDLA composition-gradient films: a) annealed library, b) non-annealed library. Each curve represents a different spot over the library (inset). ($\Delta\phi_{PCL}$≈0.82 to 0).

A long 5-carbon CH_2 chain in the PCL structure and a methyl (CH_3) side group in the PDLA one, are the most prominent differences among the structures of the 2 polymers. Consequently a characteristic peak was expected for PCL in the CH_2 stretch region, whereas a PDLA signature was anticipated in the CH_3 region. Indeed, PCL showed a remarkably strong absorbance peak around 2864 cm^{-1}, CH_2 symmetric stretch regime ("pure PCL" curve, figure 3.16). In contrast, PDLA showed a characteristic, but faint, peak close to 2970 cm^{-1}, asymmetric CH_3 stretch region ("pure PDLA" curve, figure 3.16). The reason of the dim absorbance of PDLA in the CH_3 stretch regime (when compared to that of PCL in the CH_2 regime) can be due in part to the film thickness difference between the PDLA and PCL rich regions (almost 2 times thinner in the PDLA-rich end).

Following the peak at 2864 cm^{-1}, a monotonic decrease in PCL absorbance is witnessed as position is scanned across the library (starting from the PCL-rich edge). A corresponding increase in PDLA absorbance (2970 cm^{-1} peak) is also noticed.

Absorbance variation of the peak centered at 2864 cm^{-1} was assumed to be exclusively an effect of PCL concentration change (which can be seen from the FTIR spectra of pure PCL and pure PDLA in figure 3.16). Therefore, quantitative analysis to verify composition along the library, and to validate the linear composition gradient profile estimated from the mass balance (equation 3.5), was effectuated comparing the absorbance of this peak (2864 cm^{-1}) with the absorbance of mixtures of known concentration and thickness (standards). The model to obtain the PCL mass fraction was based on the Beer-Lambert law, defined as follows:

$$\frac{I}{I_0} = \exp\left(-\varepsilon C h\right) \tag{3.6}$$

Where I and I_0 are the intensity of the transmitted and incident radiation respectively, ε is the frequency dependant extinction coefficient, C is the sample concentration, and h is the sample thickness. Absorbance, A, is defined as the negative logarithm of the transmittance ratio, therefore:

$$A = \varepsilon C h \tag{3.7}$$

Since the extinction coefficient, ε, is only a function of frequency, it is constant for particular material at a fixed frequency. Thus, mixtures of known composition and thickness can be employed to determine the concentration of unknown mixtures at a preset frequency:

$$\frac{A_1}{A_0} = \frac{\varepsilon C_1 h_1}{\varepsilon C_0 h_0} \tag{3.8}$$

$$\therefore C_1 = \frac{A_1 C_0 h_0}{A_0 h_1} \tag{3.9}$$

Where 0 and 1 subscripts represent the known and unknown mixtures respectively.

The thickness of the unknown sample, h1, was approximated from the thickness profile obtained earlier by ellipsometry (figure 3.14). A "2nd derivative zero" algorithm (Peakfit®) that determines the points where the second derivative of the data is both constant and zero, was used for baseline subtraction prior to absorbance (peak area) calculation. Absorbance values of the peak at 2864 cm^{-1} for different PCL compositions were calculated for 2 separate non-annealed libraries using Peakfit®. Four different standards of 25%, 50%, 75% and 100% PCL were prepared and characterized by FTIR absorbance at 2864 cm^{-1} and thickness (ellipsometry). An average variation of 1.8% was observed between the calculated PCL concentration values for a particular spot,

depending on the standard used. The average of the values estimated with all 4 standards was taken as the final PCL concentration.

Figure 3.17 shows the calculated PCL concentration values along with the predicted profile from mass balance. As seen in the plot, there is good agreement between the mass balance and the values obtained from FTIR spectra. Differences between them extend from 0.2% to 4.8%, with an average of 2.24%. Theses results validate the existence of a *linear* composition profile along the composition-gradient library, and show the potential of the gradient-film coating technique as a powerful methodology for preparing custom combinatorial samples.

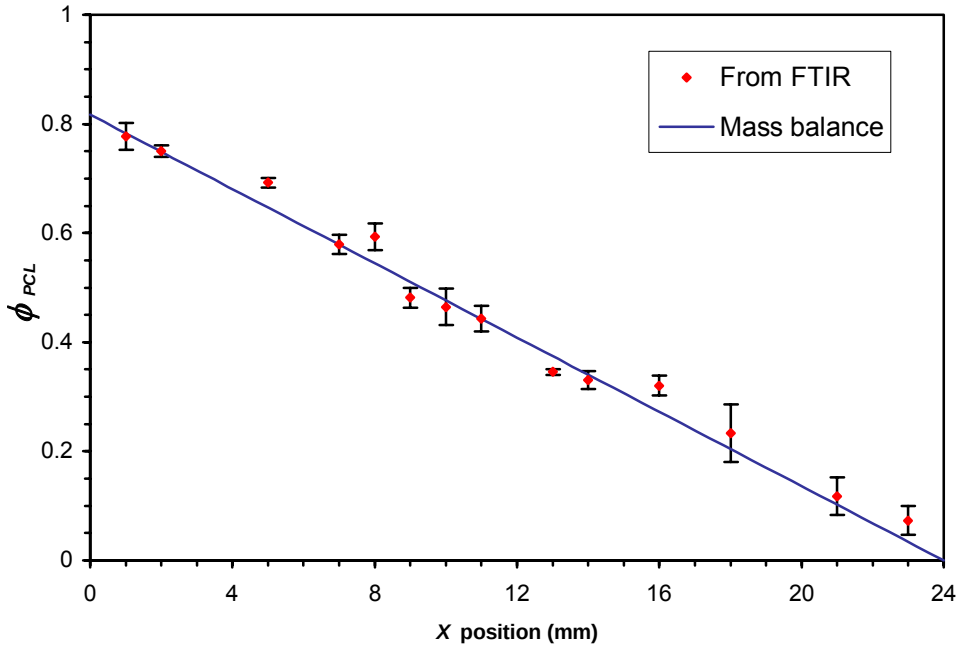

Figure 3.17. PCL mass fraction vs. position over a *non-annealed* linear-gradient PCL/PDLA library. The solid blue line represents the expected mass fraction of PCL (mass balance). Red dots represent the average value of the PCL concentration calculated at the same location in 2 separate libraries. Standard uncertainty given by error bars (±SEM, n=2).

In order to verify that the linear composition profile was not affected by the annealing process, the same 2 chips formerly used for the mass balance validation of non-annealed libraries were annealed for 2 hours following the procedure outlined in section 3.2.2. FTIR spectra of the annealed chips (figure 3.16a) were registered along a line of constant annealing temperature (approximately 100 °C). Just a few random positions were evaluated since the purpose was not to show that the gradient *was* linear, but that it *remained* linear once the library was annealed.

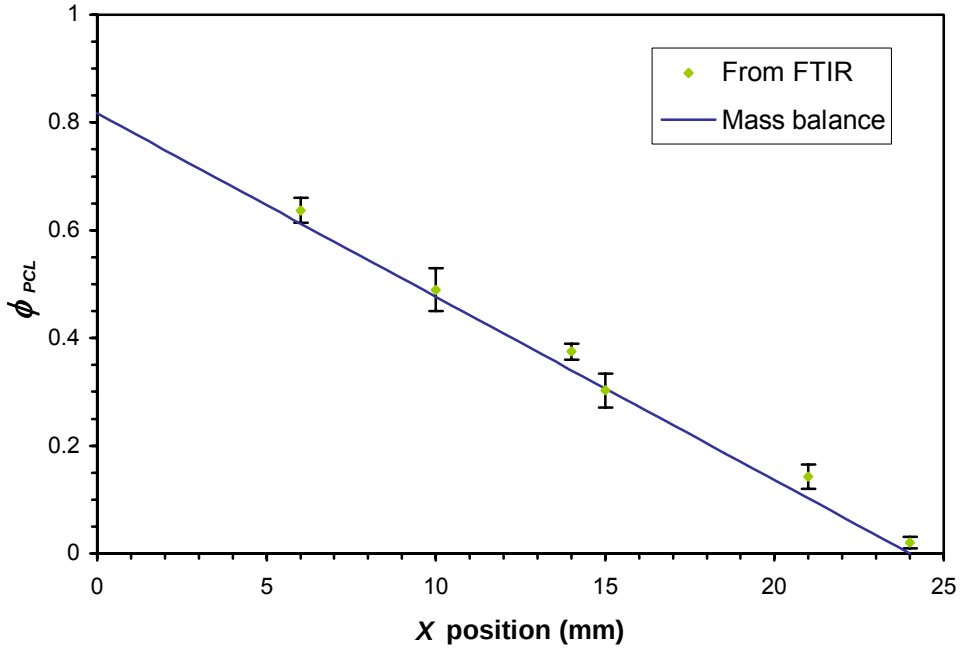

Figure 3.18. PCL mass fraction vs. position over an *annealed* linear-gradient PCL/PDLA library. The solid blue line represents the expected mass fraction of PCL (mass balance). Green dots represent the average value of the PCL concentration calculated at the same location in 2 separate libraries. Standard uncertainty given by error bars (±SEM, n=2).

Diffusion for a 2 hour anneal was not likely to affect considerably the previously observed linear profile, as based on a diffusion length ($\sqrt{Dt}$) of approximately 849nm (equivalent to 0.0035% of the library width) for a polymer of M_W≈115000 with an average

diffusion coefficient of $D \approx 10^{-16}$ m^2/s in a polymer melt. Figure 3.18 illustrates that the influence of the annealing procedure on the composition gradient was indeed negligible, as all the points calculated deviate only from 0.4% to 3.5%, with an average of 2.28%, from the theoretical values.

3.3.3. LIBRARY SURFACE ROUGHNESS (AFM)

Atomic force microscopy (AFM), used to physically characterize the surface profile of the libraries, was executed in two different scanning modes, namely, contact mode and z-modulation (or force modulation) mode. In force modulation imaging mode, the cantilever tip tracks the sample topography as in normal contact mode, with the difference that a periodic signal is applied to the cantilever. The amplitude of tip modulation that results from this applied signal varies according to the elastic properties of the sample. Hence, the resulting force modulation image, which is a map of the sample's elastic response, shows improved contrast between surface features when compared to its topography counterpart (as seen in figures 3.21). Both types of images were collected simultaneously, since the frequency of the signal applied to the tip is several times higher than the Z feedback loop it is set up to track. Therefore, topographic information can be separated from local variations in the sample's elastic properties.

AFM scans were performed over three separate libraries at several locations of disparate composition-temperature regimes, covering an area of 100 μm x 100 μm per scan. Values of the root-mean-square roughness, which gives information about the height difference distribution of the surface microstructures, were estimated from the AFM topography maps obtained for each regime (figure 3.19). As pointed out in section

3.2.3.3, the root-mean-square roughness corresponds to standard deviation of the height of the different surface features over the scanned area.

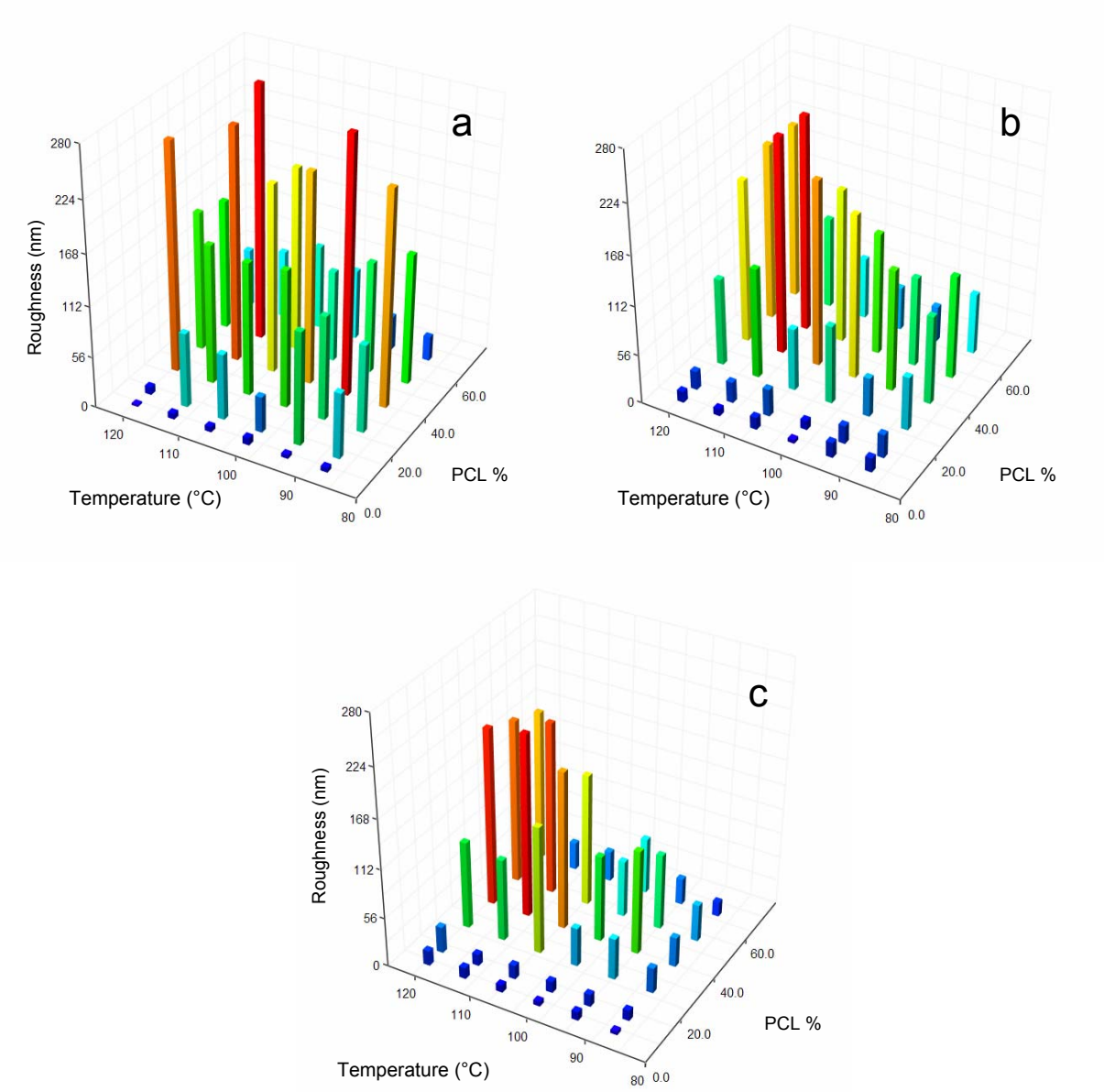

Figure 3.19. Root-mean-square surface roughness of three separate annealed composition-gradient libraries, obtained from topography maps of contact AFM mode. a), b) and c) denote libraries 1, 2 and 3 respectively.

It is very important to note that AFM tests were completed only over *annealed* libraries, since the main purpose of the procedure was to analyze and characterize the

surface topography of the different microstructures developed during phase separation of the PCL/PDLA blends (LCST phase behavior). Figure 3.19 shows a general trend of surface roughness increment as temperature increases. This trend is more clear on libraries 2 and 3 (figures 3.19b and 3.19c) than in library 1 (figure 3.19a), which shows particularly high roughness values at low temperatures (around 87 °C), masking the global effect of temperature on roughness. These high values are likely to be an artifact related to inconsistencies in the library preparation, since those temperatures correspond to the lower limit of the LCST regime, where such large changes on surface topography are not expected. The effect of composition on surface roughness is somehow different than that of temperature, as roughness increases with PCL concentration until a maximum is reached in the vicinity of 55% PCL, close to the LCST limits (as seen in figure 3.3). Further increase in PCL concentration evidences a decrease in surface roughness, as seen at 66% PCL, which is clear in all the 3 libraries. The average surface roughness profile of PCL/PDLA libraries as a function of composition and temperature is shown in figure 3.20a.

In order to ease the visualization of the roughness distribution over an annealed library, a contour map of the average roughness values presented in figure 3.20 is shown in figure 3.20b. It is evident that the LCST phase behavior of the polymer blend has a significant effect on surface roughness, as there is a noticeable increase in surface roughness deep inside the LCST regime and further gradual decrease towards its limits. This suggests the development of very distinct PCL and PDLA microdomains due to both PCL crystallization and phase separation, and also confirms the transition of a segregated structure to a continuous 1-phase morphology as the LCST boundary is reached.

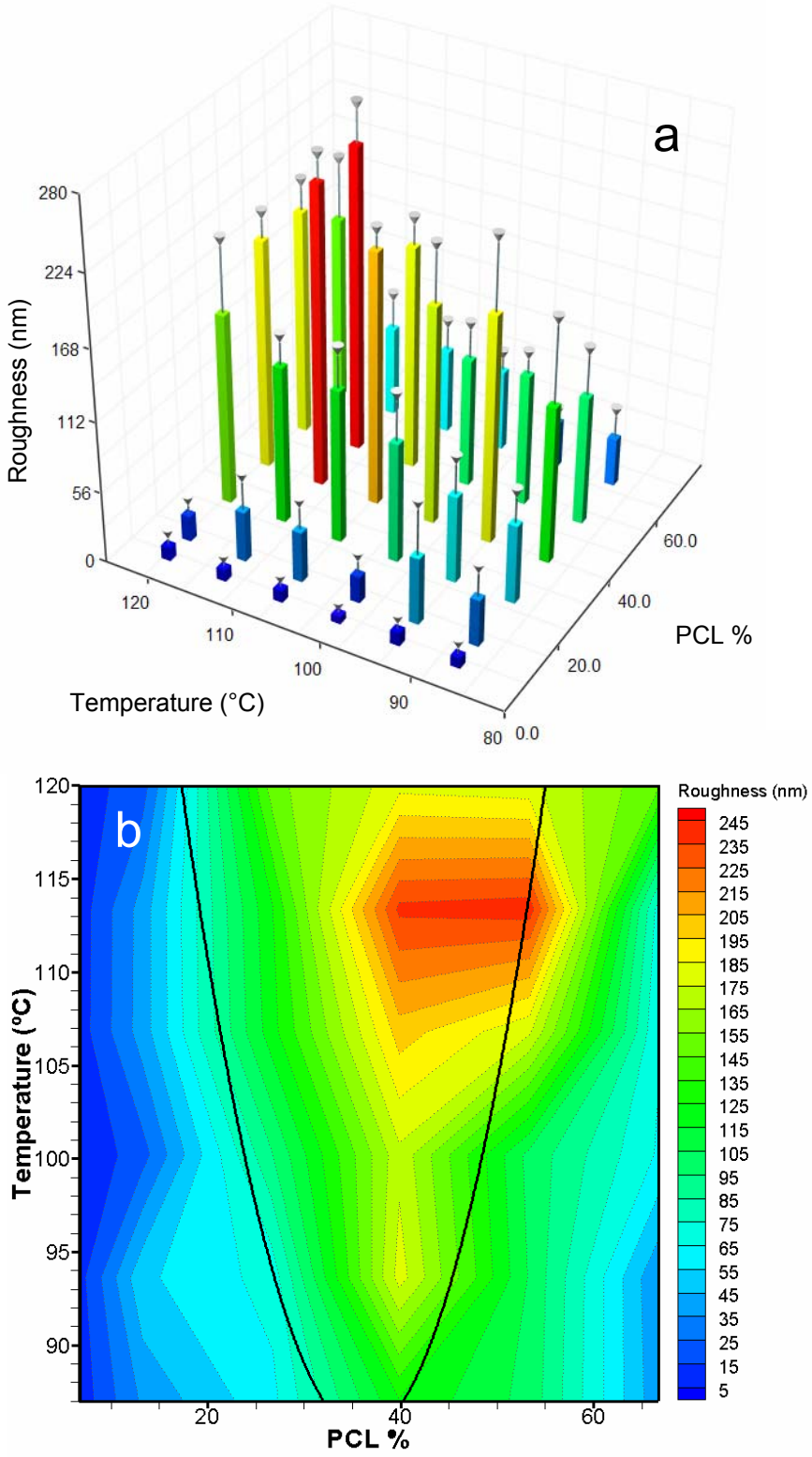

Figure 3.20. a) Root-mean-square surface roughness profile of a PCL/PDLA annealed composition-gradient library. Values presented as averages ± SEM (indicated by error bars delimited by inverted cone markers, n=3). b) Contour map of the average root-mean-square surface roughness values over the composition-gradient library.

Topography and force modulation maps of diverse composition-temperature regimes of PCL/PDLA libraries are shown in figures 3.21 through 3.25. These images allow direct visualization of an extensive variety of surface microstructures, and facilitate comprehension of the surface roughness values presented beforehand. Three dimensional extensions of the topography maps are also shown in order to enhance visualization, illustrating the actual polymer surface morphology.

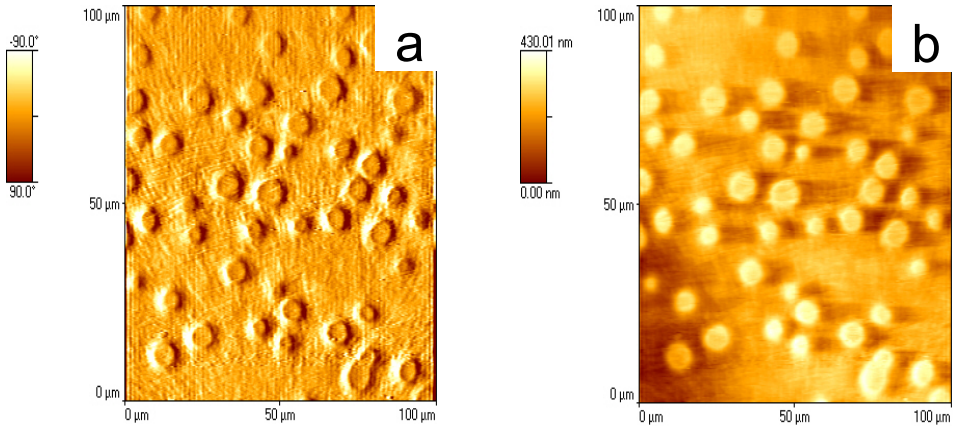

Figure 3.21. AFM images of a two-hour annealed PCL/PDLA library. Approximate composition and temperature of the scanned area are 26%PCL/74%PDLA and 120 °C respectively. a) Force modulation mode map. b) Contact mode topography map. Scanned area: 100 µm x 100 µm.

The contrast between figures 3.21 and 3.22 illustrates the gradual change of surface microdomains configuration as concentration is scanned along a line of constant temperature. Thereby, the regime corresponding to 26% PCL and 120 °C (figure 3.21) exhibits a discrete small-droplet phase identified as the PCL-rich domain (section 3.3.4), which is dispersed in a continuous PDLA-rich matrix.

As PCL concentration rises to 39% PCL at 120 °C (figures 3.22a and 3.22b), the size of the semicrystalline discrete PCL-rich domains augments as well as their height. Further increase in PCL concentration to 53% PCL at 120 °C (figures 3.22c and 3.22d),

evinces a consolidation of the PCL-rich regimes which gives place to a bi-continuous phase morphology of the PCL/PDLA blend (section 3.3.4). Higher PCL concentrations, above approximately 58% PCL, present an opposite behavior to that seen in low PCL concentration areas; namely, a continuous rich-PCL phase with dispersed PDLA droplets.

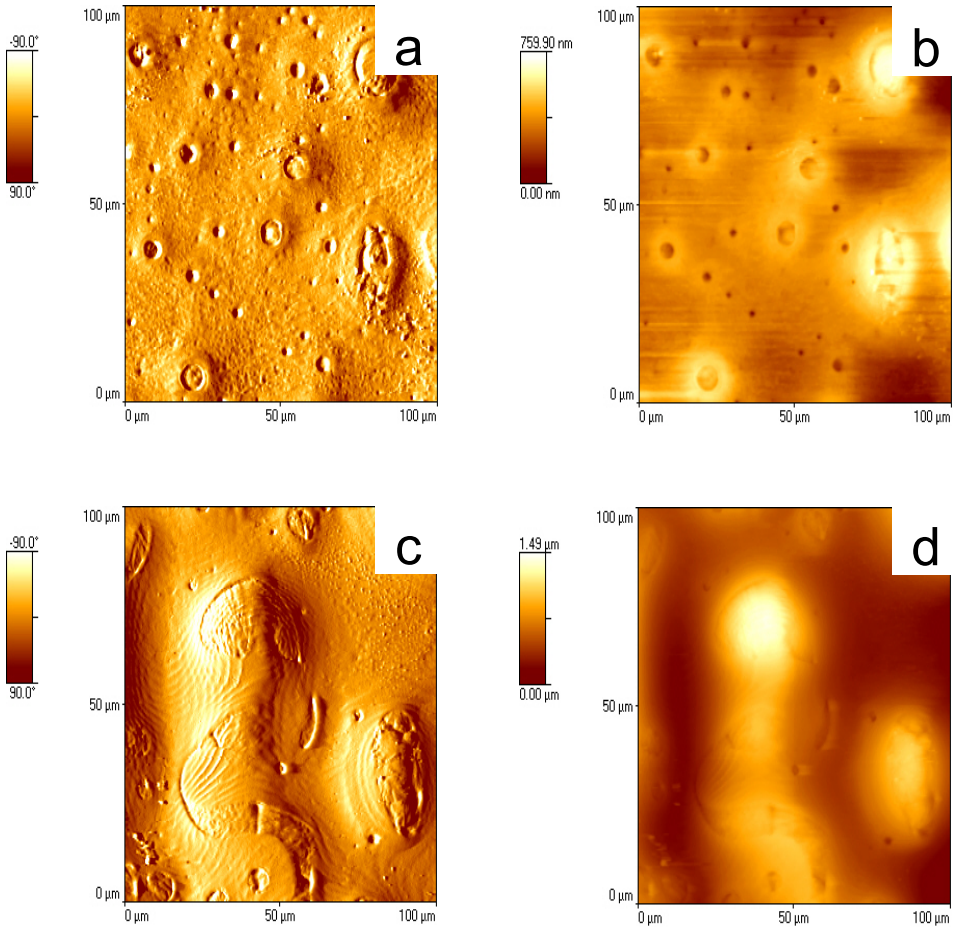

Figure 3.22. AFM images of a two-hour annealed PCL/PDLA library. Images a) and c) correspond to force modulation maps, and images b) and d) to contact mode topography maps. Approximate compositions of the scanned areas are 39%PCL/61%PDLA for images a) and b), and 53%PCL/47%PDLA for images c) and d). Temperature is 120 °C for all images. Scanned area: 100 µm x 100 µm.

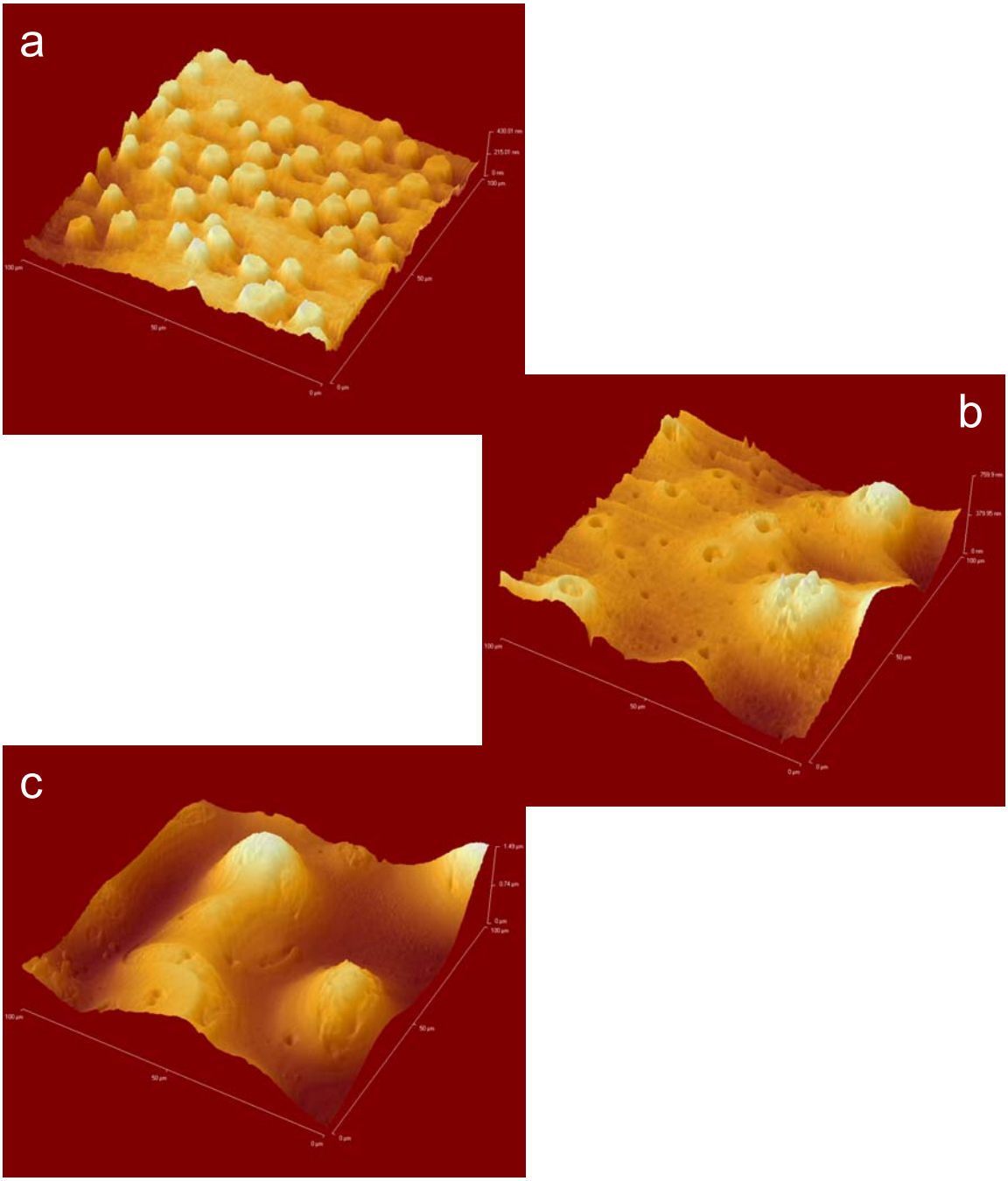

Figure 3.23. Three dimensional extensions of AFM topography maps of two-hour annealed PCL/PDLA libraries. a) 26%PCL/74%PDLA, PCL-rich droplet-like domains dispersed in a continuous PDLA-rich matrix. b) 39%PCL/61%PDLA, PCL-rich domains in a continuous PDLA-rich matrix. c) 53%PCL/47%PDLA, merged PCL-rich domains forming a bi-continuous PCL/PDLA matrix. The approximate annealing temperature of the sampled regions is 120 °C. Scanned area: 100 μm x 100 μm.

In order to witness the variety of surface morphologies across PCL/PDLA libraries, areas with different conditions of temperature and composition than those previously presented were scanned as well. A few of these are shown in figures 3.24 and 3.25.

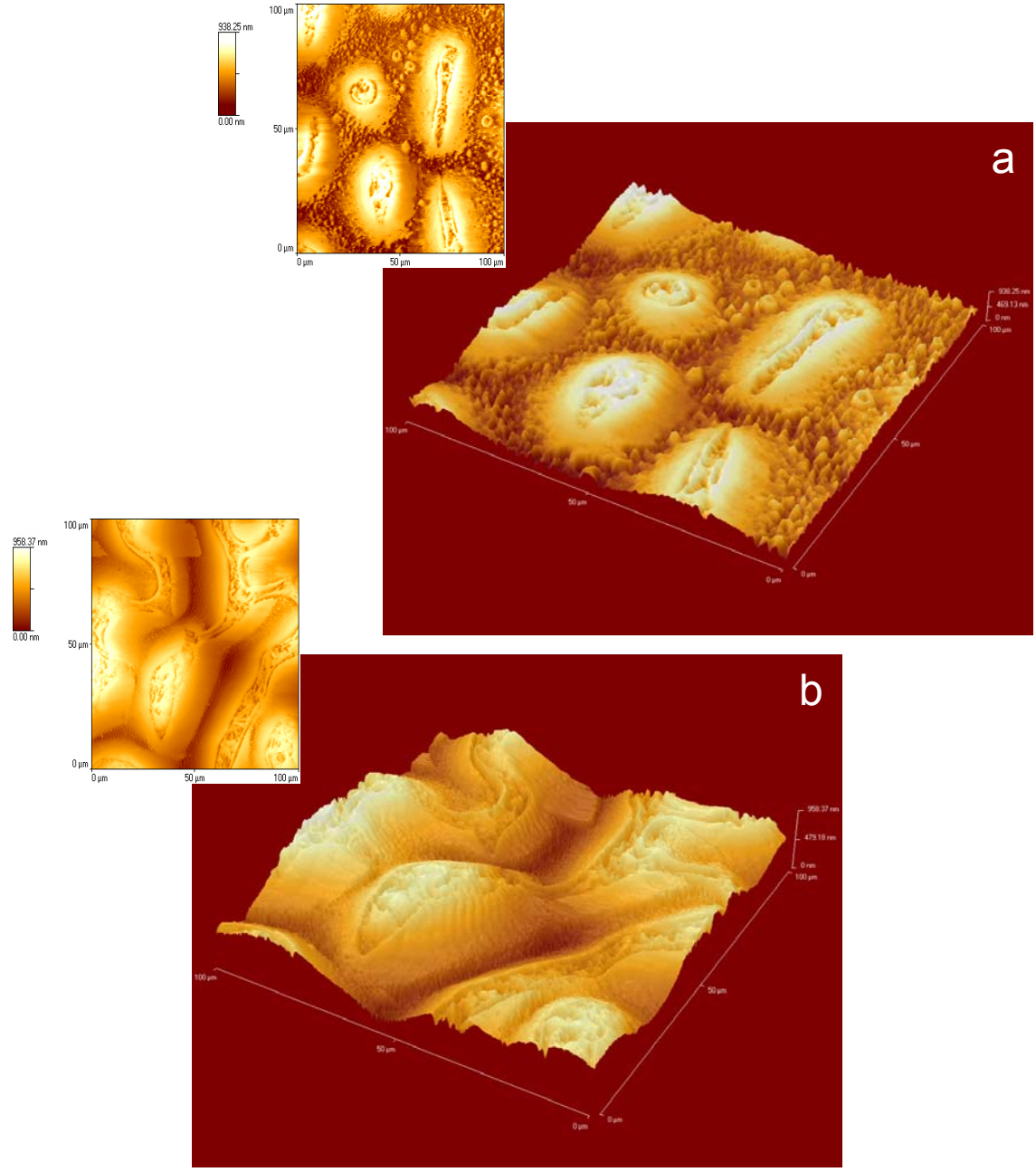

Figure 3.24. 2D and 3D topography maps of two-hour annealed PCL/PDLA libraries. a) 32%PCL/68%PDLA 110 °C, PCL-rich domains segregated in a PDLA-rich surrounding. b) 40%PCL/60%PDLA 100 °C, bi-continuous PCL/PDLA structure. Scanned area: 100 μm x 100 μm.

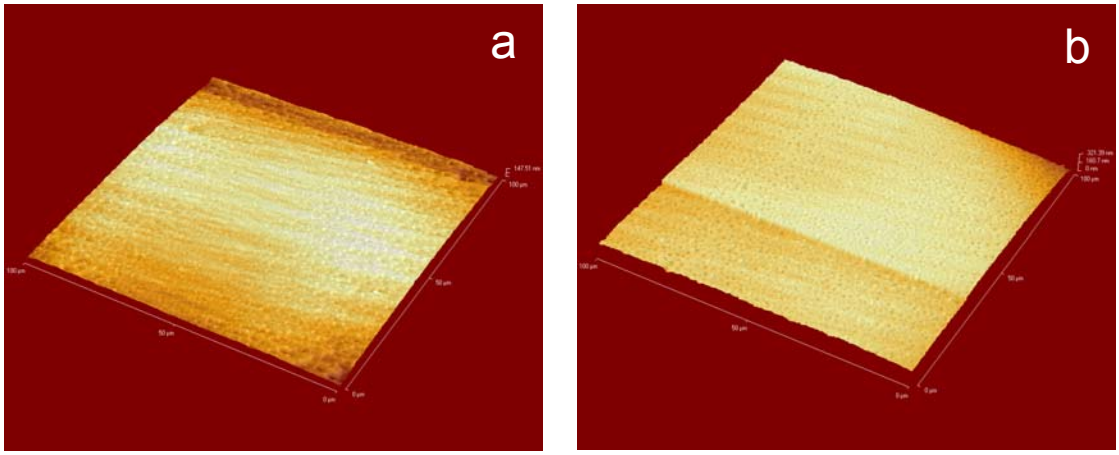

Figure 3.25. Three dimensional topography maps of two-hour annealed PCL/PDLA libraries. a) 70%PCL/30%PDLA 100 °C. b) 10%PCL/90%PDLA 95 °C. Scanned area: 100 μm x 100 μm.

The three dimensional topography maps shown in figures 3.25a and 3.25b present a lack of segregation of chemically distinct domains, leading to more homogeneous and smoother (less rough) surfaces. This is consistent with the expected characteristics of a completely miscible blend, as the scanned areas correspond to locations well outside the LCST regime, where PCL and PDLA are totally miscible and form a continuous one-phase blend.

3.3.4. MICRODOMAIN GEOMETRY AND DISTRIBUTION CHARACTERIZATION (CROSS POLARIZED OPTICAL IMAGING)

Further surface characterization by means of AFM was hindered by the limited scanning range of the apparatus when compared to the size of some surface microstructures. Cross polarized optical microscopy was therefore used to accomplish this task, taking advantage of the fact that the crystalline morphology of PCL rotates polarized light, whereas the amorphous PDLA structure doesn't. This is translated in a

high contrast between bright PCL crystalline and semicrystalline regions and dark PDLA areas, as clearly seen in figure 3.26.

Characteristics of the phase separated polymeric blend, such as structure diameter and individual component surface coverage, were obtained by means of image analysis. The detailed analysis procedure followed is depicted in the subsequent paragraphs. However, it is shown for only one image as the analysis method is the same for each of the 144 images evaluated. Image manipulations (enhancements) such as correction of lightning unevenness and contrast increase were effectuated prior to the analysis to improve its reliability.

Pictures were taken over annealed libraries at the same 36 composition-temperature locations examined with AFM, in order to observe how surface roughness correlates with microstructure size and polymer surface fraction.

3.3.4.1. IMAGE ENHANCEMENT

Image enhancement was performed using the image analysis software package SigmaScan Pro (Systat software).

The first step followed in the enhancement procedure was correcting uneven lighting, as it greatly influences intensity thresholding (a major problem in image analysis). Lightning correction, also called shading correction, was done creating an 8 x 8 grid pseudo-clearfield map of the original image, which is an approximation of the image's lightning pattern or true clearfield map.

Figure 3.26. Original polarized microscope picture of a phase separated PCL/PDLA blend. Bright and dark regions correspond to crystalline PCL and amorphous PDLA respectively. Encircled area shows uneven image lighting.

The pseudo-clearfield map was generated by setting the center point of each square of the predefined 8 x 8 grid, to the value of the lightest pixel in the original image's corresponding square. Linear interpolation between the adjusted center points was then used to estimate the intensity values of the rest of the pseudo-clearfield map (figure 3.27a). It is important to mention that prior to the pseudo-clearfield generation, the original image was converted to grayscale in order to allow grayscale linear interpolation between the grid center points.

Image equalization (lightning correction) was performed dividing the original image by the generated pseudo-clearfield map.

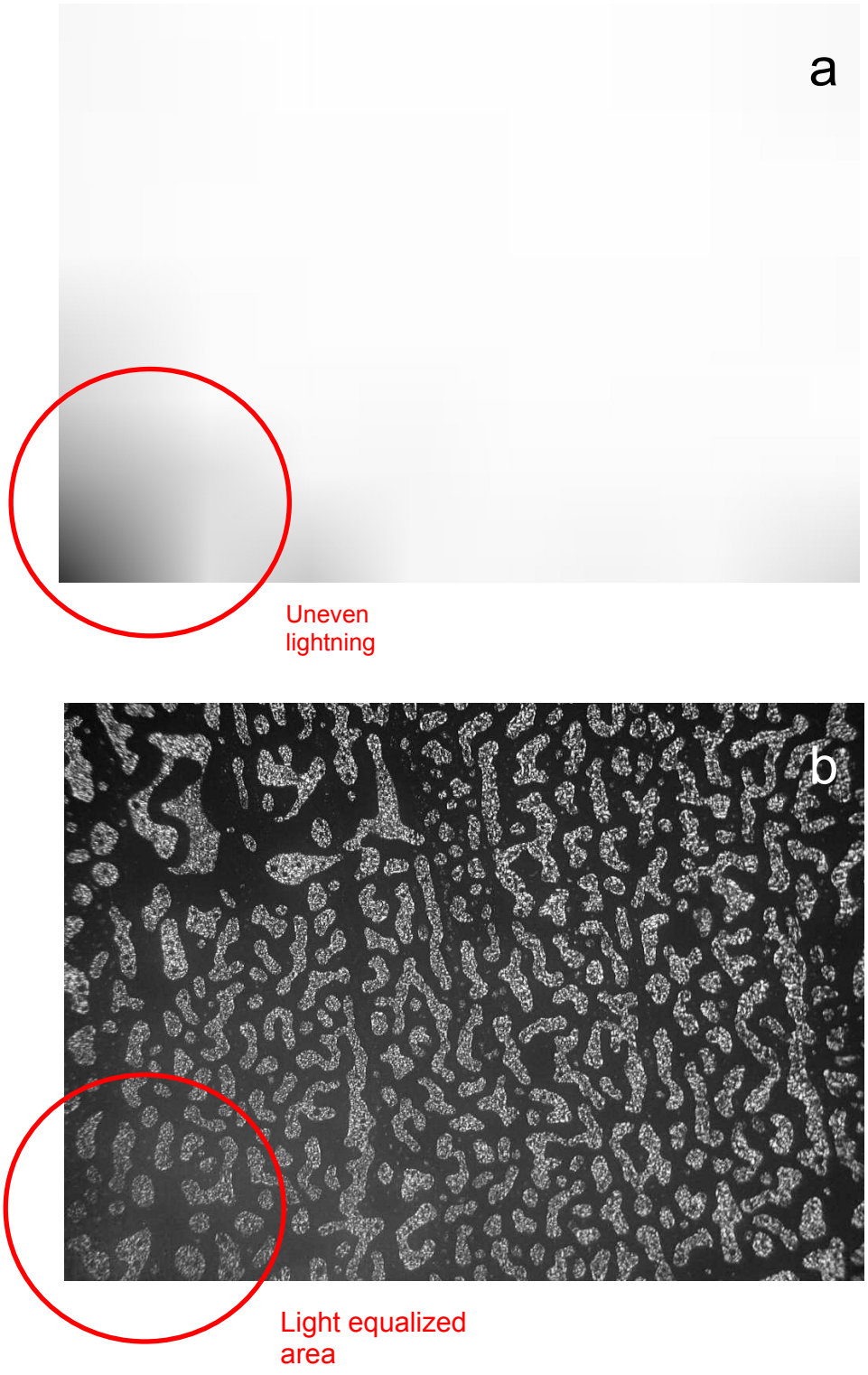

Figure 3.27. a) Generated approximation of the lighting pattern of the image shown in figure 3.26 (pseudo-clearfield map). Encircled area shows uneven image lighting. b) Light equalized and contrast enhanced image (grayscale). Encircled area highlights the light equalized region.

Further enhancement of the image was performed by increasing the contrast of the light equalized image, in order to facilitate intensity thresholding and therefore image overlay plane generation. The final enhanced image to be used for analysis is shown in figure 3.27b.

3.3.4.2. IMAGE ANALYSIS

The procedure followed to analyze different regions of the PCL/PDLA libraries was divided in two parts namely; overlay plane generation and filtering, which involves the creation of a binary image suitable for analysis; and binary image particle analysis, employed to characterize microstructure size and surface fraction of each component. Overlay plane generation and manipulation was performed using SigmaScan Pro (Systat software), and final particle analysis was carried out with ImageJ (NIH, public domain).

The main idea behind creating an overlay plane of an image prior to its analysis, is simply to generate an image segmentation that groups the parts of interest leaving outside those that lack importance.

Overlay planes were obtained defining an intensity threshold (equation 3.10) over a histogram of the pixel intensities distribution of the previously enhanced grayscale image.

$$f_\tau(x,y) = \begin{cases} 1 \ \textit{if} \ \ f(x,y) \geq \tau \\ 0 \ \textit{if} \ \ f(x,y) < \tau \end{cases} \tag{3.10}$$

Where *f(x,y)* is the grey value of a pixel located at the position (*x,*y), and τ is a *fixed* grey value defined as “threshold”.

Pixels with grey intensities above the threshold value τ are assigned to category 1 and are declared as “object”; those with intensities below τ are assigned to category 0 and declared as “background”.

The threshold value was chosen so that only PCL-rich regions (object), which corresponds to high intensity pixels (bright areas), were included in the overlay plane; leaving out the low intensity pixels corresponding to PDLA-rich domains (background). When the pixels range or categories were set, the grey level of each pixel in the image was compared with the selected threshold level. Pixels with intensities laying in category 1 and category 0 are turned “on” and “off” respectively, generating the desired binary overlay plane (figure 3.28).

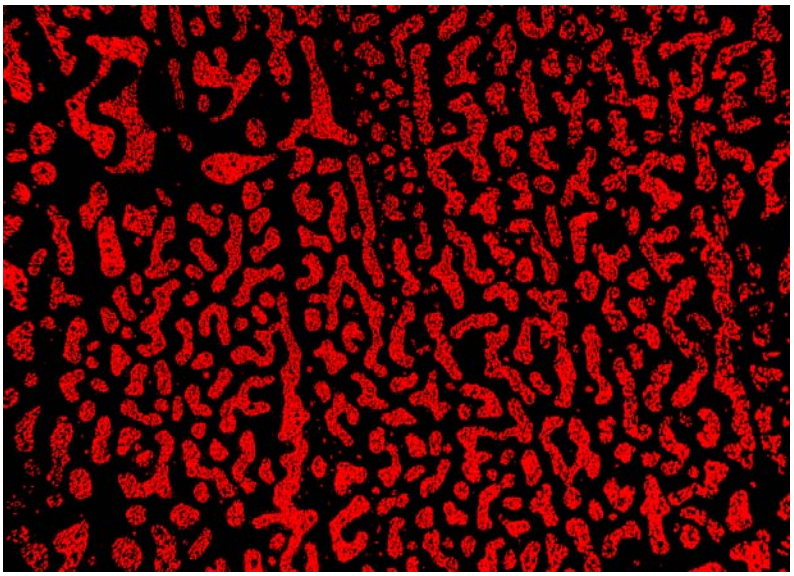

Figure 3.28. Overlay plane of the PCL/PDLA library region shown in figure 3.27b. Red pixels correspond to category 1 (PCL-rich) and black pixels to category 0 (PDLA-rich).

It is readily seen in figure 3.28 that the generated overlay plane matches very well the PCL-rich rich domains. However, these regions, seen as red “blobs” in the figure, are not completely formed by PCL and the presence of minute PDLA domains is

evident (minuscule black dots inside the red blobs). This creates a problem for the final image analysis, since the existence of these small domains makes the particle analysis extremely sensitive to the lower limit value setting of the particle size. In other words, a small bright PCL area surrounded by these tiny PDLA domains, which is indeed part of a bigger PCL domain, can be counted as one independent particle; resulting in considerable variations on the calculated average domain size. For example, increasing the lower particle size from 1 pixel to 4 pixels on a 1024 x 768 pixels image (as the one showed in figure 3.28) increases the average PCL domain size approximately 4 to 7 times.

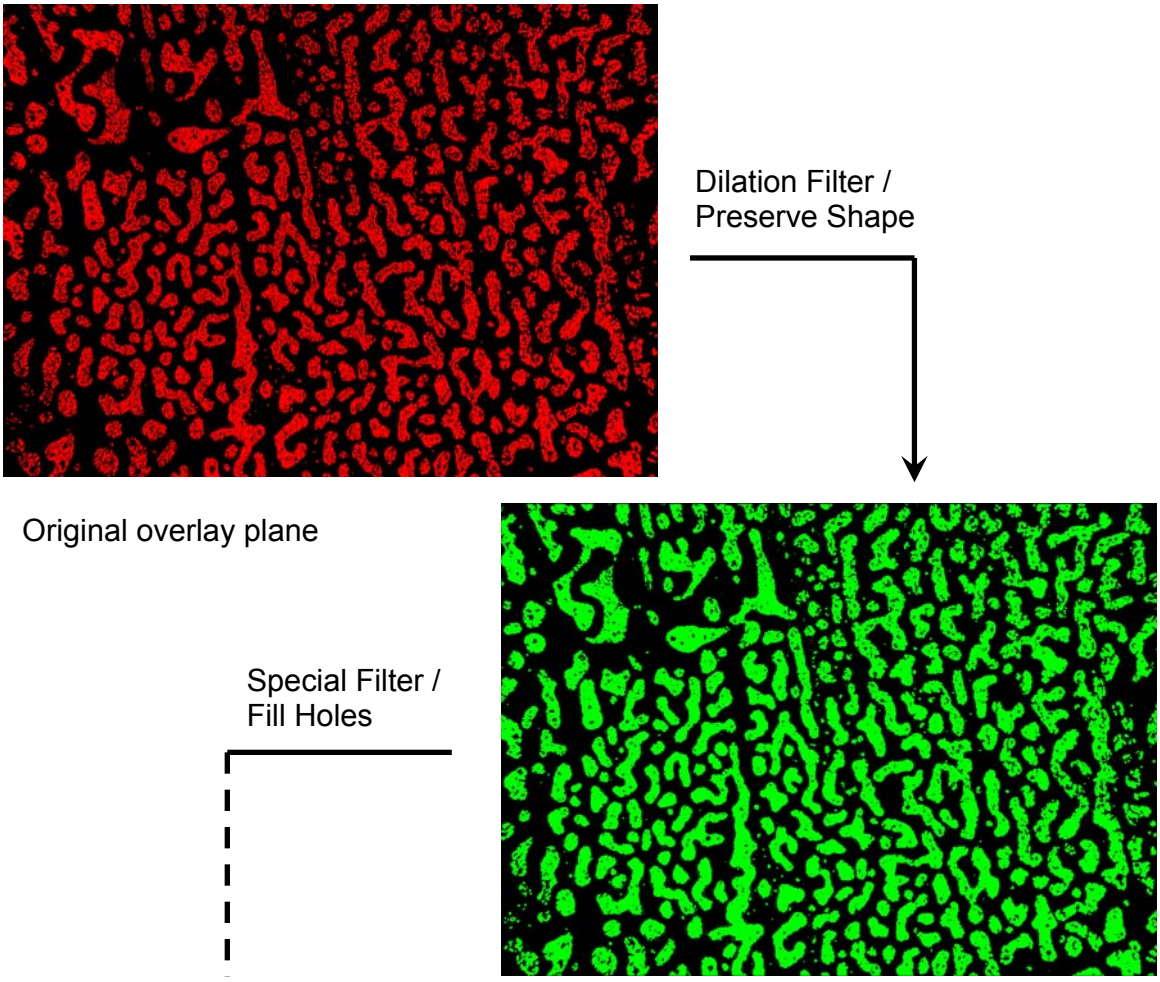

Figure 3.29. Filtering procedure of the original overlay plane to remove small PDLA domains from PCL rich regions.

(Figure 3.29 continued)

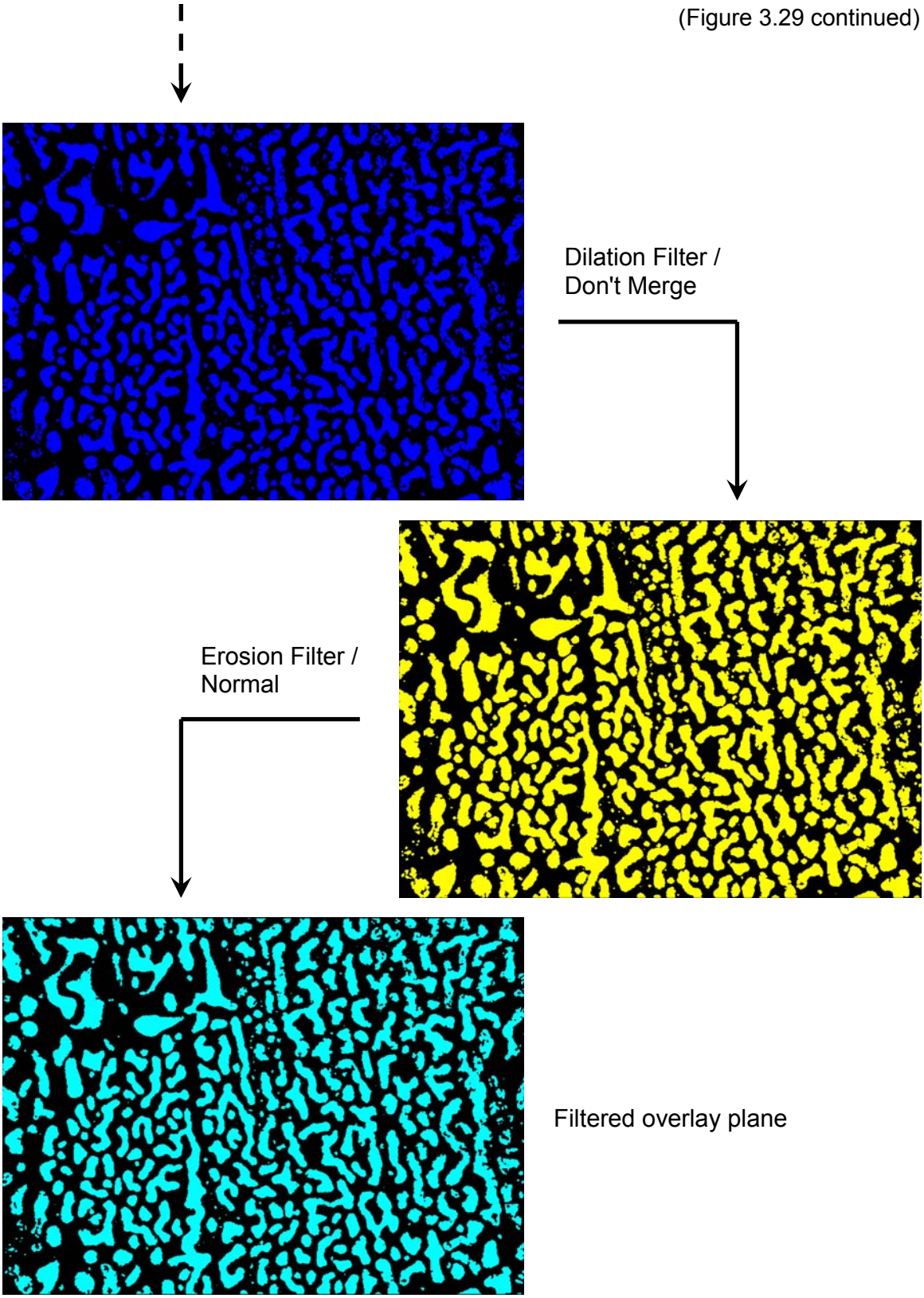

Figure 3.29. Filtering procedure of the original overlay plane to remove small PDLA domains from PCL rich regions.

To avoid this problem the initial overlay plane was filtered using several standard filtering techniques such as dilation, erosion, and “hole filling” (detailed explanation of morphology filters for binary images can be found elsewhere [19]). The filtering procedure executed is outlined in figure 3.29.

It is important to notice that the use of a standard global thresholding technique was satisfactory, due to the fact that the contrast between PCL and PDLA in the polarized microscopy images was considerably high. Otherwise, the use of more specialized techniques like sharpening filters (i.e., Sobel filter and Roberts filter) [20], and adaptive thresholding would have been required to improve edge detection.

Image analysis of the final filtered overlay plane (figure 3.29) was performed using ImageJ’s built-in particle analysis routine. This routine counts and measures objects in binary or thresholded images by scanning the image or selection until it finds the edge of an object. It then outlines the object (figure 3.30) and measures it using the “measure” command; another built-in function of the program [21]. This command allows effectuating several distinct measurements (i.e., particle size, area, circularity, diameter, etc); however, we focused on only two of them, namely, particle maximal Feret’s diameter (F_{max}) and particle area coverage.

Maximal Feret’s diameter is defined as the theoretical diameter of an object if it were circular in shape, which is equivalent to the particle’s caliper length or longest distance between any two points along the selection boundary (particle boundary). This parameter is widely used to characterize the dimensionality of objects with random shapes or “blob” shapes (figure 3.31), such as the phase separated microstructures found over PCL/PDLA libraries. Edge particles (those intersected by the border or “frame” of the image) were excluded from the analysis when calculating the particles average size and maximal Feret’s diameter, to avoid inaccurate values that could have emerged when taking into account incomplete particles. These incomplete particles,

however, were considered to calculate the polymers average surface fraction as the whole image area is used to determine this value.

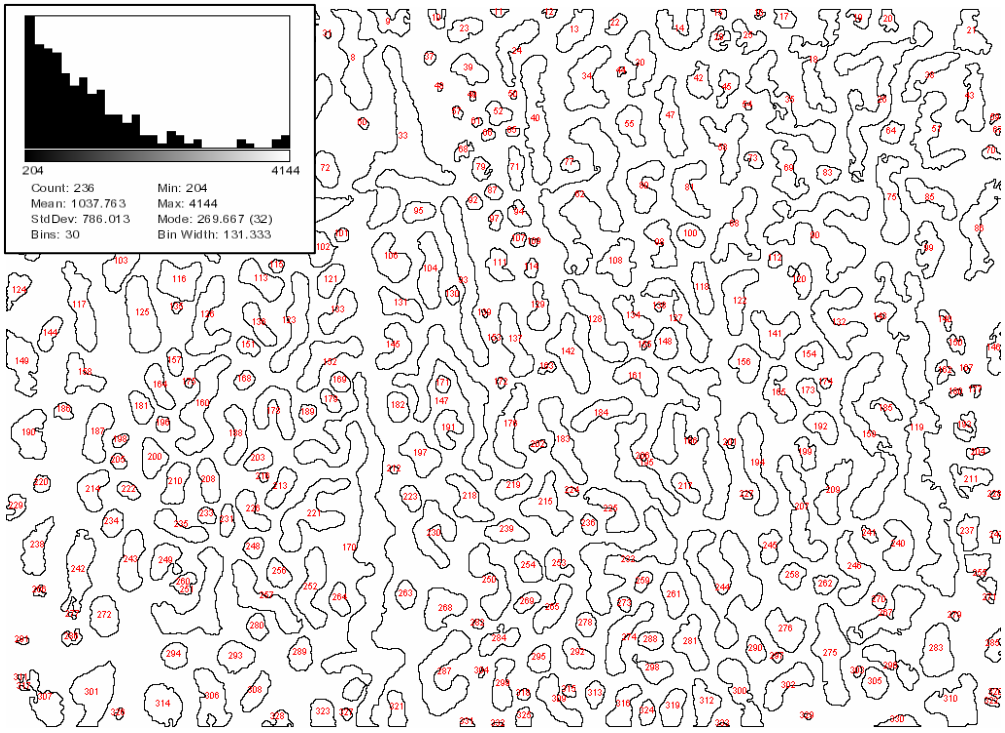

Figure 3.30. Outlines of the measured regions generated during the image analysis procedure. Inset: particle size distribution.

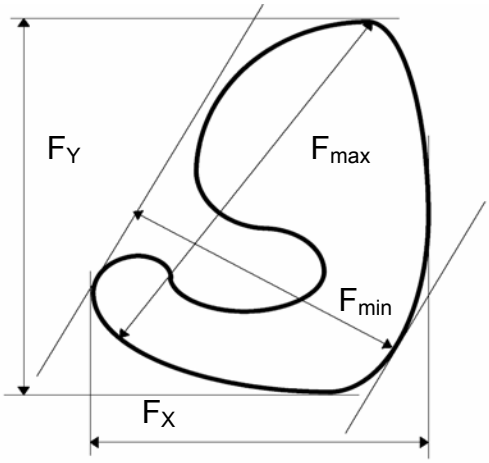

Figure 3.31. Schematic of the maximal (F_{max}) and minimal (F_{min}) Feret's diameters of a random shape particle [20].

The surface fraction covered by PCL-rich domains exhibits a monotonic rise as PCL concentration increases (figure 3.32). This increment is quite clear above a PCL

mass percentage of approximately 15%. Below this value the calculated surface coverage of PCL ranged between 0% and 3% regardless of the PCL concentration, which might be explained by hindering of PCL crystallization due to a high degree of dispersion of PCL in the glassy PDLA matrix at very low PCL concentrations. Limitations in the resolution of the image analysis technique can also contribute to this fact, as there is a lower limit of PCL concentration below which bright pixels of minute crystalline regions cannot be resolved. Temperature, on the other hand, seemed to have little or no effect on the percentage of area covered by PCL regimes, as there is no marked change or trend in this quantity along lines of varying temperature and constant composition (figure 3.32a, lateral view).

It can be noticed in the range of monotonic increase of surface coverage with increasing PCL concentration, that the surface percentage values are approximately an additional 10% higher than the corresponding PCL concentration values; that is, for a PCL concentration of 40% the surface coverage is close to 50%, for a concentration of 50% the area is about 60% and so on. This difference is due mainly to the filtering procedures applied to the images prior to their analysis, specially the “hole filling” filter, since small PDLA regions are masked and considered to be part of bigger PCL structures incrementing therefore the effective area covered by PCL. The approximation of the three-dimensional morphology of the libraries surface, generated by the height disparity between PCL-rich and PDLA-rich domains, to two-dimensional images, also contribute to this difference, since the images fail to account for the real amount of PCL present in each domain.

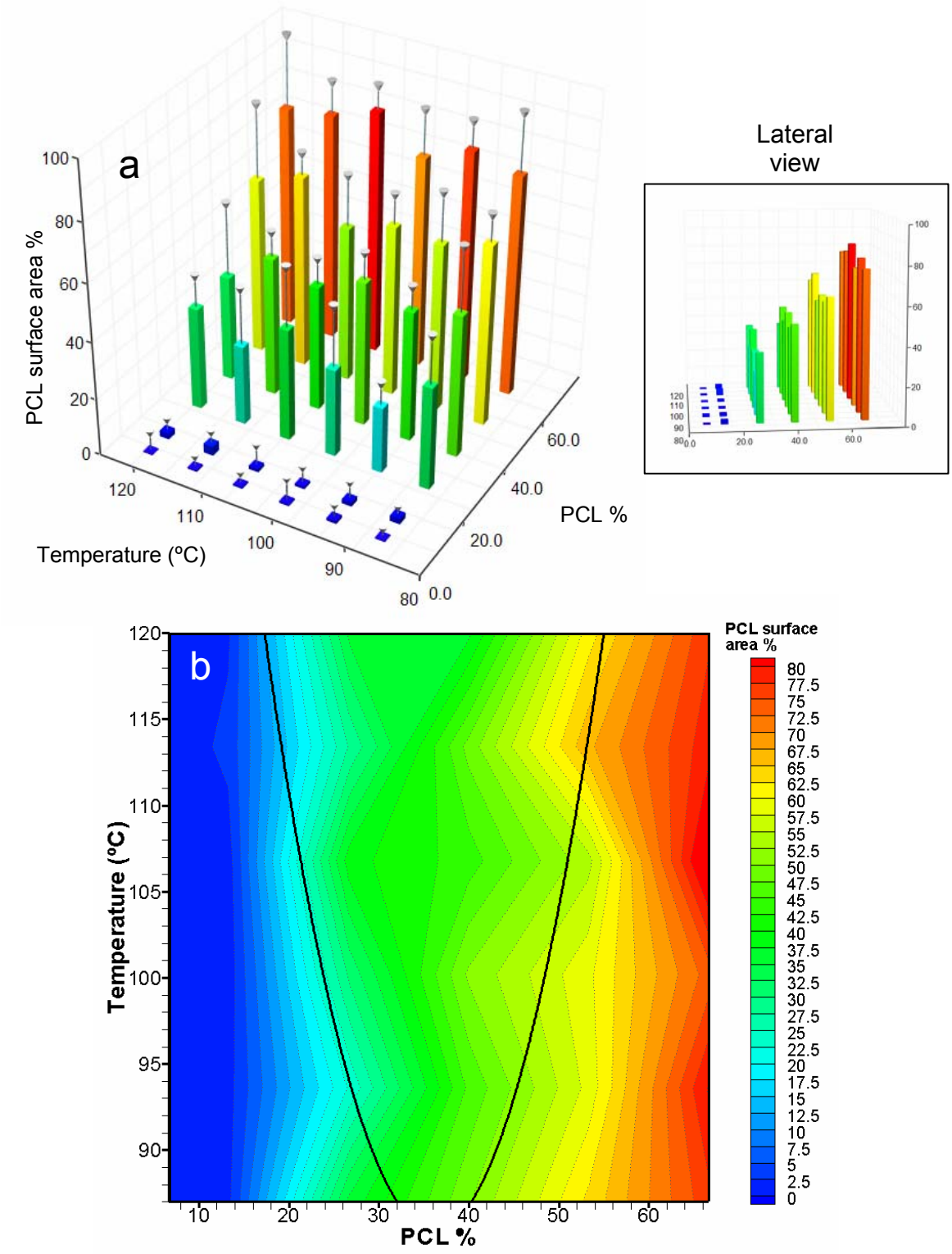

Figure 3.32. a) PCL surface coverage profile of a temperature-annealed PCL/PDLA composition-gradient library. Values presented as averages ± SEM (indicated by error bars delimited by inverted cone markers, n=4). b) Contour map of the PCL surface coverage values over the composition-gradient library.

Calculations of surface coverage were effectuated over the initial unfiltered overlay plane to exclude the “extra area” added by the filtering procedure; however, the program failed to properly recognize the particle edges and tended to open internal boundaries (i.e., rings) and merge domains depending on the lower particle size limit. This turned into a highly variable area coverage value.

The size (feret’s diameter) distribution of the PCL microdomains is displayed in figure 3.33, where the average sizes range from approximately 0.5 μm to 70 μm. In this case the influence of composition and annealing temperature was noticeably different than their effect over surface coverage, as the size of PCL microstructures increased with both composition and temperature. However, there is maximum limit to the size increment of PCL domains since, as mentioned earlier in section 3.3.3, at PCL concentrations above 58-60% a transition from the unstable region, below the spinodal curve, to the metastable region, between the spinodal and binodal curves, takes place and PCL becomes a continuous phase with dispersed PDLA droplet-like structures.

The deviation between the diameter values calculated from the 4 different libraries was higher towards the central area of the library, as seen form the standard error denoted by error bars in figure 3.33a. This variance is an expected outcome of the image analysis procedure, specifically the way feret’s diameter is calculated, since the area mentioned corresponds mainly to the region where a bicontinuous morphology is present. This morphology is characterized by “wavy” or “twisted” shapes whose maximal distance between boundary points depends greatly on “how” the structure is twisted, producing therefore less homogeneous results than those obtained from structures with circular or near-circular shapes.

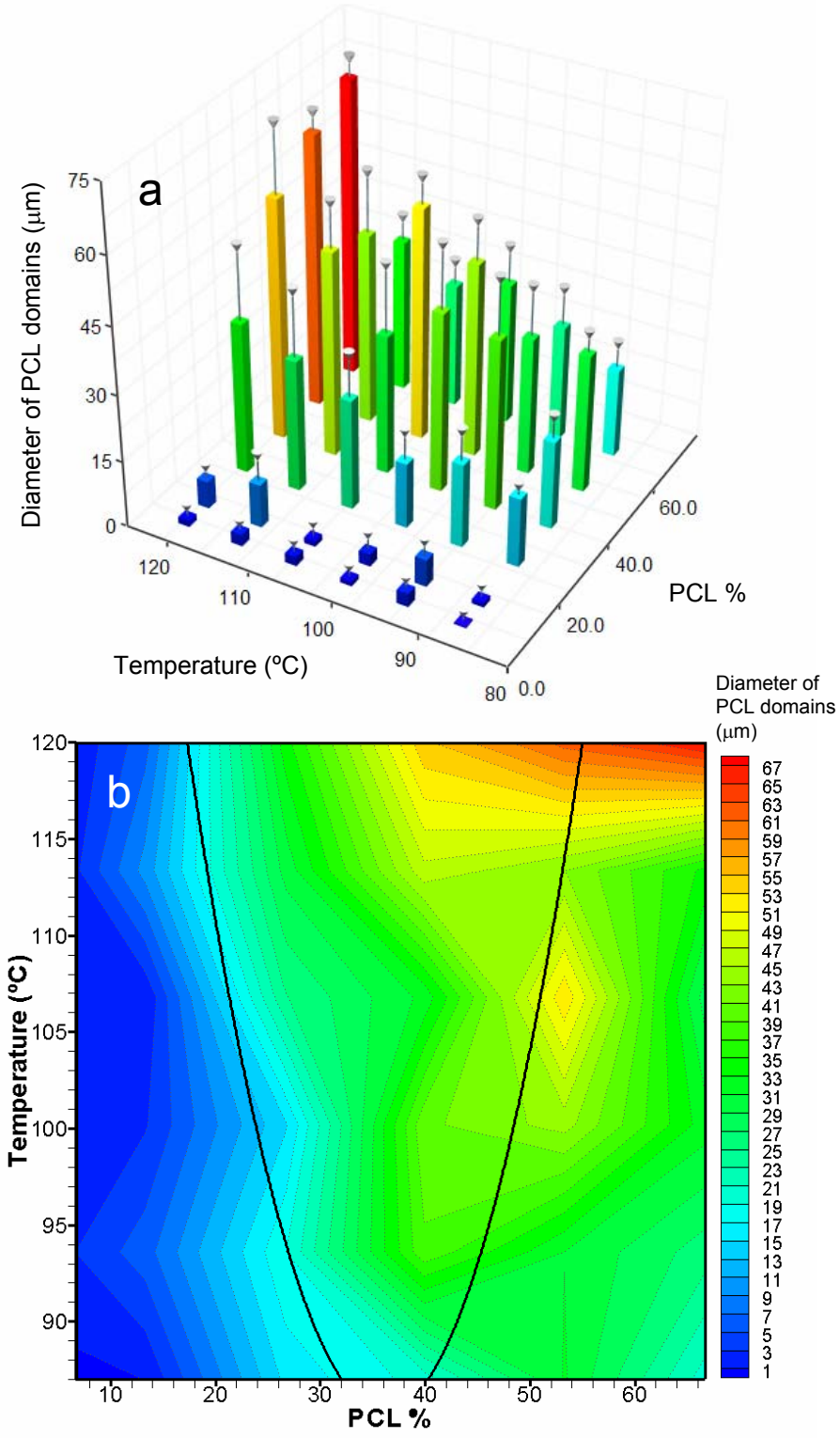

Figure 3.33. a) PCL domain feret's diameter profile across a temperature-annealed PCL/PDLA composition-gradient library. Values presented as averages ± SEM (indicated by error bars delimited by inverted cone markers, n=4). b) Contour map of the PCL domain feret's diameter values over the composition-gradient library.

The witnessed PCL-domain size increment with increasing temperature when moving along lines of constant composition inside the LCST regime (figure 3.33), is explained by a steady increase of free energy mismatch between the 2 phases due to polymer densification (entropic effect generated by a polymer free volume diminution). This mismatch obliges the 2 phases to lower their contact area with each other in order to keep the free energy difference at a minimum (equilibrium condition). The reduction in contact area is attained by coalescence of adjacent chemically akin domains, which *increases* domain size and lowers their specific area (area per unit mass).

The polymer densification effect, however, fails to explain the increment in PCL domain size noticed at high temperatures (~115-120ºC) and PCL concentrations higher than 55 % (figure 3.33). In this region PCL should be a continuous phase with dispersed PDLA-rich domains, and hence we should not expect to find PCL domains. What is more is that this trend is noticed *outside* the 2-phase regime (PCL % > 60 %) where the polymer surface should consist of a continuous PCL-rich phase. The only logic justification for this behavior is a “border effect” due to the library preparation process, as the region involved corresponds to the place where the stripe or polymer mix is painted prior to coating the film. This region in general has different characteristics (i.e., thickness) than the rest of the library.

One thing worth mentioning is that as temperature is incremented the enthalpic contribution to the free energy difference between PCL and PDLA diminishes while the entropic contribution increases (equation 2.14, section 2.3.2). This implies that as temperature rises the effect of polymer densification is higher and higher, and hence we would expect a diminution in PCL surface fraction (surface coverage) as the specific area of the PCL domains decreases (the polymer is “more dense”, then less area is required to “cover” the same amount of mass). However, from figure 3.32, it is evident that this is not the case with the PCL/PDLA libraries and that surface fraction coverage is

approximately constant along lines of constant composition. A possible explanation for this effect is that the enthalpic contribution to the free energy difference between both polymers *is not* that small in comparison to the entropic one. In other words, the energetic contribution is large enough, when summed to its entropic counterpart, to elicit LCST phase separation with minimal polymer free volume reduction (low polymer densification). This idea, however, has yet to be validated (future work). A plausible approach would be evaluating the surface fraction coverage of PCL domains at different locations over homogeneous chips (no composition gradient) with the same composition and annealed at different temperatures. This will allow to see, avoiding any possible influence induced by the temperature and composition gradients of the libraries, if the behavior noticed is due to thermodynamic effects, or if, on the contrary, it is related to the gradient libraries preparation techniques and/or their temperature gradient.

The similar behavior seen on surface roughness and microstructure size as a function of temperature and composition across the library, shows a close correlation between the two variables that suggests an increment in the PCL regime height as its specific surface decreases (increase in domain size). This increment raises the height difference between surface features (PCL and PDLA domains) which is directly reflected in the surface roughness value.

A mosaic of images of various distinct locations across a temperature-annealed PCL/PDLA library is shown in figure 3.34, where the effect of composition and temperature on the surface morphology is easily seen; namely, the transition from a PDLA-rich matrix with dispersed PCL-rich droplets to a continuous PCL-rich regime with dispersed PDLA-rich domains as PCL concentration increases, and the variation of microstructure size as temperature increases.

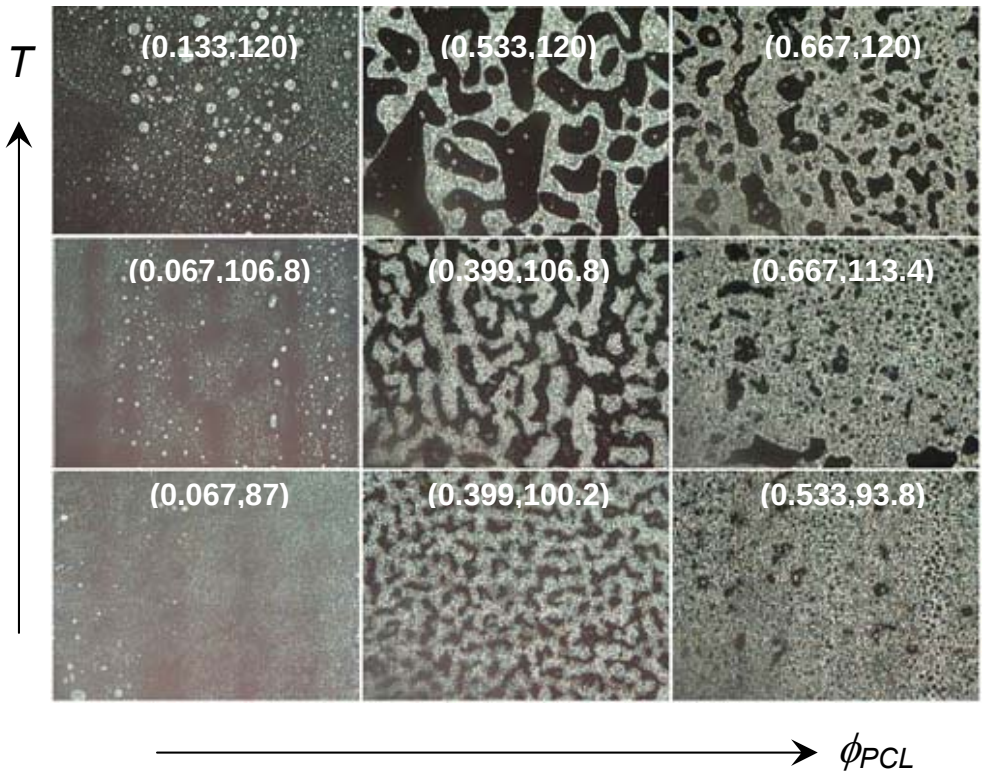

Figure 3.34. Variation of the PCL/PDLA surface microstructure as a function of temperature and composition. Bright=PCL-rich, dark=PDLA-rich. Numbers in parenthesis indicate PCL fraction (ϕ_{PCL}) and temperature (T) in ºC respectively (ϕ_{PCL},T).

3.4. SUMMARY

Composition-gradient libraries of the FDA approved biodegradable polymers PCL and PDLA were prepared over silicon substrata using the flow coating technique. Due a lower critical solution temperature phase behavior of the PCL/PDLA polymer blend, diverse surface morphologies were obtained by annealing the composition-gradient libraries under a continuous temperature gradient placed in an orthogonal fashion with respect to the composition gradient.

FTIR characterization of the combinatorial libraries confirmed the expected linear mass fraction variation of both polymers along the library, and revealed no significant

variation in composition due to polymer diffusion during the annealing process. Film thickness, examined by ellipsometry, was not constant and exhibited a linear ascent as PCL concentration increased. This variation was attributed to the viscosity disparity between the two polymer solutions. Phase separation of the blend, as expected, played a critical role in surface morphology variation. For example, surface roughness was noticeably enhanced in the demixed region of the library, especially in the upper limit inside the LCST regime (late phase separation); whereas PCL structure size exhibited a steady increment with temperature attributable to the increasing disparity of free energy of PCL and PDLA-rich phases inside the phase-separated regime.

3.5. CONCLUSION

Characterization results show that the methodology followed in the preparation of combinatorial libraries allows to effectively creating patterned surfaces with controllable morphologies via temperature and composition variation. Moreover, it stands as a novel approach to obtain patterned surfaces of biodegradable polymer blends (when they exhibit LCST and/or UCST phase behavior) to be used in biological assays, that rivals standard techniques based on pattern embossing onto polymer surfaces of templates created by photolithography processes.

REFERENCES

1. **Ward I.M., *Mechanical properties of solid polymers*. 2 ed. 1983, New York: Wiley. 475.**

2. **Macaúbas P.H., Demarquette N.R., *Rheology as a Tool for Immiscible Polymer Blends Characterization:Interfacial tension and compatibilization*, in *RheoFuture*. 2002, Thermo Electron Coporation: Karlsruhe, Germany.**

3. **Willemse R.C., de Boer A.P., van Dam J., and Gotsis A.D., *Co-continuous morphologies in polymer blends: the influence of the interfacial tension.* Polymer, 1999. 40: p. 827-834.**

4. **Langer R., Vacanti J., *Tissue engineering.* Science, 1993. 260(5110): p. 920-926.**

5. **Brocchini S., James K., Tangpasuthadol V., and Kohn J., *Structure-property correlations in a combinatorial library of degradable materials.* Journal of Biomedical Materials Research, 1998. 42: p. 66-75.**

6. **Hrkach J.S., Ou J., Lotan N., and Langer R., *Synthesis of poly(L-lactid acid-co-lysine) graft copolymers.* Macromolecules, 1995. 28: p. 4736-4739.**

7. **Meredith J.C., Amis E.J., *LCST phase separation in biodegradable polymer blends: poly(D,L-lactide) and poly(ε-caprolactone).* Macromol. Chem. Phys., 2000. 201(6): p. 733-739.**

8. **Reed A.M., Gilding D.K., *Biodegradable polymers for use in surgery - poly(glycolic)/poly(lactic acid) homo and copolymers: 2. In vitro degradation.* Polymer, 1981. 22(4): p. 494-498.**

9. **Ratner B.D., Hoffman A.S., Schoen F.J., and Lemons J.E., ed. *Biomaterials Science: An introduction to materials in medicine*. 1 ed. 1996, Academic Press: San Diego, CA. 484.**

10. **Nam Y.S., Park T.G., *Porous biodegradable polymeric scaffolds prepared by thermally induced phase separation.* Journal of Biomedical Materials Research, 1999. 47: p. 8-17.**

11. **Engelberg I., Kohn J., *Physicomechanical properties of degradable polymers used in medical applications: A comparative study.* Biomaterials, 1991. 12: p. 292-304.**

12. **Broz M.E., VanderHart D.L., and Washburn N.R., *Structure and mechanical properties of poly(d,l-lactic acid)/poly(ε-caprolactone) blends.* Biomaterials, 2003. 24: p. 4181-4190.**

13. **Meredith J.C., Karim A., and and Amis E.J., *High-Throughput Measurement of Polymer Blend Phase Behavior.* Macromolecules, 2000. 33: p. 5760-5762.**

14. **Karim A., Sehgal A., Amis E.J., and Meredith J.C., *Combinatorial mapping of polymer blends phase behavior*, in *Experimental design for combinatorial and high throughput materials development*, J.N. Cawse, Editor. 2003, John Wiley & Sons, Inc.: Hoboken. p. 73-88.**

15. **All the process was controlled using a custom labview® code based on a code originally written by Dr. J.C. Meredith . Modifications to the original code were done accordingly to the requirements of the project.**

16. **Meredith J.C., Smith A.P., Karim A., and Amis E.J., *Combinatorial Materials Science for Polymer Thin-Film Dewetting.* Macromolecules, 2000. 33: p. 9747-9756.**

17. **Leclair A., Favis B.D., *The role of interfacial contact in immiscible binary polymer blends and its influence on mechanical properties.* Polymer, 1996. 37: p. 4723-4728.**

18. **Reich S., Cohen Y., *Phase Separation of Polymer Blends in Thin Films.* Journal of Polymer Science, 1981. 19: p. 1255-1267.**

19. **Wilkinson M.H.F., Schut F., ed. *Digital Image Analysis of Microbes: Imaging, morphometry, fluorometry and motility techniques and applications*. 1st ed. 1998, John Wiley & Sons: West Sussex. 551.**

20. **Kindratenko V., *Development and Application of Image Analysis Techniques for Identification and Classification of Microscopic Particles*, in *Departement Scheikunde*. 1997, University of Antwerp: Antwerp, Belgium.**

21. ***http://rsb.info.nih.gov/ij/docs/menus/analyze.html*.**

CHAPTER IV

EFFECT OF PCL/PDLA LIBRARIES SURFACE TOPOGRAPHY ON CELL BEHAVIOR

4.1. INTRODUCTION

Non-living material like bone mineral and collagen and elastin fibers are found in substantial quantities in most tissues. The major, and extremely important, role of this material is to provide mechanical strength and support to the tissue. Indeed, without collagen we would collapse as piles of cells onto the floor [1]. Therefore, when tissue is to grow outside its native environment, mechanical support that mimics that found in such environments has to be provided. This task is commonly accomplished by the use of “external” materials. However, although a myriad of different materials can be engineered to meet the required mechanical characteristics (i.e., metals, polymers, ceramics, and composites), the success of their use is dictated by another factor: the material-cell interaction.

The interaction of cells with external materials is an exceptionally complicated matter and is of enormous relevance for the development of useful biomaterials in numerous fields. Biocompatible materials find use in several diverse applications like cell culture devices, bioreactors, protein handling, and lately in the bioelectronics field to create state-of-the-art cell-silicon “biochips” [2]. However, the main use of biomaterials resides in the domain of tissue engineering and biomedicine where they are commonly used as scaffolds to grow or repair tissue, and as prosthetic implants.

Surface chemistry has been found to be a crucial aspect in determining the degree of biocompatibility of a particular material [3]. In fact surface chemical groups of

synthetic materials have been shown to interact intimately with the extracellular matrix, and have a strong effect on focal adhesions and close contacts [4], which, in turn, regulate cell function and signaling [5-8].

Custom modifications of the surface chemical characteristics of synthetic materials have been a popular and effective way to improve biocompatibility and to control cell behavior [1, 3, 8-16]. For example, the surface of polyester (PET) membranes used in biohybrid organ technology has been modified by allylamine-plasma coating to improve cell adhesiveness, maintaining the mechanical properties of the PET support [9]. Other approaches involve grafting of different functional groups over polymer surfaces [11, 16], and the construction of biomimetic scaffolds by polymer surface functionalization with immobilized peptides such as RGD-containing ligands [10, 17, 18].

There is abundant evidence that cell shape per se has a major effect on several cellular events such as proliferation, differentiation, cytoskeletal organization, and gene expression [19, 20]. It has been shown that the fabrication of patterned surfaces that combine bioactive and inert chemistries can be utilized to systematically modulate cell function by molding cell shape [13, 14, 19, 21-24]. However, cells are also strongly sensitive to surface topographical features, having a particularly marked effect on cell morphology, and hence cell function [20, 25]. Microgrooved substrata, for example, has been found to provoke cellular orientation, known as contact guidance, in fibroblasts and Schwann cells [26, 27], and to increase cell F-actin polymerization in macrophages which, in turn, influences cell orientation and movement [28]. Cell migration and adhesion [12], as well as proliferation and protein expression [29] have been also shown to be affected a great deal by substratum roughness. Numerous other studies elucidate the importance of surface texture and roughness of implant materials on cell responsiveness and cell-surface integration [30-33].

Table 4.1 presents the most common biological reactions attributed to topographical features.

Table 4.1. Biological reactions to topography [1].

Cell orientation
Cell adhesion
Cell movement
Gene expression
Activation of phagocytosis
Orientation of the cytoskeleton

Engineered micropatterned surfaces are commonly used to conduct tests designed specifically to delineate cell response to surface topography, since control over surface features can be achieved. Fabrication of such surfaces has been done largely by photolithography of silica or silicon followed by dry etching, and by electron beam lithography (for nanometer-sized features). Embossing and casting techniques have also been used to transfer photolithographic patterns to polymer surfaces [1]. These 2D techniques, however, are generally expensive, time consuming, and do not lend themselves to the creation of patterns on 3D tissue scaffolds.

Emerging alternatives like demixed polymer blends are gaining momentum as they are less expensive and easier to fabricate into 3D devices, and they have been proven to influence cell behavior positively. Polymer demixed islands, for example, have been shown to influence cell spreading and elicit cytoskeletal changes, as well as up-regulate gene expression in immortalized human fibroblasts and human endothelial cells [34-36].

The advent of state-of-the-art combinatorial and high throughput screening techniques into polymers and material science can significantly ease the complex task of

characterizing the interactions between cells and biomaterials. Brocchini and coworkers [16] have shown that combinatorial approaches are valuable tools in biomaterial design, by creating a *discrete* combinatorial library of 112 distinct polyarylates via parallel copolymerization of different aliphatic acids with various tyrosine-derived diphenols. This discrete library allowed systematic study of material dependant biological responses. Meredith et al [37], have gone one step further by successfully using novel combinatorial libraries of PCL/PDLA polymer blends with *continuous* composition and temperature gradients that, due to the blend's LCST phase behavior (polymer demixing, section 3.1), create a continuous variation of surface topography across the libraries. These libraries allow concurrent evaluation of the effect of thousands of dissimilar surface characteristics on cell attachment and gene expression.

Here we revisit the previous work of Meredith and coworkers [37], and extend it to other key developmental stages of MC3T3-E1 osteoblast-like cells, namely, cell attachment and spreading, proliferation, viability, gene expression, and mineralization.

4.2. MATERIALS AND EXPERIMENTAL METHODS

4.2.1. CELLS

Immature mouse osteoblast-like MC3T3-E1 cells, acquired from the RIKEN bioresource center cell bank (Ibaraki, Japan), were used throughout all the experiments. This cell line exhibits a sequential expression of osteoblast characteristics analogous to in vivo bone formation, namely, a proliferative stage of undifferentiated osteoblast precursors followed by expression of a differentiated osteoblast phenotype, after which matrix mineralization occurs [38-40]. A simplified representation of the sequential

upregulation of osteoblast-specific markers during the different developmental stages of MC3T3-E1 cells is outlined in figure 4.1.

4.2.2. CELL CULTURE

Before the experimental runs, MC3T3-E1 cells were subcultured in 150mm tissue culture treated polystyrene dishes (Corning, Inc.) with supplemented cell culture media consisting of 89% Minimum Essential Medium (MEM) α-Medium (1X) (Invitrogen Corp.), 10% characterized fetal bovine serum (FBS) (Hyclone), and 1% penicillin-streptomycin (invitrogen Corp.), at 37 ºC and 5% CO_c.

PCL/PDLA composition/temperature gradient libraries (sections 3.2.1 and 3.2.2), used as substrates for the cell culture experiments, were sterilized by complete immersion in 70% ethanol for 5-10 minutes, followed by two consecutive washes in sterile complete phosphate-buffered saline (PBS) (1X) to remove any ethanol remaining over the surface of the library.

To avoid any influence of secreted proteins (i.e., osteocalcin), expressed by cells attached to the culture well, Costar® six-well ultra low attachment microplates (Corning, Inc.) (individual well diameter = 35 mm) were used to place the sterilized 24 x 24 mm libraries. These wells are covered with a hydrophilic and neutrally charged covalently bound hydrogel layer that inhibits the hydrophobic and ionic interactions involved in protein adsorption, and therefore cell attachment. Each library was allowed to sit flat on the bottom of the wells to rule out any possible effect that might be caused by surface inclination.

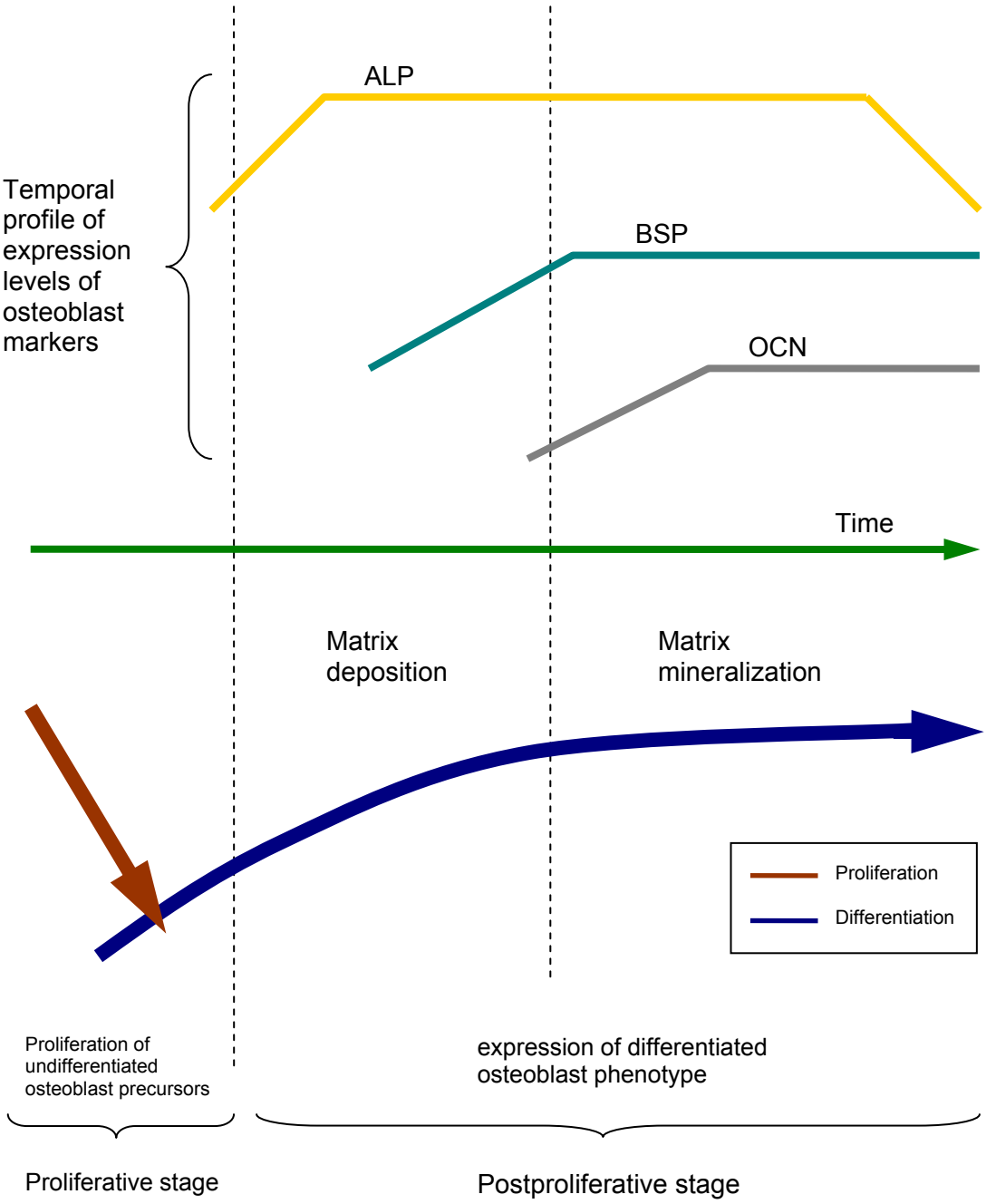

Figure 4.1. Simplified graphic representation of the developmental stages of MC3T3-E1 osteoblast-like cells (based on [38, 40, 41]).

Prior to the seeding of the subcultured MC3T3-E1 over the combinatorial chips, cells were washed with sterile calcium and magnesium free PBS (1X) (Invitrogen Corp.) and detached by trypsinization with Trypsin-EDTA (0.05% Trypsin, 0.53 mM EDTA•4Na) (1X) (Invitrogen Corp.). Cells were seeded over the libraries at a density of 5000 cells/cm^2 in 89% α-MEM supplemented with 10% FBS and 1% penicillin-streptomycin (total working volume per well was 3 ml). Positive controls were prepared by seeding 35 mm tissue culture treated polystyrene dishes (Corning, Inc.) at identical conditions.

To promote the expression of differentiated osteoblast phenotype and stimulate matrix mineralization, 50 μg/ml L-(+)-Ascorbic acid (vitamin C) (Sigma-Aldrich, Inc.) and 3 mM β-Glycerol phosphate (Sigma-Aldrich, Inc.) were incorporated to each media change [38, 42, 43]. For runs longer than 2 days, supplemented media was exchanged every other day.

Negative controls were prepared when required by replacing the supplemented media with non-supplemented media (serum free media) 5 to 7 hours after the initial seeding.

4.2.3. BIOASSAYS

Ironically one of the main issues involved in the use of continuous-gradient combinatorial libraries to assess cell-surface interaction, is that the libraries are not uniform. Properties of a particular region of the library are different than those of its neighboring regions, and consequently its effect on cell function is expected to be different as well. This hinders the possibility of using popular and well established techniques, especially when evaluating protein expression, such as ELISA, since the results would reflect the average contribution of the whole library, but would fail to give

any information about a particular spot. Hence, assays have to be completed over the library itself.

Each assay was done over 6 separate combinatorial PCL/PDLA libraries. Results were averaged between the 6 libraries and presented as average ± standard error mean (SEM).

4.2.3.1. CELL ADHESION AND SPREADING (MORPHOLOGY)

Initial cell attachment and spreading over PCL/PDLA libraries was determined via immunofluorescence staining 6 hours after the initial seeding. Cytoskeleton F-actin fibers were labeled to identify cell shape, whereas focal adhesion localized vinculin was labeled to locate attachment points.

Once the culture was terminated, cells were washed 2 times with 3 ml of PBS and then *permeabilized* for 10 min with 2ml of cytoskeleton buffer[a] at 4 ºC and pH 6.8, plus 0.5% detergent (triton X-100, IBI/Shelton Scientific) and protease inhibitors[b]. Cell *fixation* was done with cold (4 ºC) 3.6 % (v/v) formaldehyde in PBS for 5 min followed by 1 hour *blocking* with blocking buffer (5% FBS in PBS). After several washes in PBS, the primary antibody, mouse anti-vinculin IgG (Upstate Group Inc.), was added to stain for target proteins and incubated at room temperature for 1 hour. Secondary antibodies, conjugated rhodamine phalloidin (Molecular Probes, Inc.) and Alexa Fluor® 488 goat anti-mouse IgG (H+L) (Molecular Probes, Inc.), were added and incubated in the dark for 1 hour at room temperature to provide signal from primary antibodies. After the incubation period samples were rinsed thoroughly in PBS and DIH_2O, and then mounted on microscope slides. Cell density was quantified using the nuclear DNA stain Hoechst

[a] 50 mM NaCl, 150 mM sucrose, 3 mM $MgCl_2 \cdot 6H_2O$, 50 mM TRIS (J.T. Baker)
[b] 20 μg/ml Aprotinin, 1 μg/ml Leupeptin (Sigma-Aldrich, Inc.), 2 mM phenylmethylsulfonylfluoride (PMSF) (EM Science)

(bisbenzimide) (Molecular Probes, Inc.), which was added simultaneously with the secondary antibodies. Qualitative identification of the samples was done by fluorescence microscopy using a Nikon Eclipse E4000 fluorescence microscope (Nikon Corp.)[c] coupled with a SPOT RT slider camera (Diagnostic Instruments, Inc.).

It is important to mention that the PCL/PDLA polymer blend presents noticeable autofluorescence, especially under blue and green filters (wavelength emission range from 420 to 525 nm) (figure 4.2). Thus an appropriate concentration of antibodies is required for proper labeling while avoiding increased polymer autofluorescence due to possible non-specific binding. The following dilutions of stock antibodies in PBS were found to give satisfactory results: mouse anti-vinculin IgG 1:500, conjugated rhodamine phalloidin 1:200, Alexa Fluor® 488 1:200, and Hoechst 1:10000.

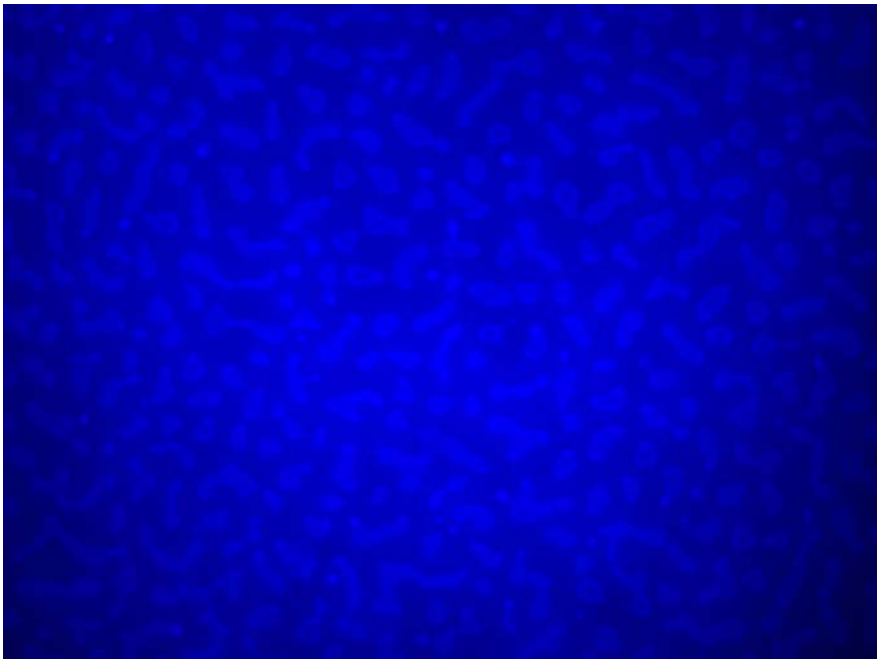

Figure 4.2. Blue autofluorescence emission of a PCL/PDLA library excited with a 379-401 nm source. Brighter sections correspond to PDLA structures.

[c] This equipment was used for all the different immunofluorescence tests

4.2.3.2. CELL PROLIFERATION

A preliminary approach to assay proliferation utilized the thymidine analog 5-bromo-2'-deoxyuridine (BrdU), preferentially incorporated into newly replicated DNA, using the ABSOLUTE-S™ SBIP cell proliferation assay kit (Molecular Probes, Inc.). To avoid harsh DNA denaturation methods that thwart the possibility of simultaneous cell-labeling procedures on the same sample (i.e., viability), the assay relies on the strand breaks induced by photolysis to make the BrdU epitope accessible to the detecting antibody.

Initial tests on TCPS dishes, following the kit's recommended experimental protocol, showed high levels of cell membrane fluorescence with full absence of nuclear staining (figure 4.3), suggesting non-specific binding of the BrdU photolyte and/or the labeled anti-BrdU secondary antibody, and poor membrane permeabilization.

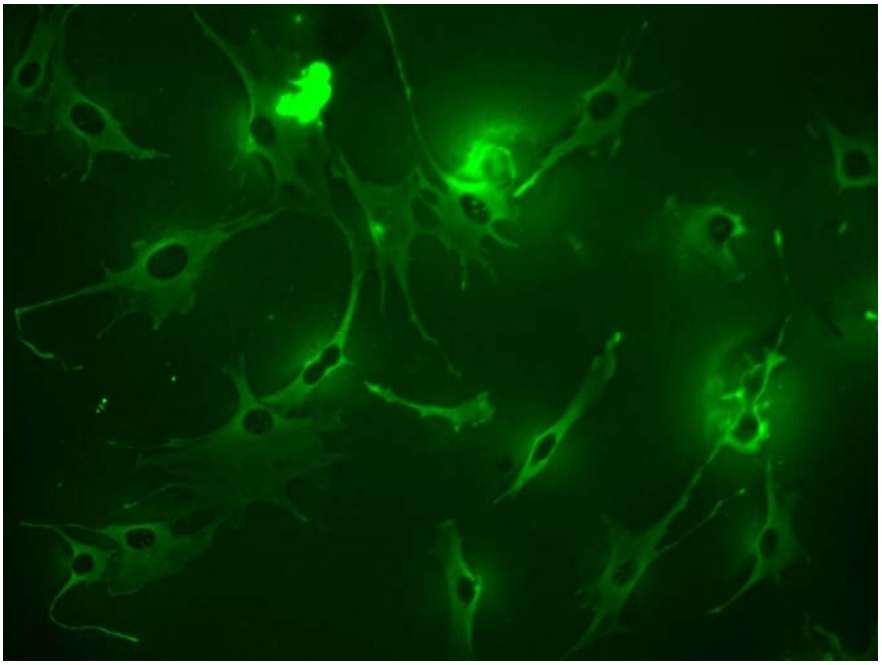

Figure 4.3. Fluorescence microphotography (green channel) of a 2-day proliferation assay of MC3T3-E1 cells on TCPS using the ABSOLUTE-S™ SBIP cell proliferation protocol.

Modifications to the original protocol were performed to solve initial issues by incorporating a detergent (triton X-100) to the permeabilization phase, and reducing the secondary antibody concentration. Results were mixed as cell nuclei were successfully marked, whereas cell membranes still showed considerable fluorescence levels (figure 4.4).

Membrane fluorescence turned out to be a significant issue as the PCL/PDLA libraries autofluorescence seemed to be noticeably enhanced by the UV light irradiation used during DNA photolysis. The combined effect of enhanced polymer autofluorescence and cell membrane fluorescence made the distinction of proliferated and non-proliferated cells practically impossible.

A protocol based on the proliferation assay described by Datta et al [44] was used as an alternative to the procedure recommended by the ABSOLUTE-S™ SBIP cell proliferation protocol due to the abovementioned issues.

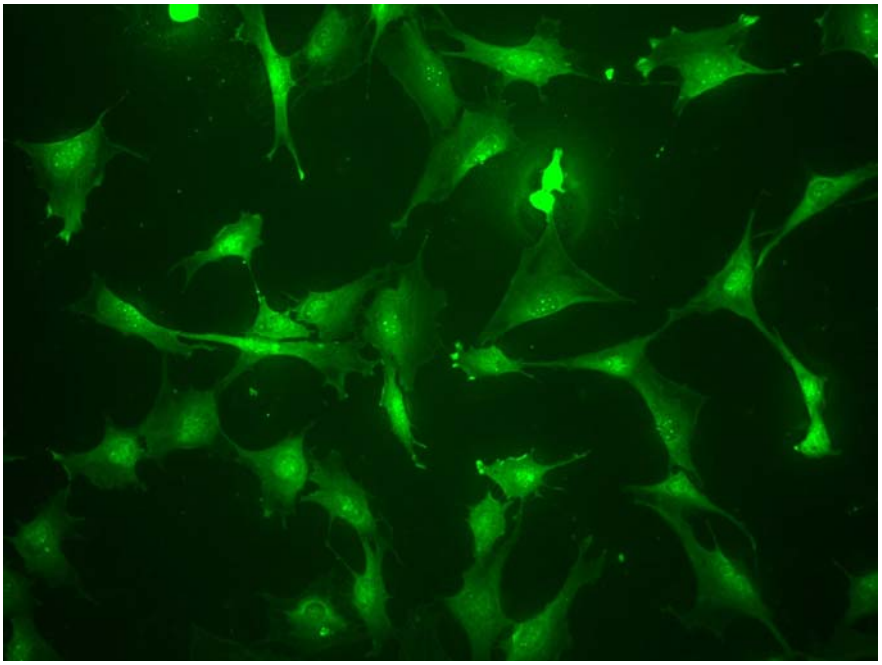

Figure 4.4. Fluorescence microphotography (green channel) of a 2-day proliferation assay of MC3T3-E1 cells on TCPS using a modification of the ABSOLUTE-S™ SBIP cell proliferation protocol.

BrdU (Sigma-Aldrich, Inc.) was added to the cell culture media prior to cell fixation and incubated for 6 hours at 37 ºC and 5% CO_2 to allow its incorporation into new replicated DNA. Following the incubation period, samples were washed 3 to 5 times in PBS (5 min/wash); treated with ice-cold 2N HCl for 20 min to fix the cell layer and denature DNA strands; and washed 3 times with a 100 mM TRIS, 50 mM NaCl solution (pH 7.6) (20 min/wash). Subsequent blocking was carried out for 1 hour at room temperature with 5% goat serum blocking buffer (5% goat serum in PBS). Monoclonal anti-BrdU (clone BU 33, Sigma-Aldrich, Inc.) was diluted 1:1000 in PBS and incubated for 1 hour after the blocking stage. Samples were thoroughly washed 5 times with PBS (5 min/wash) prior to the addition of the Alexa Fluor® 488 conjugated secondary antibody (1:200 in PBS) to provide signal from the monoclonal anti-BrdU. Cell density was estimated by simultaneous addition of Ethidium homodimer-2 (EthD-2) (Molecular Probes, Inc.) diluted 1:2000 in PBS. The labeling solution was removed after an incubation period of 1 hour in the dark at room temperature, and followed by exhaustive washing in PBS (5 washes, 10 min/wash) and in DIH_2O prior to dry mounting.

Optimal BrdU concentration for the application was ascertained by trial runs and found to be 100 μg/ml (figure 4.5).

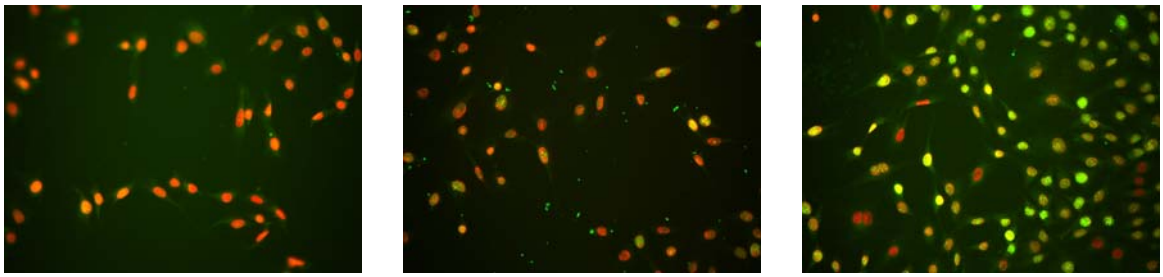

Figure 4.5. Representative immunofluorescence images of some of the 2-day proliferation trial runs effectuated to determine optimal BrdU concentration (Green: BrdU, Red: EthD-2). From left to right: 10 μg/ml, 50 μg/ml and 100 μg/ml. Original magnification 20x.

Cell proliferation was monitored on separate libraries at 3, 4, 5, 8 and 13 days after the initial culture.

4.2.3.3. PROTEIN EXPRESSION

During their developmental stages, especially during the postproliferative phase where downregulation of replication is associated with expression of osteoblast functions, osteoblasts express various characteristic proteins typically called osteoblast markers. These markers include alkaline phosphatase (ALP), osteopontin (OPN), osteonectin (ON), osteocalcin (OCN) and bone sialoprotein (BSP).

The expression of alkaline phosphatase and osteopontin increases time-dependently during osteoblastic differentiation and maturation (early markers), while osteocalcin and bone sialoprotein are expressed only after cells reach the mineralized tissue-formation stage (late markers) [45] (figure 4.1).

We evaluated the effect of PCL/PDLA libraries on the expression of one early and one late marker, namely, alkaline phosphatase, which is already expressed in some proliferative osteoprogenitors and preosteoblasts; and osteocalcin, which is upregulated only at the postproliferative osteoblast stage [41].

4.2.3.3.1. ALKALINE PHOSPHATASE EXPRESSION

Alkaline phosphatase activity was quantified using the histochemical procedure depicted by McGee-Russel [46] after 6-day and 8-day cultures.

Cells were washed with PBS and fixed with 70% ethanol for 15 min after 6 or 8 days in culture. Following fixation, samples were rinsed in diH_2O and incubated for 1

hour with an ALP staining solution. After the incubation period samples were washed once more time with DIH_2O and then dried.

The staining solution was prepared by dissolving Na-α-naphtylphosphate (Sigma-Aldrich, Inc.) and fast blue RR salt (Sigma-Aldrich, Inc.) in a 50 mM TRIS mix (pH 10) at a ratio of 2 mg/ml each.

4.2.3.3.2. OSTEOCALCIN EXPRESSION

Osteocalcin expression was examined after 13 and 14 days in culture by immunofluorescence, using a very similar staining procedure to that used for f-actin staining (section 4.2.3.1).

Following 13 or 14 days in culture cells were washed with PBS and permeabilized for 10 min in an ice-cold (4 ºC) 0.5% triton X-100 detergent solution. Cold (4 ºC) 3.6 % (v/v) formaldehyde in PBS was added for 5 min to fix the cells, followed by 1 hour blocking with 5% FBS in PBS. Goat anti-mouse osteocalcin (Biomedical Technologies, Inc.), the primary antibody, was added at a dilution factor of 1:50 and incubated at room temperature for 1 hour. Alexa Fluor® 350 donkey anti-goat IgG (H+L) (Molecular Probes, Inc.), used as secondary antibody, was diluted to 1:100 and placed onto the sample to provide signal from the osteocalcin antibody. Incubation time was 1 hour in the dark at room temperature. After the incubation period samples were thoroughly rinsed in PBS and DIH_2O, and then mounted on microscope slides.

4.2.3.4. MINERALIZATION

Mineralization of extracellular matrix, which marks the final phase of osteoblast phenotypic development, was quantified by Von Kossa staining [47] for 13-day and 14-day cultures.

Cultures were fixed in 70%, rinsed with DIH_2O and incubated with 5% silver nitrate ($AgNO_3$). Incubation was carried out a room temperature with the samples exposed to *very bright* light. After removal of the silver nitrate solution, 5% sodium thiosulfate (Na_2SO_3) was added to fix the staining. Finally the samples were thoroughly rinsed with DIH_2O and dried.

4.2.3.5. VIABILITY

Cell viability was evaluated with the LIVE/DEAD® Viability/Cytotoxicity kit (Molecular Probes, Inc.), a two-color fluorescence assay that determines live and dead cells simultaneously by measuring intracellular esterase activity, via calcein AM, and plasma membrane integrity, via ethidium homodimer (EthD-1).

Samples were concurrently stained with calcein AM and EthD-1 during incubation periods of 45 minutes at room temperature. Optimal dye concentrations were found to be approximately 1.8 to 2.1 μM for calcein AM and 3.6 to 4.2 μM for EthD-1, depending on the sample substrate (TCPS or PCL/PDLA libraries) and culture time. Following the incubation phase, quantification of cell viability was completed by fluorescence microscopy.

Cell viability assays were performed in parallel (separate libraries) with each of the aforementioned tests.

4.3. RESULTS AND DISCUSSION

4.3.1. CELL ATTACHMENT AND MORPHOLOGY

The initial osteoblast attachment density to combinatorial libraries after a 6-hour culture is shown in figure 4.6.

The number of adherent cells per unit area was significantly greater on areas of moderate to low PCL concentration ($\phi_{PCL} \leq 0.5$), reaching the highest attached cell density levels (~2100 cells/cm^2, comparable to cell density on positive TCPS controls) below a PCL mass percentage of 30% ($\phi_{PCL} = 0.3$). Below this value cells adhered equally to regimes inside *and* outside the LCST boundary, suggesting a direct influence of surface chemistry on cell attachment.

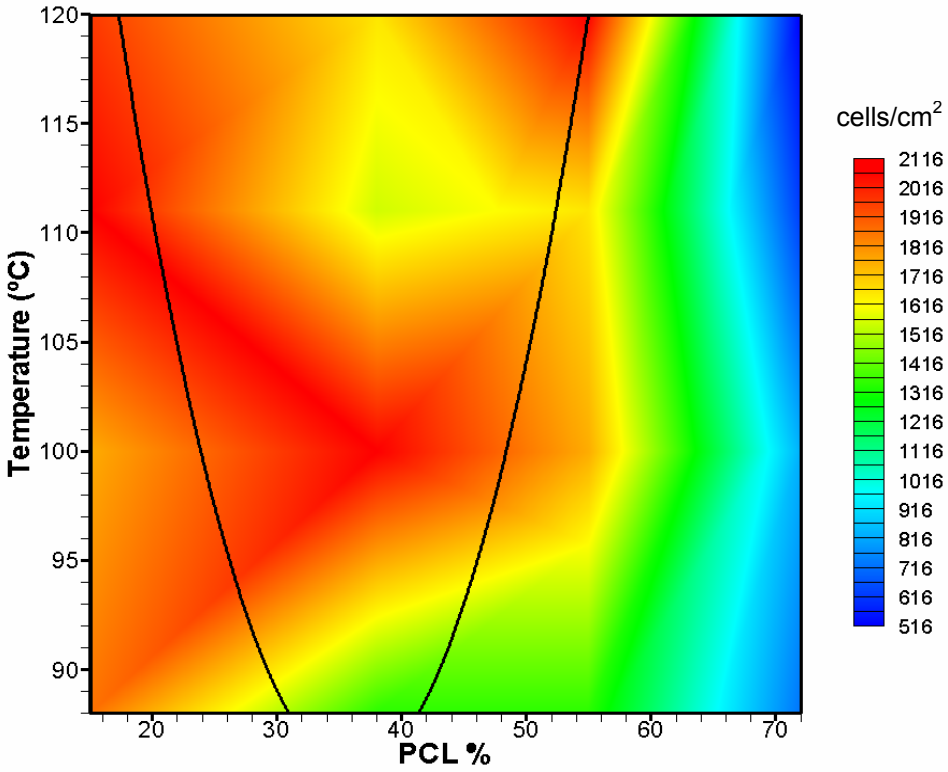

Figure 4.6. MC3T3-E1 attachment density over a PCL/PDLA combinatorial library after a 6-hour culture period. Cell density presented as cells/cm^2 (average values over 5 libraries). Black line denotes the LCST boundary.

Surface wettability (hydrophobicity) of PCL and PDLA, evaluated by measuring the static contact angle of deionized distilled water, was determined to ascertain whether enhanced attachment occurred over a more hydrophilic or more hydrophobic surface. Measurements were performed with a Rame-Hart 100 goniometer, obtaining average contact angles of 60.44º ± 0.37º and 78.54º ± 0.81º for pure PDLA and pure PCL respectively (figure 4.7). The slightly higher hydrophilicity of PDLA compared to PCL, attributable to its shorter hydrocarbon chain, suggests that cells attach preferentially to regions with higher overall surface energy (more hydrophilic) rather than to low surface energy ones (less hydrophilic).

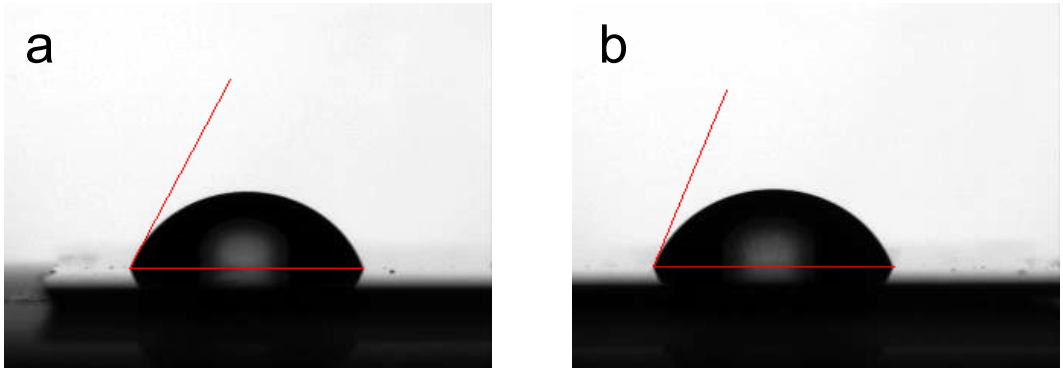

Figure 4.7. Static contact angle for a) pure PDLA (60.44º ± 0.37º) and b) pure PCL (78.54º ± 0.81º). Angles were measured using ImageJ image analysis software (NIH, public domain).

Although FACs were virtually impossible to resolve on the combinatorial libraries, due to the high level of fluorescent green background of the polymer that masked the vinculin stain, high magnification long exposure images of the rodhamine phalloidin stained F-actin fibers revealed that in fact cells adhere to the more hydrophilic PDLA. Since both polymers present a different level of autofluorescence when excited with a particular wavelength, images taken over different spots on the library were overexposed to a wavelength of 530-560 nm (red filter) for approximately 12 to 15 seconds with a gain of 8 in order to make possible the distinction between PCL and PDLA structures. The

overexposure was responsible for the bad resolution of the f-actin fibers of the cytoskeleton, which looks like a continuous red membrane over the cell; however, it made possible to observe that cells were stretching between PDLA rich domains (highlighted areas in figure 4.8), or even following the shape of PDLA structures.

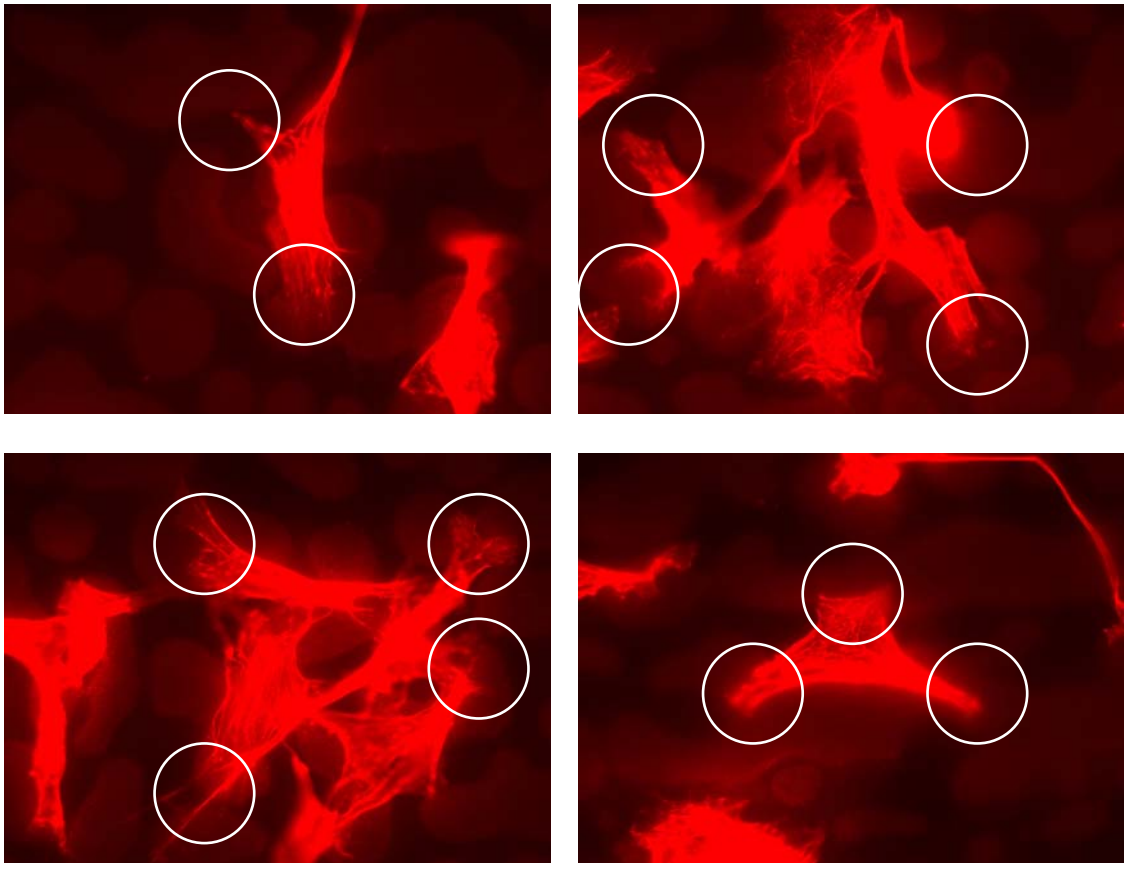

Figure 4.8. Overexposed images of MC3T3-E1 osteoblasts adhered on different locations of combinatorial PCL/PDLA libraries. Brighter and darker background structures correspond to PDLA-rich and PCL-rich domains respectively. Highlighted areas show cell attachment points onto PDLA structures. Original magnification 60x.

Hydrophobic surfaces adsorb comparatively more fibronectin and other serum proteins than hydrophilic surfaces. However it has been shown that hydrophobic substrata do not promote adhesion and spreading of fibroblasts [48, 49], and that *moderately* hydrophilic surfaces are more favorable for mammalian cell adherence [49].

Hence, the preferential attachment of MC3T3-E1 osteoblasts to PDLA-rich areas, regardless of the surface microstructure, seems to be regulated by the slightly higher overall surface energy of PDLA-rich zones. This phenomenon may be attributable to conformational changes of adsorbed adhesive proteins, specially fibronectin, as strong hydrophobic interactions may inhibit necessary protein receptors rearrangement resulting in loss of biologic activity and hence poor cell adhesion and spreading [50, 51]. Furthermore, conformational changes in fibronectin have been shown to elicit alterations of other cell events such as proliferation and phenotypic expression in MC3T3-E1 immature osteoblasts and mouse myoblats [52, 53]. It is important to notice that extremely hydrophilic surfaces (i.e., hydrogels) have the same effect as hydrophobic substrata on adhesion and spreading [54].

Even though cell attachment seemed to be unaffected by the surface topography, spreading and cytoskeletal rearrangement (cellular responses of attachment) seemed a marked dependence to surface features as well spread multipolar morphologies were predominant on the rougher surface of the LCST regime, while bipolar spindle-shaped cells were present outside the 2-phase region (figure 4.9). This is explained by the fact that cell adhesion and spreading are two separate phenomena. For example, the attachment strength to a surface is not correlated with the area of contact (spreading). A cell attached onto Teflon is easily removed even though it presents a well spread morphology, while an elongated cell on glass will strongly adhere and cannot be easily detached [2].

Cells with stellate morphology displayed numerous highly organized f-actin stress fibers and high cell area, while the second morphology characterized by a bipolar shape presented reduced cell area and minimal f-actin stress fibers.

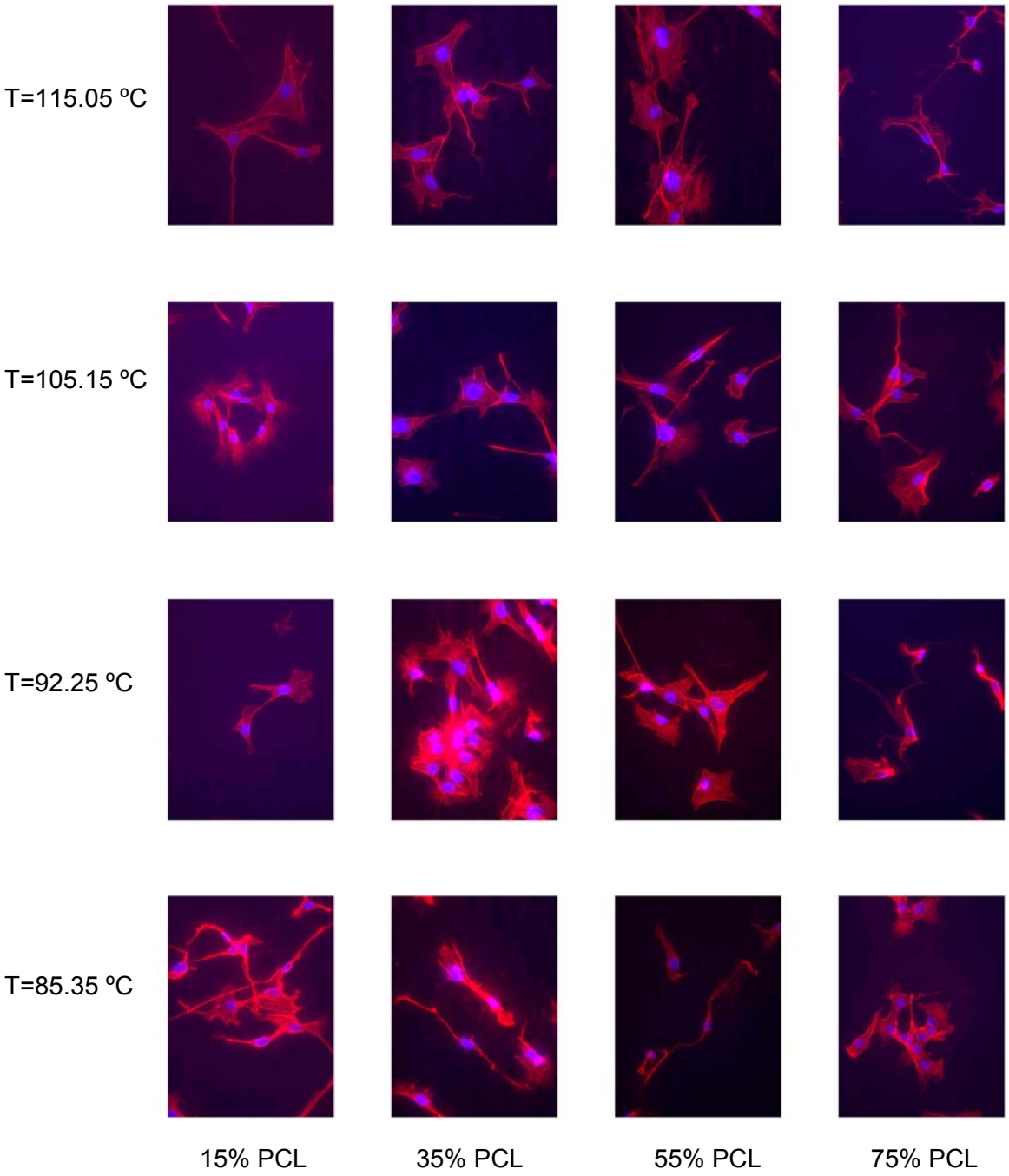

Figure 4.9. Cytoskeleton organization and predominant morphologies of MC3T3-E1 immature osteoblasts at different composition/temperature regimes over PCL/PDLA combinatorial libraries (6-hour culture). Cells were stained with rhodamine phalloidin for F-actin stress fibers (red), and Hoechst for DNA (blue). Original magnification 40x.

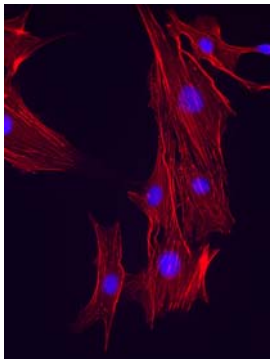

Figure 4.10. Positive control for attachment and morphology assays. F-actin: red, nucleus: blue. 6-hour culture on TCPS. Original magnification 40x.

Although well spread cells seemed to be predominant inside the LCST regime and elongated bipolar cells outside it, as previously mentioned, examples of both morphologies were present all over the library surface. Thus average cell aspect was calculated by circularity (equation 4.1) to quantify cell spreading as a function of composition and process temperature. Cell circularity compares cell aspect (the ratio of its area to the square of its perimeter) to that of a circle of the same area.

$$C = 4\pi\left[\frac{A}{P^2}\right] \tag{4.1}$$

Where *A* and *P* are the cell area and perimeter respectively. A circularity value of 1 indicates a perfect circle. As the value approaches to 0, it indicates an increasingly elongated profile.

Cell circularity was measured by image analysis using ImageJ (NIH, public domain). The procedure followed was very straightforward as it only required delimiting the cell boundary (figure 4.11). Once cell boundaries were defined, circularity calculation was performed using the built-in circularity measurement function of ImageJ.

Figure 4.11. Cell boundary outline by polygonal selection using segmented line sections (yellow line surrounding the cell marked with the arrow. Line sections are delimited by the white dots on the boundary).

A circularity value of 1 could be seen as an indicator of maximum spreading; however, well spread cells normally present polygonal processes that give them a "star-like" appearance rather than a circular shape. Circularity of spread morphologies ranges between 0.4 and 0.6, while for bipolar-shaped cells ranges between 0.08 and 0.2.

Figure 4.12 shows the average circularity values of measurements performed over 5 distinct combinatorial libraries (standard errors of the measurements are shown in figure 4.13). It is clear that spreading is enhanced in the LCST regime compared to the 1-phase region. However, this increase in cell spreading is not general to the entire 2-phase region as circularity is particularly high (0.4 to 0.47) towards the center (region between 95 to 100 ºC and 30 to 40% PCL), and a gradual decline is evinced towards the upper and lower areas (high and low temperature regions of the LCST regime), where

circularity reaches values as low as 0.24 and 0.16 respectively. This suggests that the polymer demixing level elicits perceptible changes in cell morphology.

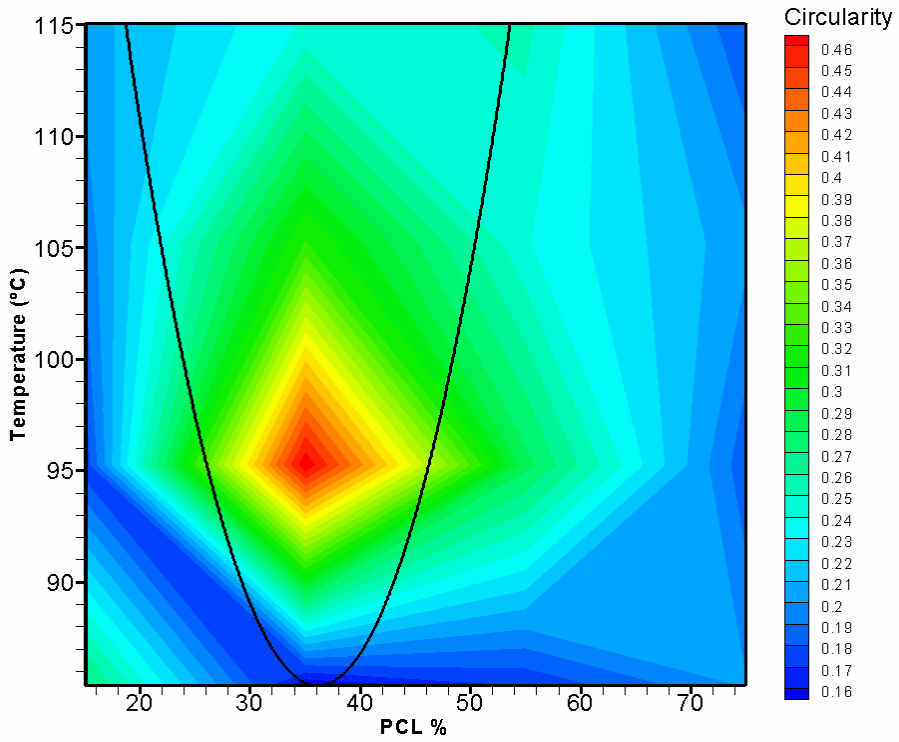

Figure 4.12. Contour map of average circularity values of MC3T3-E1 cells cultured for 6 hours over 5 distinct combinatorial libraries.

The preferential adhesion of MC3T3-E1 osteoblasts to more hydrophilic PDLA-rich domains and the marked influence of surface topography on cell morphology and cytoskeletal organization, suggest that there is an optimal size and distribution of surface microstructures that promote cell spreading. Based on the influence of patterned surfaces on cytoskeletal organization and the response of the cytoskeleton to stress conditions seen in other cell lines in previous studies [34, 36, 55], we hypothesize that the stress levels generated as cells are forced to stretch over PDLA domains promote cell multipolar spreading and production of f-actin stress fibers. In fact, the region between 95 to 100 ºC and 30 to 40% PCL, corresponding to a PCL domain diameter of

20.11 to 40.29 μm, and surface roughness of 113 to 177 nm; showed 16.9 to 37.4 % improved cell spreading (circularity range: 0.4 to 0.47) when compared to standard TCPS (average circularity: 0.342).

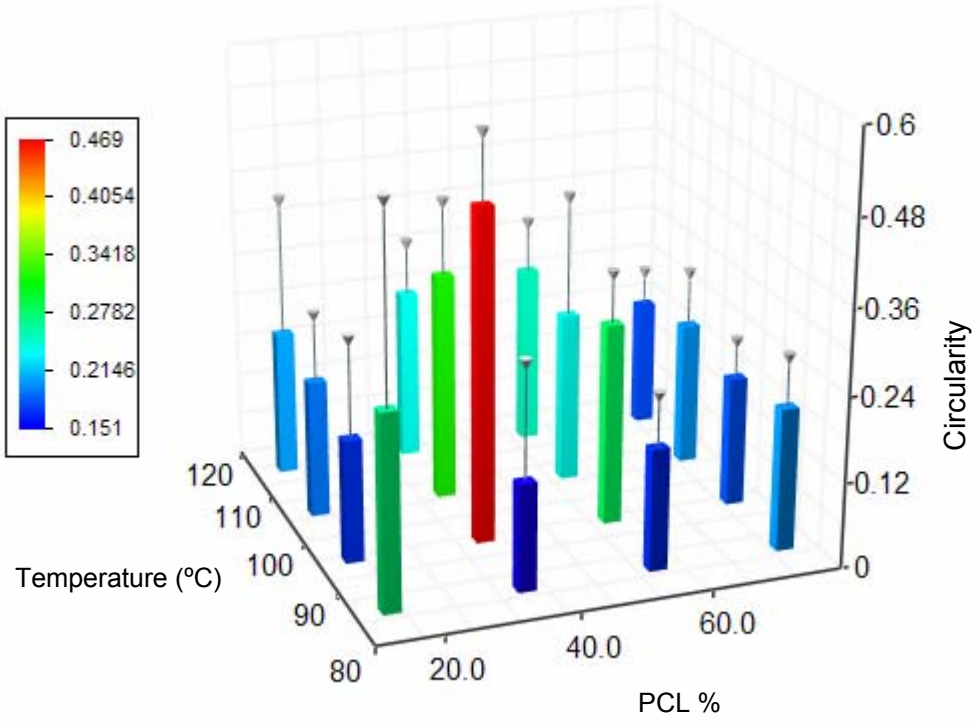

Figure 4.13. Circularity of MC3T3-E1 cells cultured over PCL/PDLA combinatorial libraries for 6 hours. Values presented as averages ± SEM, n=5. SEM is represented by inverted cone marker error bars.

Nevertheless, it has to be brought up that stellate shape and well spread morphology *do not* necessarily imply a positive influence on cell events such as differentiation and phenotypic expression. For example, Ben-Ze'ev and coworkers [56], found that hepatocytes with well spread shapes expressed low levels of mRNAs for liver-specific proteins, whereas, when seeded over a different surface, this hepatocyte cell line presented high levels of liver-specific proteins regardless of a small spherical shape with nonexistent polygonal processes and reduced cytoskeletal mRNAs

expression. Consequently, to determine if the increased production of f-actin and enhanced cell spreading witnessed in the middle section of the LCST regime is beneficial or not, although cells of the 3T3 line rarely proliferate when poorly attached [6], cell functionality has to be examined by evaluating the sequential expression of osteoblast characteristics as a function of composition and process temperature of the combinatorial libraries, followed by comparison of regions with proper or enhanced functionality with attachment and spreading-enhancing regimes.

4.3.2. PROLIFERATION

Cell proliferation was assayed at different stages of the osteoblastic development since progenitor cell proliferation and osteoblast differentiation are believed to have an approximately inverse relationship (as seen in figure 4.1). Hence proliferation of MC3T3-E1 immature osteoblasts is expected to diminish as they start to differentiate.

Assays were completed after 3, 4, 5, 8 and 13 days of culturing to encompass all the phases of the MC3T3-E1 developmental process, including the main initial proliferative stage as well as the earlier and later phases of phenotype expression. The method is based on the immunostaining of the thymidine analog BrdU that is incorporated into the DNA as it is replicated during the S-phase of the cell cycle.

After the staining procedure, due to the large number of libraries involved in the proliferation tests, the whole surface of the samples was scanned using a fluorescence phosphor-imager (Amersham Bioscience) to accelerate the discovery of areas of localized cell proliferation. These areas were imaged in detail later using a fluorescence microscope. The phosphor-imager was modified previously to read emission wavelengths between 500 and 530 nm (the peak emission wavelength of the anti-BrdU

secondary antibody, Alexa Fluor® 488, is 519 nm). Some of the complete-surface scans of BrdU stained combinatorial libraries are shown in figure 4.14.

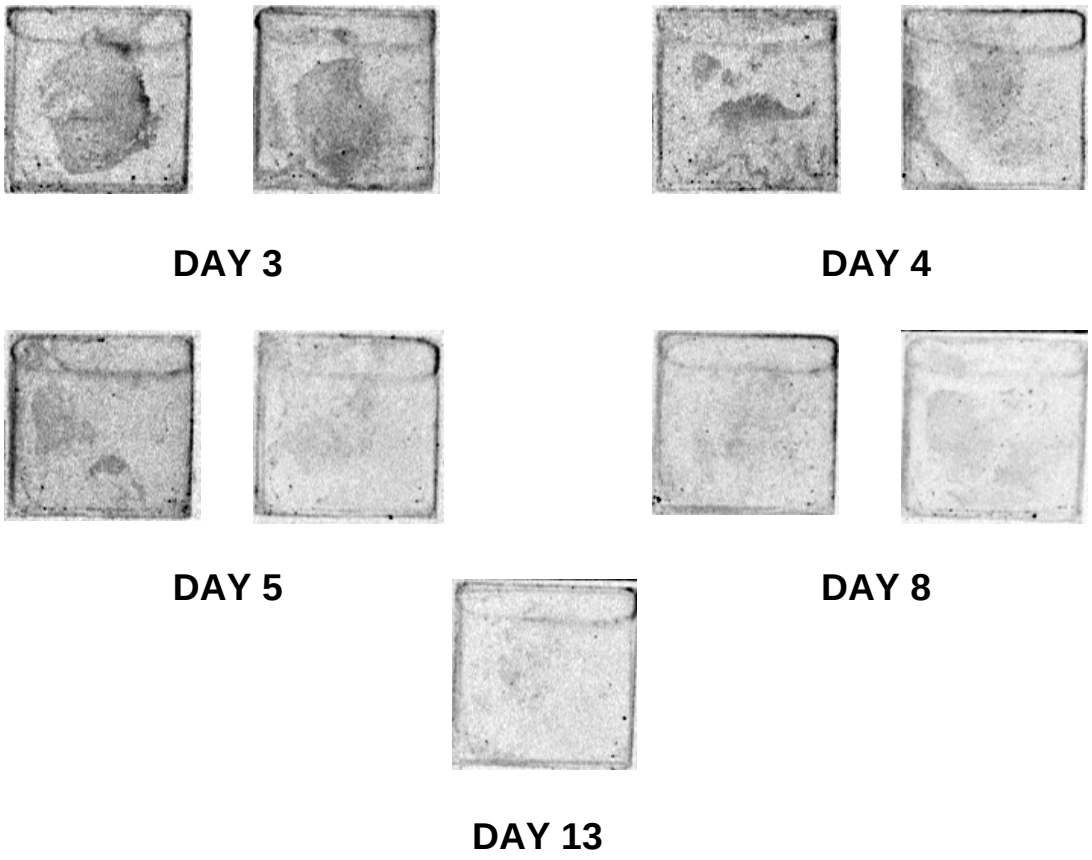

Figure 4.14. Phosphor-imager scans of the surface of PCL/PDLA combinatorial libraries cultured with MC3T3-E1 cells and immunostained for BrdU (proliferation assay). Darker regions correspond to areas of possible high cell proliferation rate (higher emission levels in the 500-530 nm wavelength range).

One of the main concerns when using the modified phosphor-imager was that the green channel signal-to-noise ratio was very low, especially for sources with weak emission power such as the immunostained libraries. This, combined with the autofluorescence of the libraries, was thought to be the reason for the patterns seen in figure 4.14, as there is no discernible similarity between samples of the same day (this behavior held for all the scans done with the phosphor-imager). A closer inspection

using the fluorescence microscope revealed that in fact the problem was dye leakage. Non-specific dye leakage is a common problem of immunostaining procedures that is influenced by diverse factors (i.e., pH, surface charge, temperature, etc). The leakage half-life of a dye may range from several weeks (i.e., carboxifluorescein in liposomes) to less than a minute (i.e., fluorescein in *Bacillus acidocaldarius*), depending on the aforementioned factors [57].

Leakage of the conjugated secondary antibody seemed to be associated with the complete membrane removal and DNA denaturation with 2N HCl, as very low leakage levels were noticed during initial tests where cells were permeabilized with detergent solutions and DNA denaturation was done by UV photolysis. Moreover, little leakage was observed when using the same secondary antibody to stain vinculin during attachment tests.

Due to the impossibility of taking advantage of the complete-surface scans obtained with the phosphor-imager, libraries were scanned the “old fashion” way using a fluorescence microscope. It is important to notice that even though the totality of the surface of each library was scrutinized, not all the areas were “readable” as green background due to leakage reached levels that completely shrouded proliferated cells from non-proliferated ones. Other sections presented reduced background intensity that allowed discrimination of proliferated and non-proliferated cells; however, hardware and control limitations (resolution and gain and exposure controls) of the camera coupled to the microscope precluded the possibility of obtaining clear images. For these regions cell count to determine the ratio of proliferated cells to total number of cells was carried out directly in the microscope.

Figure 4.15 shows fluorescence images of several positions over a combinatorial library stained for proliferation (BrdU incorporation + EthD-2 DNA staining) after a 3-day

culture. The color intensity of the images was enhanced using Photoshop (Adobe Systems, Inc.) image editing software to lessen the background levels.

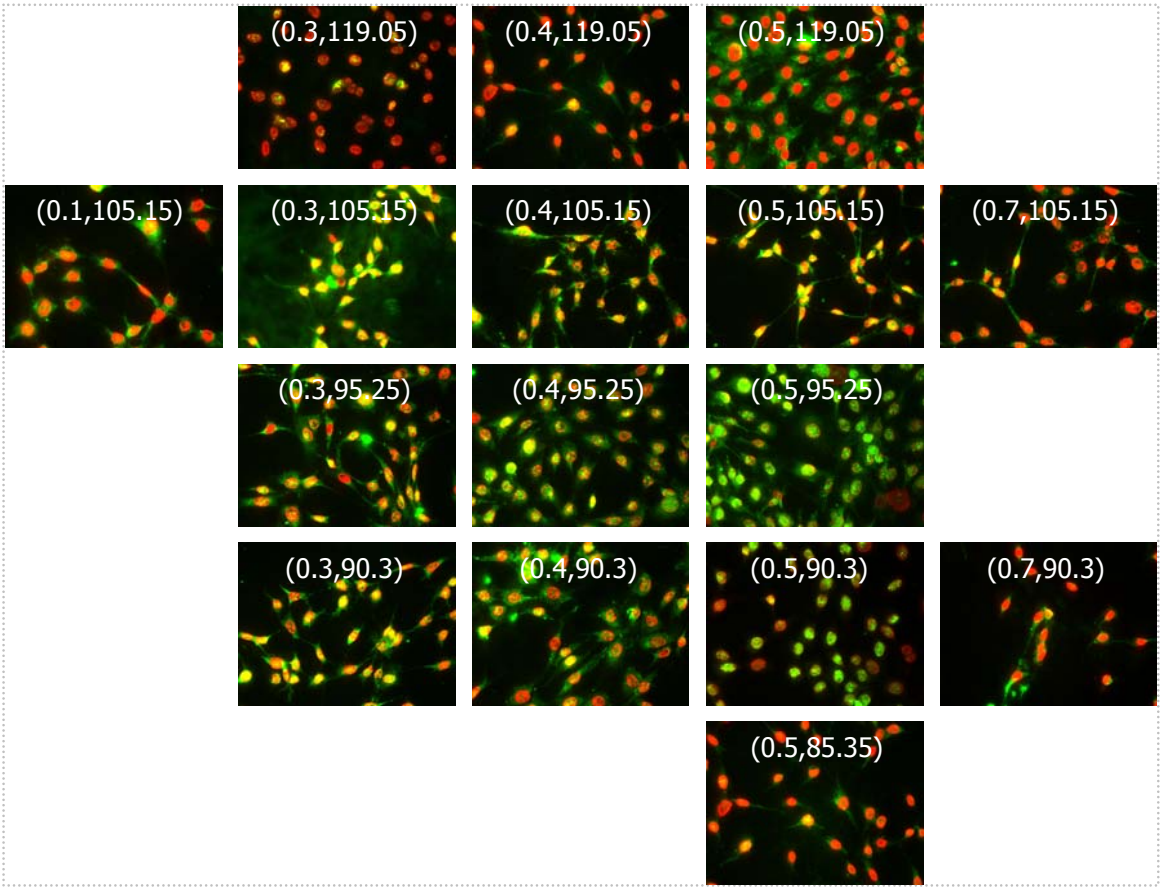

Figure 4.15. Immunofluorescence staining for proliferation of MC3T3-E1 osteoblasts over a PCL/PDLA combinatorial library after a 3-day culture. Cells were stained with Alexa Fluor® 488 (green) for BrdU incorporated into proliferated cells, and EthD-2 (red) to quantify total number of cells. Numbers in parenthesis indicate PCL mass fraction and temperature in ºC. Cell passage 5. Original magnification 40x.

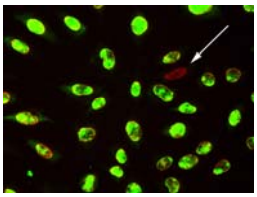

Figure 4.16. TCPS positive control for the 3-day proliferation assay. Proliferated cells: green. Arrows indicate non-proliferated cells (stained only with EThD-2). Original magnification 40x.

At a glance, effectuating a qualitative comparison of the proliferation levels of the multiple library locations shown in figure 4.15 with the degree of proliferation observed in the 3-day positive TCPS control (figure 4.16), it is readily seen that MC3T3-E1 proliferation appears to reach a standard level (TCPS level) in the outside region adjacent to the lower right side of the LCST cloud point boundary (ϕ_{PCL} = 0.5 and 90.3 ºC < T < 95.25 ºC). Hence the effect of surface microstructures on different cell events is likely to be dissimilar, as cells tend to preferentially attach and spread inside the 2-phase regime, while seem to propagate faster in the transition region between the demixed and continuous regimes. Proper quantitative analysis to support or contradict the previous statement is shown later in this section.

Negative controls were prepared following the procedure described in the methods section to rule out abnormal staining of non-proliferated cells, due to non-specific binding of primary and/or secondary antibodies, or high BrdU concentration. Figure 4.17 displays proliferation negative controls following 3-day and 4-day cultures. Contrast between green filter images of negative and positive controls confirmed that no BrdU was incorporated into non-proliferated cells, validating the assay protocol.

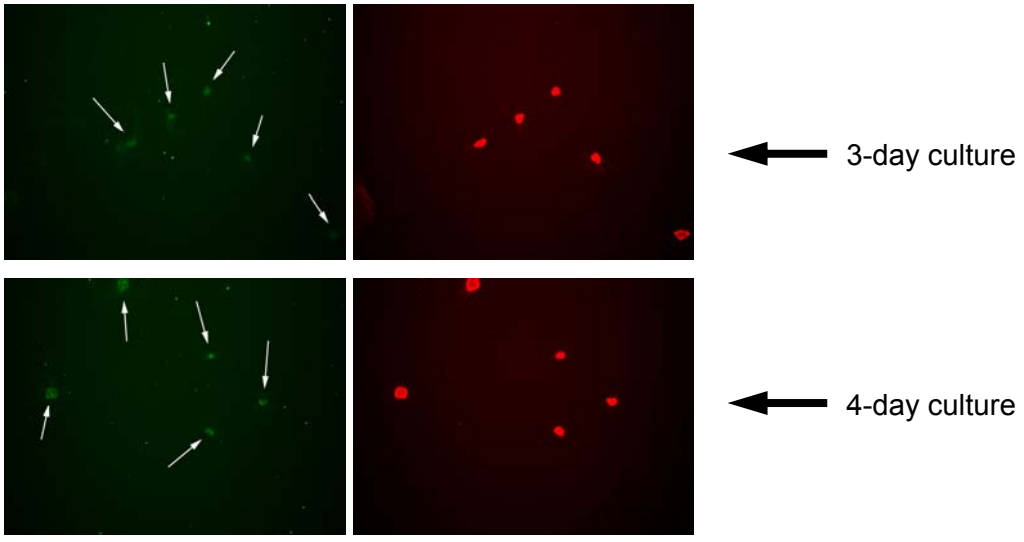

Figure 4.17. 3-day and 4-day negative control cultures for proliferation assays. Arrows in the green filter images indicate the positions of cells as seen by EthD-2 staining (red filter images). Original magnification 40x.

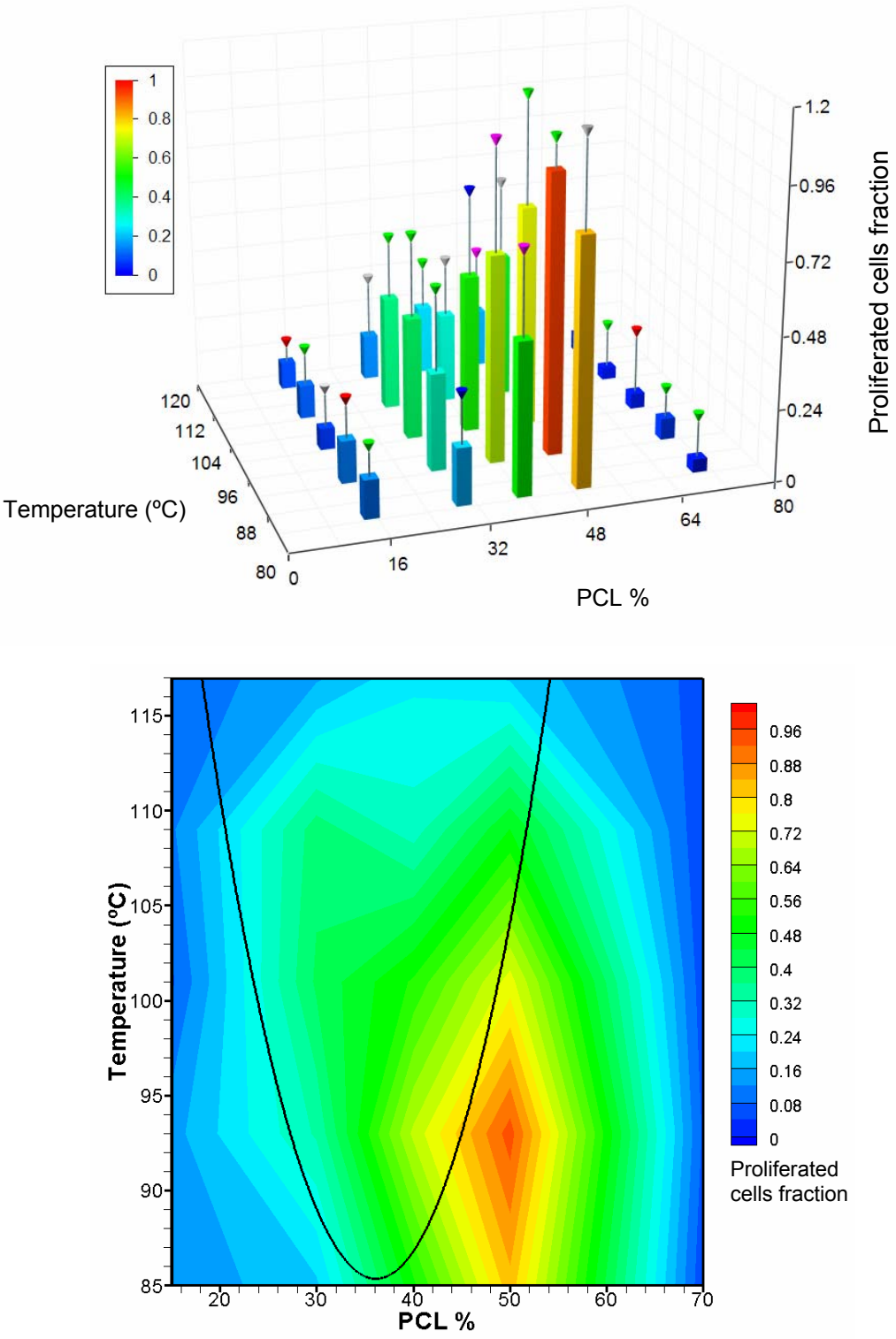

Figure 4.18. Top: Proliferated to total number of cells ratio over a combinatorial PCL/PDLA library as a function of temperature and composition after a 3-day culture (cell passage 5). Values presented as averages ± SEM (n=6 blue mark, n=5 grey mark, n=4 green mark, n=3 violet mark, n=2 red mark). Bottom: Average proliferation ratio contour map.

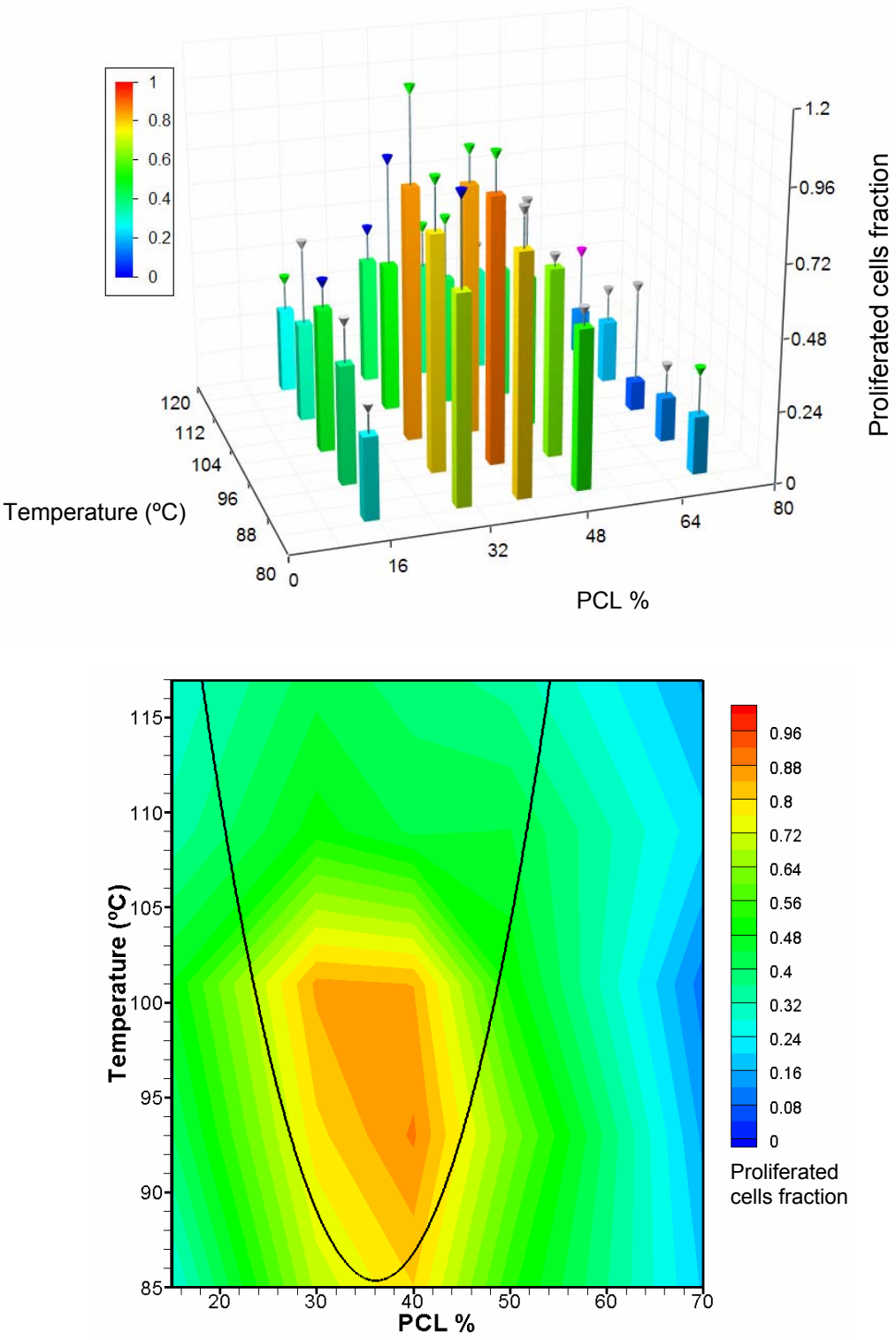

Figure 4.19. Top: Proliferated to total number of cells ratio over a combinatorial PCL/PDLA library as a function of temperature and composition after a 4-day culture (cell passage 7). Values presented as averages ± SEM (n=6 blue mark, n=5 grey mark, n=4 green mark, n=3 violet mark). Bottom: Average proliferation ratio contour map.

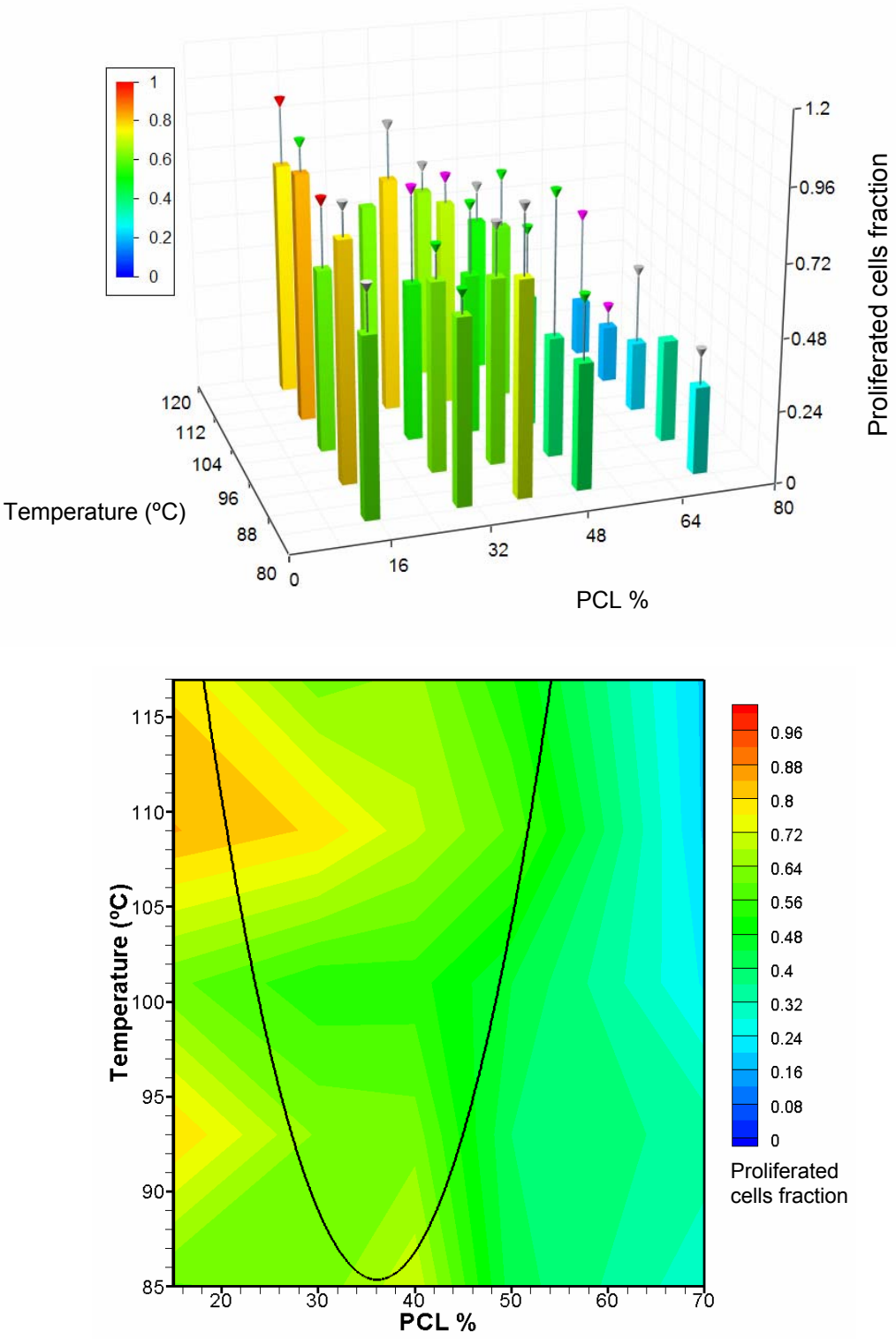

Figure 4.20. Top: Proliferated to total number of cells ratio over a combinatorial PCL/PDLA library as a function of temperature and composition after a 5-day culture (cell passage 4). Values presented as averages ± SEM (n=5 grey mark, n=4 green mark, n=3 violet mark, n=2 red mark, n=1 no mark). Bottom: Average proliferation ratio contour map.

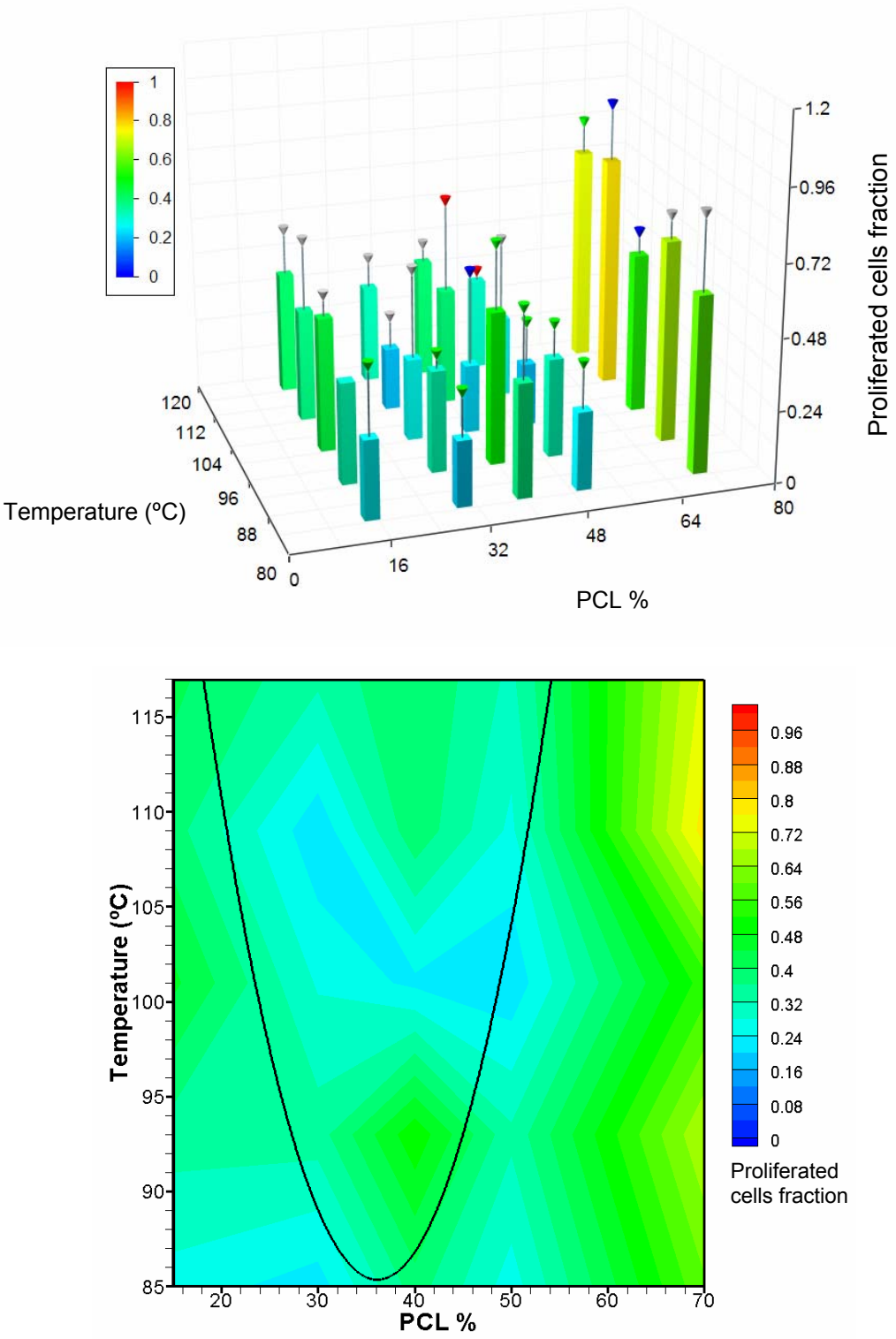

Figure 4.21. Top: Proliferated to total number of cells ratio over a combinatorial PCL/PDLA library as a function of temperature and composition after a 8-day culture (cell passage 4). Values presented as averages ± SEM (n=6 blue mark, n=5 grey mark, n=4 green mark, n=2 red mark, n=1 no mark). Bottom: Average proliferation ratio contour map.

The ratio of proliferated cells to total number of cells at diverse locations of the combinatorial libraries is shown in figures 4.18 through 4.22. Average values ± standard error means are shown in bar plots, while contour maps present 2D views of the average values to ease data visualization. Due to the fact that not all the areas of each of the 6 libraries used per assay were 100% readable, as stated before, the value of n (number of samples) required for the estimation of the standard error fluctuates within each assay. Error bars were marked accordingly by assigning a different color to each value of n. Finally, it is important to notice that the lower and higher limits of the proliferation ratio in the bar plots and contour maps, represented by multiple color levels, were kept *constant* for all the assays to have a proper visualization of the intensity of proliferation across the libraries.

An interesting trend in MC3T3-E1 proliferation over combinatorial libraries is witnessed after a 3-day culture (figure 4.18), since cells seem to have a higher proliferation rate on the polymer surface nearby the lower limit of the phase separated region. This area, characterized by small to medium diameter PCL domains (approximately 21 to 33 μm) and moderate roughness (85 to 105 nm), presented a remarkably poor cell spreading and cytoskeletal organization upon initial attachment (0.18 to 0.28 circ.). Hence, our belief was that proliferation would not be enhanced in this region, especially due to the fact that replication of the 3T3 cell line is precluded by poor cell spreading [6]. However, the results seen, which corroborate the initial qualitative deduction, suggest that the enhanced spreading in the middle-lower part of the LCST, resulting from a response to surface topography as the cell tries to reach the preferred PDLA-rich domains to attach and avoid apoptosis via anoikis, is not necessarily beneficial for cell proliferation and differentiation. A possible explanation for this behavior is a lack of *isometric* tension in the cytoskeleton of the well-spread morphologies attained inside the LCST regime. For example, preventing the development of isometric

tension and subsequent cytoskeletal restructuring events has been shown to delay, or even inhibit, the progression of the G1 phase of the cell cycle in human capillary endothelial cells, leading to a restriction of cell proliferation [23]. Other studies have demonstrated that entering the S phase of the cell cycle and DNA synthesis can only proceed when cells are spread to the *appropriate* degree [14].

A behavior similar to the one observed in figure 4.18 has been seen before in studies carried out with immortalized human fibroblasts [34], where following initial attachment cells presented stellate morphologies and well organized cytoskeletons over rough surfaces, whereas, cells attached to flat surfaces had less f-actin stress fibers and elongated shapes. 3 days after the initial culture trends had reversed, and the cytoskeleton on the planar surface matured with increased amounts of organized f-actin fibers, while the cytoskeleton of cells over rough surfaces had become less organized. The trend continued, and after 3 weeks cells over the flat surface were mostly confluent, whereas the cells over the rough surface were still single, while keeping their well spread morphology. Furthermore, various similar studies have revealed a negative impact of increased roughness above a particular threshold on cell growth. Washburn et al [58], for example, have shown that there is a critical roughness value above which proliferation of MC3T3-E1 osteoblasts is drastically reduced. Other study revealed that proliferation of rat calvarial cells respond to increased roughness up to a point where further increase result in detrimental of cell proliferation [29].

No strengthening of proliferation was noticed in any area of the combinatorial library when compared to the TCPS positive control. The highest level of proliferation over the libraries was comparable to that of the positive control.

It is important to notice that the lack of growth response in certain areas of the library was not due to reduced viability, since no apoptosis was observed (section

4.3.4.). On the contrary, as shown in the subsequent paragraphs, it was a direct effect of the surface of the combinatorial library.

After 4 days in culture (figure 4.19) the high MC3T3-E1 proliferation regime shifted to the lower portion inside the 2-phase region. A small increase in cell proliferation was also evinced in the high PDLA concentration region (left area outside the LCST) as well as the upper part of the LCST regime. The high PCL concentration region, on the other hand, kept low proliferation levels even though that in the 3-day culture assay exhibited proliferation levels comparable to the 2 regions just mentioned. This can be attributed to the lower surface energy of the high PCL concentration region , since increasing hydrophobicity seems to appreciably reduce cell proliferation [16]. There is also a reduction in proliferation in the area with the highest levels of cell replication in the 3-day assay. This seems to be in agreement with the downregulation of proliferation as cell density increases prior to differentiation.

Results of the 5-day proliferation assay are shown in figure 4.20. At this point proliferation is prominent only in some areas of the high PDLA concentration region and the upper left portion of the LCST (proliferation ratio ~0.7). The rest of the library, with the exception of the high PCL concentration domain, seems to be leveling and lowering the cell replication rate as cells are almost confluent (proliferation ratio ~0.4). The Effect of the diverse topographies across the library on cell proliferation can be seen from the sequence of different positions where the area of maximum proliferation was located in every test, namely, a transition region with low roughness and moderate to small microstructures just outside the LCST regime at day 3, middle and lower parts of the 2 phase regime at day 4, and upper part of the phase separated region at day 5.

Proliferation ratios of approximately 0.28 at high PCL concentrations (5-day assay) reinforce the hypothesis that surface energy is critical for cell proliferation. At this

point the cell proliferation ratio of the positive control is lower than the maximum one over the library since the control is almost confluent (proliferation downregulation).

The 8-day assay (figure 4.12) showed an upsurge in the proliferation ratio at high concentrations of PCL. This increase in cell growth in the most hydrophobic area of the library, after a prolonged cell culture (8 days), suggests that cell proliferation is retarded by low energy substrata. On the other hand, the rest of the library was almost confluent and exhibited signs of strong downregulation of proliferation which are characteristic of the onset of mineralization.

After 13 days proliferation has leveled out and the totality of the surface of each library is confluent. Only negligible cell growth activity is witnessed at random locations of the libraries indicating the total inhibition of proliferation and, hence, the existence of a mature osteoblast phenotype. This however has to be supported by evaluating the levels of expression of osteoblast markers.

4.3.3. PROTEIN EXPRESSION AND MINERALIZATION

Phenotypic characterization was carried out at diverse instances of the postproliferative phase of MC3T3-E1 cells to asses the effect of combinatorial libraries on cell differentiation. Two different markers were examined, namely, alkaline phosphatase (ALP) and bone osteocalcin (OCN).

Initial work done by Meredith et al [37] over PCL/PDLA combinatorial libraries showed that alkaline phosphatase expression was strongly enhanced at a particular temperature-composition regime of the libraries when compared to standard TCPS (figure 4.22). In this work alkaline phosphatase activity of MC3T3-E1 cells, which normally increases immediately after the proliferative period [40], was assayed after 7

and 8 days of culture. 6 separate libraries were examined in each test following the procedure outlined in the methods section.

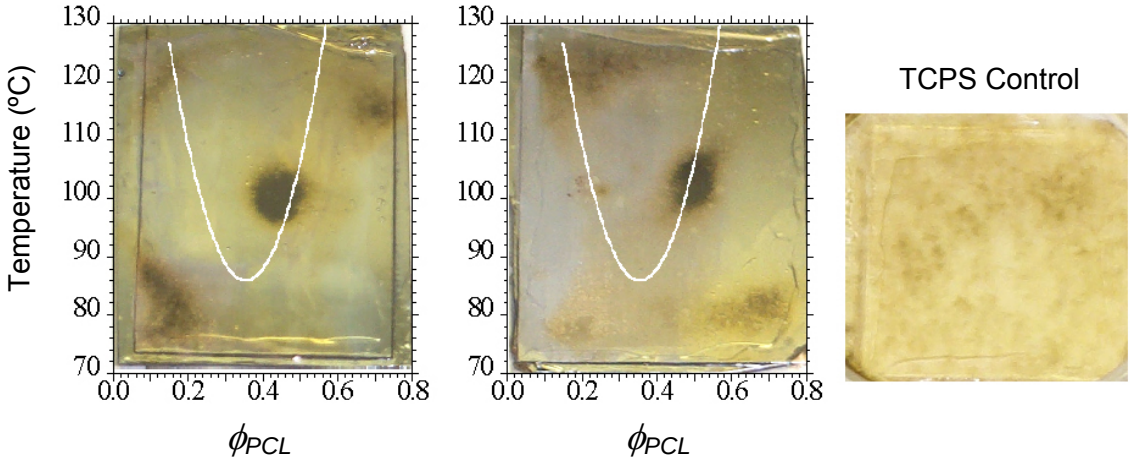

Figure 4.22. Alkaline phosphatase stained PCL/PDLA combinatorial libraries after 5-day culture with MC3T3-E1 cells (TCPS control is shown on the right). Dark areas near the LCST cloud point boundary correspond to alkaline phosphatase enhancing regimes [37].

Figure 4.23 shows a digital scan of one of the alkaline phosphatase stained libraries alongside a TCPS positive control following a 7-day culture.

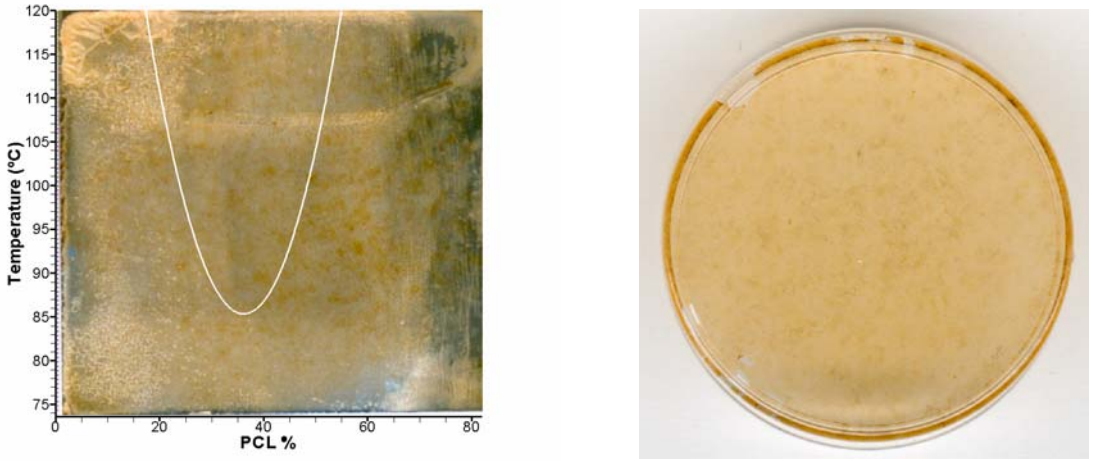

Figure 4.23. Left: Combinatorial PCL/PDLA library stained for alkaline phosphatase after a 7-day culture with MC3T3-E1 cells (the white line represents the LCST boundary). Right: Positive control TCPS. Cell passage 6.

It is readily seen that the level of alkaline phophatase expression is very low on both the combinatorial library and the positive TCPS control, with no discernible differences between both. It is also noticed that there are no important differences between the continuous phase regime and the 2-phase regime inside the LCST, suggesting no effect of the surface topography on cell differentiation. However, the work of Meredith and coworkers shows that actually surface properties *do* influence cell differentiation. Moreover, their alkaline phosphatase test was done over a 5-day culture. At this early time, under standard culturing conditions, alkaline phosphatase is expressed in very low levels by pre-osteoblasts [41], hence their results can only be explained by an upregulation of gene expression triggered by the surface properties of a particular area on the combinatorial library.

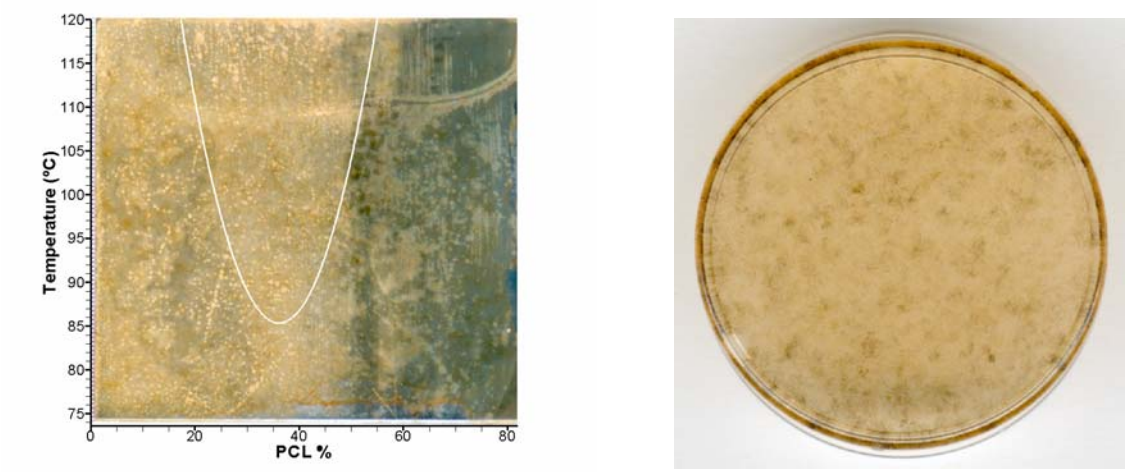

Figure 4.24. Left: Combinatorial PCL/PDLA library stained for alkaline phosphatase after a 8-day culture with MC3T3-E1 cells (the white line represents the LCST boundary). Right: Positive control TCPS. Cell passage 6.

Results of the alkaline phosphatase activity assay for a 8-day culture were not very different from those of the obtained on the 7-day ones. Figure 4.24 shows that ALP expression increased a little on the positive control (which now looks similar to the control of Meredith et al), whereas the library remained almost unchanged. Initially we

thought that the library was somehow inhibiting the cell transcriptional pathways that lead to differentiation; however, ALP levels on the positive control were also abnormally low for an 8-day culture. Therefore we hypothesize that something related to the culturing procedure and/or culturing materials (i.e., media, serum, etc) is retarding or inhibiting cell differentiation.

An extra alkaline phosphatase test run performed on a 9-day culture showed an increased amount of ALP on matured ECM nodules (figure 4.25). However, again, ALP expression was slightly higher on the positive control than on the library, and there was no discernible difference between inside and outside of the LCST regime. Moreover, as seen in the proliferation assays (figure 4.21), the proliferative stage came to an end around day 8. This transition to the matrix deposition and maturation phase is characterized by a manifest upsurge in alkaline phosphatase expression [40]. Therefore, the expressed levels of ALP at day 9 were expected to be *significantly* higher in comparison to the previous two tests.

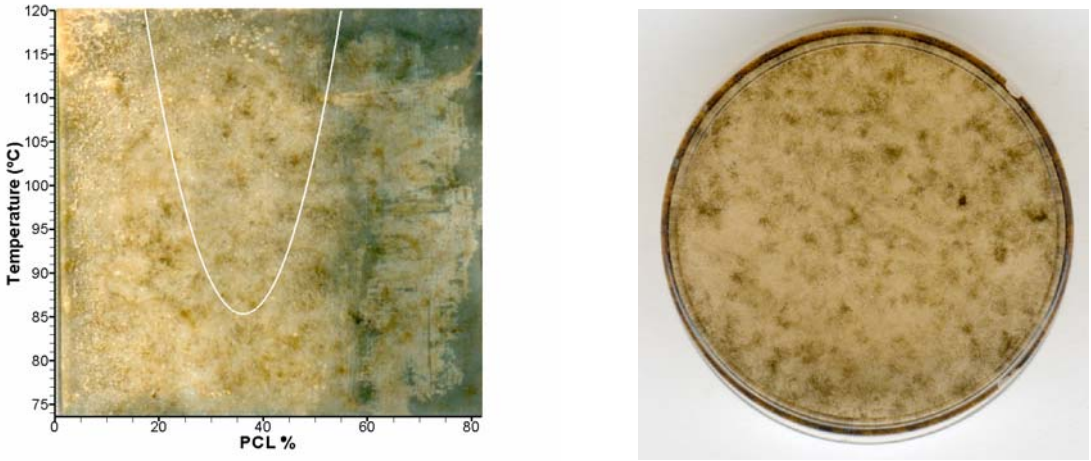

Figure 4.25. Left: Combinatorial PCL/PDLA library stained for alkaline phosphatase after a 9-day culture with MC3T3-E1 cells (the white line represents the LCST boundary). Right: Positive control TCPS. Cell passage 5.

Mineralization tests of 13 and 14-day cultures were performed by Von Kossa staining as mentioned in the methods section. Figure 4.26 shows digital scans of a 14-day Von Kossa stained library and a positive TCPS control. The samples in the image are characterized by the presence of a thick collagen layer and a *total absence* of mineralized nodules in *both* the positive control and the combinatorial library. This suggests that the library's surface is not responsible for the lack or reduced phenotypic expression witnessed during the alkaline phosphatase tests, and corroborates the hypothesis that MC3T3-E1 differentiation is being retarded or inhibited by either the culturing procedure or the culturing materials.

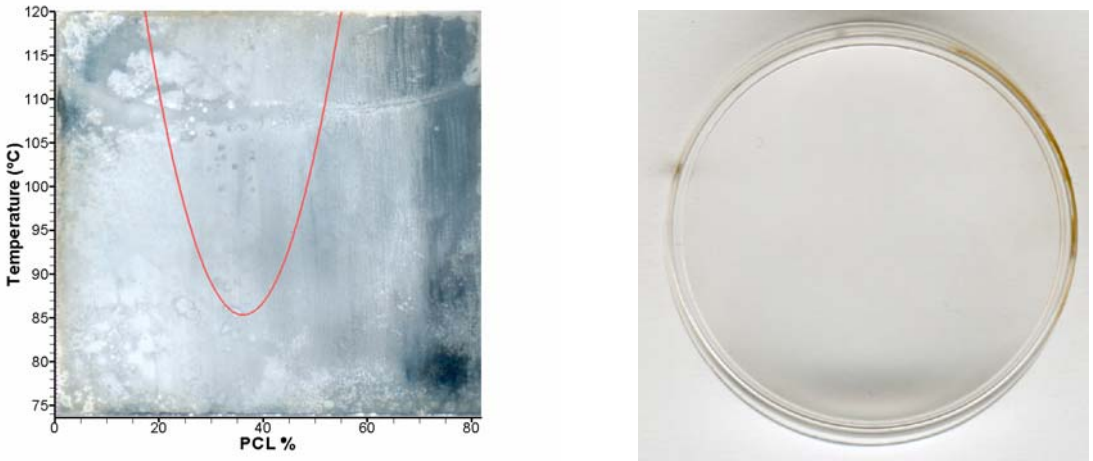

Figure 4.26. Von Kossa stain for MC3T3-E1 mineralization after a 14-day culture. Left: Combinatorial PCL/PDLA library (the red line represents the LCST cloud point boundary). Right: Positive control TCPS. Cell passage 4.

During the time the experiments for this work were performed, other researchers in the laboratory that were working with the same cell line had mineralization issues, namely, lack of mineralized nodules even after 21-day runs. The problem was tracked down to be related with the serum used to supplement the media. This is not a unusual problem, and has been extensively documented. For example, Cornet et al [59] showed

that rabbit bone marrow stromal cells differentiated and exhibited ALP activity when supplemented with fetal calf serum, but fail to express ALP and revealed reduced amounts of cell differentiation when supplemented with Ultroser® serum.

As expected, after the results shown above, the outcome of the tests for the late marker “bone osteocalcin” was negative as well.

Some libraries, as the ones shown in figure 4.27, exhibited very small levels of dystrophic mineralization. What is interesting is that this mineralization took place mainly in the middle-upper part of the phase separated regime. However, if this effect is induced by the phase morphology of the surface or if it is just a random effect is unknown. Another peculiarity that was noticed in all the libraries stained for mineralization is that collagen deposition was almost non-existent in the high PCL concentration sector (see figures 4.26 and 4.27). This can be a sign of the existence of a strong effect, previously seen in cell attachment and proliferation, of PCL on extracellular matrix deposition.

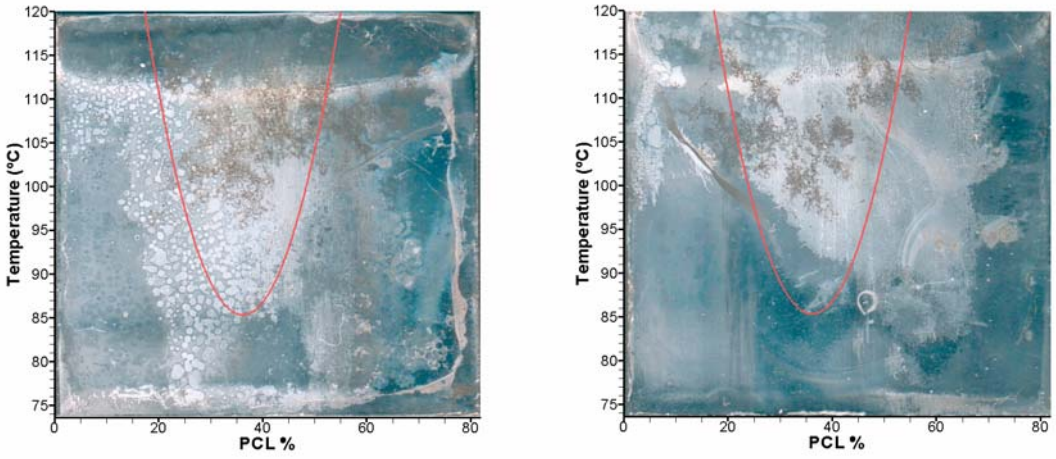

Figure 4.27. Von Kossa stain for MC3T3-E1 mineralization over combinatorial libraries after a 14-day culture (the red line represents the LCST cloud point boundary). Cell passage 4.

Further work to properly assay osteoblast phenotypic expression of MC3T3-E1 cells over combinatorial libraries is planned after materials (i.e., serum) are accurately screened, tested, and validated using standard culture techniques.

4.3.4. CELL VIABILITY

Cell viability didn't show any direct relation with the surface characteristics of the libraries, as it ranged between 98.5% and 100% across the library's surface during all tests. Increased amount of dead cells was noticed only at the borders of the libraries during the 13-day and 14-day assays (confluent cells), as shown in figure 4.28.

The combined viability of all the experiments performed was 98.13 % ± 0.91 (n=64).

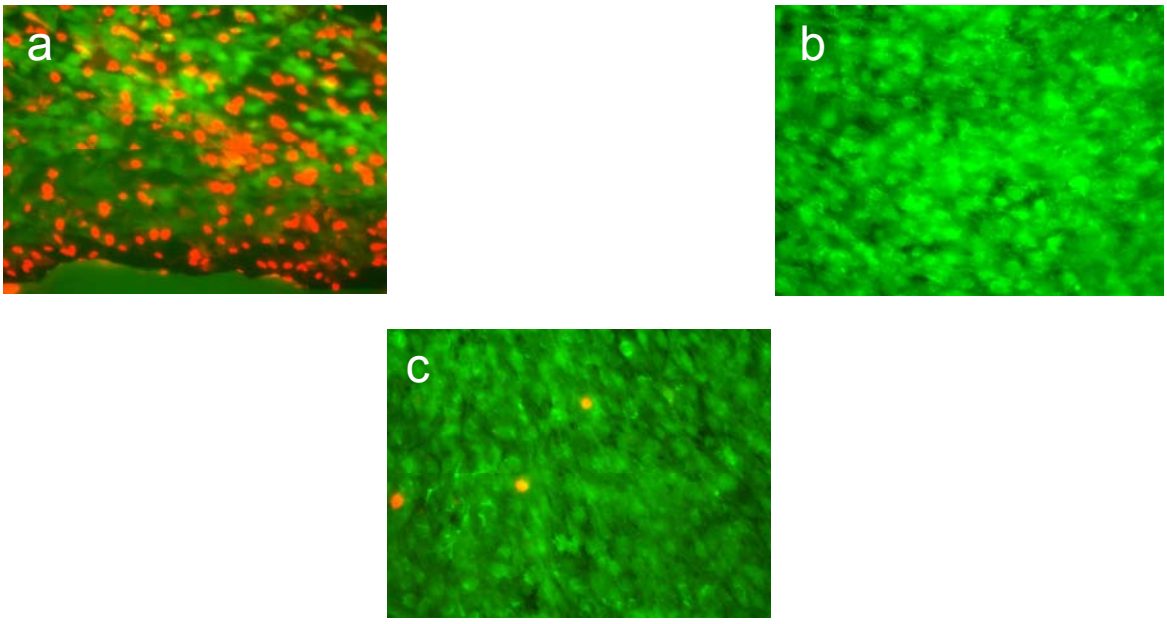

Figure 4.28. Viability comparison of different regions over totally confluent PCL/PDLA combinatorial libraries. a) 14-day test, lower border of the library. b) 13-day test, middle region of the library. c) 14-day test, middle region of the library. Viable cells: Green (stained with calcein AM), dead cells: Red (stained with EthD-1).

4.4. SUMMARY

Combinatorial libraries of PCL/PDLA with diverse surface morphologies were used to assay the influence of surface structure on different cell events of MC3T3-E1 mouse immature osteoblasts, namely, attachment, spreading, proliferation, and differentiation.

Initial cell attachment took place preferentially over the more hydrophilic PDLA regardless of the distinct surface structures present inside the LCST regime. On the other hand, although cells presented pleomorphic forms all over the library, cell spreading was influenced by surface microstructures. Bipolar elongated shapes were predominant outside the phase-separated region, while multipolar stellate shapes were present mainly inside the LCST regime, especially in the region between 93 to 100 ºC and 30 to 40 % PCL, which corresponds to a surface roughness interval of 113 nm < R_{RMS} < 177 nm and a PCL domain size range of 20.11 μm < d_{PCL} < 40.29 μm, where circularity values reached maximum levels.

Cell proliferation was initially (3-day culture) enhanced in the transition region between the LCST regime and the continuous phase (area comprised between 85 to 100 ºC and 45 to 55% PCL) corresponding to intervals of surface roughness of 85 nm < R_{RMS} < 105 nm and PCL domain size of 21 μm < d_{PCL} < 33 μm. As time passed the area of enhanced proliferation shifted across the library: lower region inside the LCST regime at day 4, PDLA-rich continuous region outside the LCST boundary at day 5, and PCL-rich regime on the right hand side of the library at day 8. At day 13 proliferation was suppressed and the library was totally confluent.

Phenotypic expression assays showed that MC3T3-E1 differentiation was being retarded or inhibited by the serum used during the experiments. Hence, the effect of structure dissimilarity across the library could not be properly estimated.

Viability didn't seem to be affected by the surface morphology of the library since no apoptosis was observed in any specific region throughout all the experiments.

4.5. CONCLUSION

The observed interactions of MC3T3-E1 cells and the variable textured surface of the PCL/PDLA combinatorial libraries confirm the important role of surface morphology on cell behavior, and show the potential of combinatorial libraries for rapid identification of complex cell-surface interactions. Specifically, it is revealed that the effect induced by a particular region seems to be highly specific for each cell event, as it was clearly seen in the attachment, spreading, and proliferation assays (although the effect of surface topography on phenotypic expression couldn't be evaluated we believe that this region-cell event specificity applies for all the phases of the cell developmental process) .

This methodology for characterization of wide ranges of surface-cell responses opens a new door in biomaterial design, as new biomaterial surfaces can be engineered to target a particular cell event (i.e., proliferation, protein expression, etc) and elicit desired results.

REFERENCES

1. **Curtis A., Riehle M., *Tissue engineering: the biophysical background.* Phys. Med. Biol., 2001. 46: p. R47-R65.**

2. **Ratner B.D., Hoffman A.S., Schoen F.J., and Lemons J.E., ed. *Biomaterials Science: An introduction to materials in medicine*. 1 ed. 1996, Academic Press: San Diego, CA. 484.**

3. **Castner D.G., Ratner B.D., *Biomedical surface science: Foundations to frontiers.* Surface Science, 2002. 500: p. 28-60.**

4. **Culp L.A., *Biochemical Determinants of Cell Adhesion.* Current Topics in Membranes and Transport, 1978. 2: p. 327-396.**

5. **Burridge K., Chrzanowska-Wodnicka M., *Focal adhesions, contractility, and siganling.* Annu. Rev. Cell Dev. Biol., 1996. 12: p. 463-519.**

6. **Alberts B., Bray D., Lewis J., Raff M., Roberts K., and Watson J.D., *Molecular Biology of the Cell*. 1989, New York: Garland Publishing, Inc. 1264.**

7. **Ben-Ze'ev A., Shtutman M., and Zhurinsky J., *The Integration of Cell Adhesion with Gene Expression: The role of β-Catenin.* Experimental cell research, 2000. 261: p. 75-82.**

8. **Chicurel M.E., Singer R.H., Meyer C.J., and Ingber D.E., *Integrin binding and mechanical tension induce movement of mRNA and ribosomes to focal adhesions.* Nature, 1998. 392: p. 730-733.**

9. **Hamerli P., Weigel Th., Groth Th., and Paul D., *Surface properties and cell adhesion onto allylamine-plasma-coated polyethylenterephtalat membranes.* Biomaterials, 2003. 24: p. 3989-3999.**

10. **Yang X.B., Roach H.I., Clarke N.M.P., Howdle S.M., Quirk R., Shakesheff K.M., and Oreffo R.O.C., *Human Osteoprogenitor Growth and Differentiation on Synthetic Biodegradable Structures After Surface Modification.* Bone, 2001. 29(6): p. 523-531.**

11. **Lee J.H., Jung H.W., Kang I., and Lee H.B., *Cell Behaviour on Polymer Surfaces with Different Functional Groups.* Biomaterials, 1994. 15(9): p. 705-711.**

12. **Lampin M., Warocquier-Clerout R., Legris C.,Degrange M., and Sigot-Luizard M.F., *Correlation between substratum roughness and wettability, cell adhesion, and cell migration.* J Biomed Mater Res, 1997. 36: p. 99-108.**

13. **Spargo B.J., Testoff M.A., Nielsen T.B., Stenger D.A., Hickman J.J., and Rudolph A.S., *Spatially controlled adhesion, spreading, and differentiation***

of endothelial cell on self-assembled molecular monolayers. **Proc. Natl. Acad. Sci. USA, 1994. 91: p. 11070-11074.**

14. **Folkman J., Moscona A., *Role of cell shape in growth control.* Nature, 1978. 273: p. 345-349.**

15. **Manwaring M.E., Biran R., and Tresco P.A., *Characterization of rat meningeal cultures on materials of differing surface chemistry.* Biomaterials, 2001. 22: p. 3155-3168.**

16. **Brocchini S., James K., Tangpasuthadol V., and Kohn J., *Structure-property correlations in a combinatorial library of degradable materials.* Journal of Biomedical Materials Research, 1998. 42: p. 66-75.**

17. **Lin H.B., Zhao Z.C., García-Echeverría C., Rich D.H., and Cooper S.L., *Synthesis of a novel polyurethane copolymer containing covalently attached RGD peptide.* J Biomed Mater Res, 1991. 25: p. 223-242.**

18. **Chung T.W., Lu Y.F., Wang S.S., Lin Y.S., and Chu S.H., *Growth of human endothelial cells on photochemically grafted Gly-Arg-Gly-Asp (GRGD) chitosans.* Biomaterials, 2002. 23: p. 4803-4809.**

19. **Thomas C.H., Collier J.H., Sfeir C.S., and Healy K.E., *Engineering gene expression and protein synthesis by modulation of nuclear shape.* PNAS, 2002. 99: p. 1972-1977.**

20. **Chehroudi B., Brunette D.M., *Effects of Surface Topography on Cell Behavior*, in *Encyclopedic Handbook of Biomaterials and Bioengineering*, D.J. Wise, Altobelli D.E., Yaszenski M.J., Gresser G.D., and Schwartz E.R., Editor. 1995, Dekker: New York. p. 813-842.**

21. **Huang S., Ingber D.E., *Shape-Dependent Control of Cell Growth, Differentiation, and Apoptosis: Switching between Attractors in Cell Regulatory Networks.* Experimental cell research, 2000. 261: p. 91-103.**

22. **Chen C.S., Mrksich M., Huang S., Whitesides G.M., Ingber D.E., *Geometric control of cell life and death.* Science, 1997. 276: p. 1425-1428.**

23. **Huang S., Chen C.S., and Ingber D.E., *Control of Cyclin D1, p27^{Kip1}, and Cell Cycle Progression in Human Capillary Endothelial Cells by Cell Shape and Cytoskeletal Tension.* Molecular Biology of the Cell, 1998. 9: p. 3179-3193.**

24. **Singhvi R., Kumar A., Lopez G.P., Stephanopoulos G.N., Wang D., Whitesides G.M., and Ingber D.E., *Engineering cell shape and function.* Science, 1994. 264: p. 696-698.**

25. **Chou L., Firth J.D., Uitto V., and Brunette D.M., *Substratum surface topography alters cell shape and regulates fibronectin mRNA level, mRNA stability, secretion and assembly in human fibroblasts.* Journal of Cell Science, 1995. 108: p. 1563-1573.**

26. **Miller C., Shanks H., Witt A., Rutkowski G., and Mallapragada S., *Oriented Schwann cell growth on micropatterned biodegradable polymer substrates.* Biomaterials, 2001. 22: p. 1263-1269.**

27. **Meyle J., Gültig K., Brich M., Hämmerle H., and Nisch W., *Contact guidance of fibroblasts on biomaterial surfaces.* Journal of Materials Science: Materials in Medicine, 1994. 5: p. 463-466.**

28. **Wójciak-Stothard B., Madeja Z., Korohoda W., Curtis A., and Wilkinson C., *Activation of macrophage-like cells by multiple grooved substrata. Topographical control of cell behavior.* Cell Biology International, 1995. 19(6): p. 485-490.**

29. **Hatano K., Inoue H., Kojo T., Matsunaga T., Tsujisawa T., Uchiyama C., and Uchida Y., *Effect of surface roughness on proliferation and alkaline phosphatase expression of rat calvarial cells cultured on polystyrene.* Bone, 1999. 25(4): p. 439-445.**

30. **Boyan B.D., Batzer R., Kieswetter K., Liu Y., Cochran D.L., Szmuckler-Moncler S., Dean D.D., and Schwartz Z., *Titanium surface roughness alters responsiveness of MG63 osteoblast-like cells to 1α,25-$(OH)_2D_3$.* Journal of Biomedical Materials Research, 1998. 39: p. 77-85.**

31. **Schwartz Z., Lohmann C.H., Vocke A.K., Sylvia V.L., Cochran D.L., Dean D.D., and Boyan B.D., *Osteoblast response to titanium surface roughness and 1α,25-(OH)2D3 is mediated through the mitogen-activated protein kinase (MAPK) pathway.* Journal of Biomedical Materials Research, 2001. 56: p. 417-426.**

32. **Lohmann C.H., Sagun R., Sylvia V.L., Cochran D.L., Dean D.D., Boyan B.D., and Schwartz Z., *Surface roughness modulates the response of MG63 osteoblast-like cells to 1,25-$(OH)_2D_3$ through regulation of phospholipase A_2 activity and activation of protein kinase A.* Journal of Biomedical Materials Research, 1999. 47: p. 139-151.**

33. **Soboyejo W.O., Nemetski B., Allameh S., Marcantonio N., Mercer C., and Ricci J., *Interactions between MC3T3-E1 cells and textured Ti6Al4V surfaces.* J Biomed Mater Res, 2002. 62: p. 56-72.**

34. **Dalby M.J., Childs S., Riehle M.O., Johnstone H.J.H., Affrossman S., and Curtis A.S.G., *Fibroblast reaction to island topography: Changes in cytoskeleton and morphology with time.* Biomaterials, 2003. 24: p. 927-935.**

35. **Dalby M.J., Riehle M.O., Johnstone H.J.H., Affrossman S., and Curtis A.S.G., *In vitro reaction of endothelial cells to polymer demixed nanotopography.* Biomaterials, 2002. 23: p. 2945-2954.**

36. **Dalby M.J., Yarwood S.J., Riehle M.O., Johnstone H.J.H., Affrossman S., and Curtis A.S.G., *Increasing fibroblast response to materials using nanotopograhy: Morphological and genetic measurements of cell response***

to 13-nm-high polymer demixed islands. **Experimental cell research, 2002. 276: p. 1-9.**

37. Meredith J.C., Sormana J.L., Keselowsky B.G., García A.J., Tona A., Karim A., and Amis E.J., *Combinatorial Characterization of Cell Interactions with Polymer Surfaces.* Journal of Biomedical Materials Research, 2003. 66A: p. 483-490.

38. Quarles L.D., Yohay D.A., Lever L.W., Caton R., and Wenstrup R.J., *Distinct proliferative and differentiated stages of murine MC3T3-E1 cells in culture: an in vitro model of osteoblast development.* J Bone Miner Res, 1992. 7(6): p. 683-692.

39. Sudo H., Kodama H., Magai Y., Yamamoto S., and Kasai S., *In vitro differentiation and calcification in a new clonal osteogenic cell line derived from newborn mouse calvaria.* J Cell Biol, 1983. 96: p. 191-198.

40. Stein G.S., Lian J.B., and Owen T.A., *Relationship of cell growth to the regulation of tissue-specific gene expression during osteoblast differentiation.* FASEB Journal, 1990. 4(13): p. 3111-3123.

41. Malaval L., Liu F., Roche P., and Aubin J.E., *Kinetics of Osteoprogenitor Proliferation and Osteoblast Differentiation In Vitro.* Journal of Cellular Biochemistry, 1999. 74: p. 616-627.

42. Brooks B.P., Qiao M., Howell D.S., and Boyan B.D., *Matrix vesicles produced by osteoblast-like cells become significantly enriched in proteoglycan-degrading metalloproteinases after addition of beta-glycerophosphate and ascorbic acid.* Calcif. Tissue. Int., 1994. 54(399-408).

43. Malaval l., Modrowski D., Gupta A.K., and Aubin J.E., *Cellular expression of bone-related proteins during in vitro osteogenesis in rat bone marrow stromal cell cultures.* J. Cell Physiol., 1994. 158: p. 555-572.

44. Datta A., Shi Q., and Boettiger D.E., *Transformation of chicken embryo fibroblasts by v-src uncouples β1 integrin-mediated outside-in but not inside-out signaling.* Molecular and Cellular Biology, 2001. 21(21): p. 7295-7306.

45. Mizuno M., Kuboki Y., *Osteoblast-Related Gene Expression of Bone Marrow Cells during the Osteoblastic Differentiation Induced by Type I Collagen.* J. Biochem., 2001. 129: p. 133-138.

46. McGee-Russel S.M., *Histochemical methods for calcium.* J. Histochem Cytochem, 1958. 6: p. 22-42.

47. Dickson G.R., *Methods of calcified tissue preparation*. 1984, New York: Elsevier. 764.

48. Schakeraad J.M., Busscher H.J, Wildevuur C.R., and Arends J., *The influence of substratum surface free energy on growth and spreading of*

human fibroblasts in the presence and absence of serum proteins. J Biomed Mater Res, 1986. 20(773-784).

49. Webb K., Hlady V., and Tresco P.A., *Relative importance of surface wettability and charged functional groups on NIH 3T3 fibroblast attachment, spreading, and cytoskeletal organization.* J Biomed Mater Res, 1998. 41: p. 422-430.

50. Altankov G., Grinnell F., and Groth T., *Studies of the biocompatibility of materials: Fibroblast reorganization of substratum-bound fibronectin on surfaces varying in wettability.* J Biomed Mater Res, 1996. 30: p. 385-391.

51. Altankov G., Thom V., Groth T., Jankova K., Jonsson G., and Ulbricht M., *Modulating the biocompatibility of polymer surfaces with poly(ethylene glycol): Effect of fibronectin.* J Biomed Mater Res, 2000. 52: p. 219-230.

52. Stephansson S.N., Byers B.A., and García A.J., *Enhanced expression of the osteoblastic phenotype on substrates that modulate fibronectin conformation and integrin receptor binding.* Biomaterials, 2002. 23: p. 2527-2534.

53. García A., Vega M.D., and Boettiger D., *Modulation of Cell Proliferation and Differentiation through Substrate-dependent Changes in Fibronectin Conformation.* Molecular Biology of the Cell, 1999. 10: p. 785-798.

54. van Wachem P.B., Beugeling T., Feijen J., Bantjes A., Detmers J.P., and van Aken W.G., *Interactions of cultured human endothelial cells with polymeric surfaces of different wettabilities.* Biomaterials, 1985. 6: p. 403-408.

55. Girard P.R., Nerem R.M., *Shear stress modulates endothelial cell morphology and F-actin organization through the regulation of focal adhesion-associated proteins.* Journal of Cellular Physiology, 1995. 163: p. 179-193.

56. Ben-Ze'ev A., Robinson G.S., Bucher N.L.R., and Farmer S.R., *Cell-cell and cell-matrix interactions differentially regulate the expression of hepatic and cytoskeletal genes in primary cultures of rat hepatocytes.* Proc. Natl. Acad. Sci. USA, 1988. 85: p. 2161-2165.

57. Wilkinson M.H.F., Schut F., ed. *Digital Image Analysis of Microbes: Imaging, morphometry, fluorometry and motility techniques and applications*. 1st ed. 1998, John Wiley & Sons: West Sussex. 551.

58. Washburn N.R., Yamada K.M., Simon Jr. C.G., Kennedy S.B., and Amis E.J., *High-throughput investigation of osteoblast response to polymer crystallinity: influence of nanometer-scale roughness on proliferation.* Biomaterials, 2004. 25: p. 1215-1224.

59. Cornet F., Anselme K., Grard T, Rouahi M, Noël B, Hardouin P, and Jeanfils J., *The influence of culture conditions on extracellular matrix proteins*

synthesized by osteoblasts derived from rabbit bone marrow. **J Biomed Mater Res, 2002. 63: p. 400-407.**

CHAPTER V

CONCLUSION

One of the primary challenges in developing tissue-engineered devices is culturing anchorage-dependent cells on synthetic materials while maintaining their differentiated properties and functions. This involves an exhaustive evaluation of multiple material properties (i.e., surface chemistry) and their effect on cell response. One of such properties is surface topography. Surface topography, however, has not been fully exploited as a tool to engender desired biological responses and is generally neglected or relegated to a second plane by typical approaches that focus chiefly on surface chemistry and its effect on cell behavior. This study was structured to gain a better understanding on the role of surface structure and morphology in cell behavior, and uncover the potential of applying surface topography in innovative ways to improve biomaterials design.

Combinatorial techniques were used to successfully create libraries of blends of the FDA approved degradable polymers PCL and PDLA, obtaining thousands of dissimilar surface microstructures resulting from the blend's LCST phase behavior. These controllable morphologies encompassed a great range of distinct roughness and domain sizes that allowed rapid identification of the effect of surface features on different cell events.

Reaction of MC3T3-E1 immature osteoblasts to surface topography was evident as there were marked differences in their response across the combinatorial libraries for a given assay. Optimal process conditions were found to be different from one cell event to the other, suggesting that dissimilar surface characteristics influence cell behavior

differently depending on the cell developmental state, i.e., the temperature-composition regime of enhanced cell spreading was different from that of enhanced proliferation. MC3T3-E1 cells, particularly, were positively influenced by low to middle roughness levels (85 to 177 nm) and middle sized domains (20 to 40 μm), suggesting a maximum tolerable amount of phase separation.

The ability shown by combinatorial techniques to characterize complex cell-surface systems in a rapid fashion, allowing finding optimal topography characteristics to elicit specific effects on cells, gives a new perspective to biomaterial design as new surfaces can be engineered to target particular cell events (i.e., proliferation, protein expression, etc), taking advantage of the exceptional sensitiveness of cells to surface morphology.

CHAPTER VI

RECOMMENDATIONS AND FURTHER WORK

Further surface characterization is essential for a better understanding of the underlying relationship between cell behavior and surface morphology. Surface properties such as roughness and microstructure size, addressed in this work, must be coupled with microdomain dispersion (distribution), in order to ascertain the impact of the degree of separation between chemically identical domains on cell attachment and function. It is worth mentioning that wide ranges of surface roughness, microstructure size, and microdomain distribution can be achieved and analyzed by varying annealing times and temperatures. Recent studies have shown that cells are extremely sensitive to nanometric-scale features, maybe even more than to micrometric-scale structures. Hence, a major improvement to this study, as it would impart a more detailed description of surface morphology, would be to assess the effect of dispersed sub-micron structures of one polymer into microdomains of the other (i.e., minute PDLA sub-micron domains dispersed inside PCL-rich microstructures –polarized micrographs, section 3.3.4.2–) on cell function.

Correlation between cell behavior and surface morphology has been obtained by linking library areas with enhanced cell response with the properties of the “same” areas over separately characterized libraries. A plausible approach to better the approximation of cell-surface interactions would be to utilize the *same* microscope to evaluate microstructure size and distribution (cross-polarized microscopy), and cell characteristics (immunofluorescence microscopy). In this way, particular cell responses can be associated directly with the morphology of the surface precisely underneath the cells,

leaving roughness as the only indirectly evaluated surface feature. Thorough validation of results obtained from combinatorial procedures has to be carried out on single composition samples, followed by proper statistical analysis. This includes both, surface properties of particular composition-temperature regimes and cell response over those regimes. Regarding immunofluorescence assays, it is imperative to modify the actual methodology and use secondary antibodies with higher signal-to-noise ratio (i.e., antibodies with emission wavelengths between 600 and 650 nm), to avoid visualization hindrance due to polymer autofluorescence (as experienced during vinculin staining to localize focal adhesion clusters). Antibody leakage has to be taken into account as well when selecting secondary antibodies.

Future work should address the impact of surface chemistry by evaluating adsorption of adhesive proteins (i.e., fibronectin) over chemically distinct domains and their biological activity, that is, protein conformational changes (denaturation) and protein orientation. Moreover, new combinatorial approaches should attempt to decouple chemistry and morphology effects on cell function. Blends of polymers with comparable biological activity, coatings, or crystallinity gradients are a few examples of alternatives that can be explored to achieve this.

Intercellular or paracrine signaling is an important factor on cell function that was left unexplored in this work. Paracrine signals are generated by local mediators released by cells into the extracellular medium in their neighborhood; these signals act locally on contiguous cells having a noteworthy effect on their overall function. Systematic inhibition of these signals will allow investigating their role on the cell-surface interactions observed across the combinatorial libraries.

Due to their own nature, combinatorial methods and high throughput screening techniques generate enormous amounts of data. The use of appropriate tools for data manipulation and analysis such as databases and datamining can markedly ease and

improve the process of converting collected data into useful information. Datamining, specifically, can be used as a powerful instrument to find trends and patterns inside big collections of datasets that otherwise would have been be overlooked.

Finally, once an adequate knowledge of cell-surface interactions is achieved, further complementary work could couple required mechanical properties with cell response-enhancing process conditions to obtain biomaterials with optimal characteristics. Supplementary research can also focus on combinatorial three-dimensional (foams) polymer supports that promote cell adhesion and support cell growth, proliferation, and differentiation.

APPENDIX A

POLYMER BLEND MASS BALANCE

The following appendix contains the detailed mass balance derived from equation 3.1, and supports the assumptions made to obtain linear composition gradients.

Table A.1. Initial values for the mixing step of the combinatorial library preparation procedure.

INITIAL VALUES		
Sample time (sec)	62.00	
Initial volume (ml)	1.00	PDLA
$X_{B,0}$ (vial)	0.05	PDLA
Sampling volume (μl)	84.00	Gradient
Withdrawal rate (ml/min)	1.50	Mix
$X_{A,0}$ (infusion)	0.05	PCL
Chip size (mm)	24.00	

Table A.2. Calculated rates based on the initial values presented in table A.1 (infusion rate equals the average between the sampling and withdrawal rates, as stated in section 3.2.1).

CALCULATED VALUES		
Withdrawal volume (ml)	1.550	mix
Sampling rate (ml/min)	0.081	Gradient
Infusion rate for linear gradient (ml/min)	0.791	PCL
Infused volume (ml)	0.817	PCL

Calculated values of the PCL and PDLA mass fractions inside the vial as a function of time (equation 3.2) are presented in table A.3 (A→PCL, B→PDLA).

Table A.3. PCL and PDLA mass fractions inside the mixing vial as a function of time.

Time (sec)	$X_{B,t}$ (vial)	$X_{A,t}$ (vial)	Time (sec)	$X_{B,t}$ (vial)	$X_{A,t}$ (vial)
0	0.05	0	32	0.0289161	0.0210839
1	0.0493411	0.0006589	33	0.0282573	0.0217427
2	0.0486823	0.0013177	34	0.0275984	0.0224016
3	0.0480234	0.0019766	35	0.0269395	0.0230605
4	0.0473645	0.0026355	36	0.0262806	0.0237194
5	0.0467056	0.0032944	37	0.0256218	0.0243782
6	0.0460468	0.0039532	38	0.0249629	0.0250371
7	0.0453879	0.0046121	39	0.024304	0.025696
8	0.044729	0.005271	40	0.0236452	0.0263548
9	0.0440702	0.0059298	41	0.0229863	0.0270137
10	0.0434113	0.0065887	42	0.0223274	0.0276726
11	0.0427524	0.0072476	43	0.0216685	0.0283315
12	0.0420935	0.0079065	44	0.0210097	0.0289903
13	0.0414347	0.0085653	45	0.0203508	0.0296492
14	0.0407758	0.0092242	46	0.0196919	0.0303081
15	0.0401169	0.0098831	47	0.0190331	0.0309669
16	0.0394581	0.0105419	48	0.0183742	0.0316258
17	0.0387992	0.0112008	49	0.0177153	0.0322847
18	0.0381403	0.0118597	50	0.0170565	0.0329435
19	0.0374815	0.0125185	51	0.0163976	0.0336024
20	0.0368226	0.0131774	52	0.0157387	0.0342613
21	0.0361637	0.0138363	53	0.0150798	0.0349202
22	0.0355048	0.0144952	54	0.014421	0.035579
23	0.034846	0.015154	55	0.0137621	0.0362379
24	0.0341871	0.0158129	56	0.0131032	0.0368968
25	0.0335282	0.0164718	57	0.0124444	0.0375556
26	0.0328694	0.0171306	58	0.0117855	0.0382145
27	0.0322105	0.0177895	59	0.0111266	0.0388734
28	0.0315516	0.0184484	60	0.0104677	0.0395323
29	0.0308927	0.0191073	61	0.0098089	0.0401911
30	0.0302339	0.0197661	62	0.00915	0.04085
31	0.029575	0.020425			

Figure A.1 depicts the linear evolution of the PCL and PDLA mass fractions presented in table A.3. The only requirement for this linear behavior is that the infusion rate of PCL equals the average of the sampling and withdrawal rates.

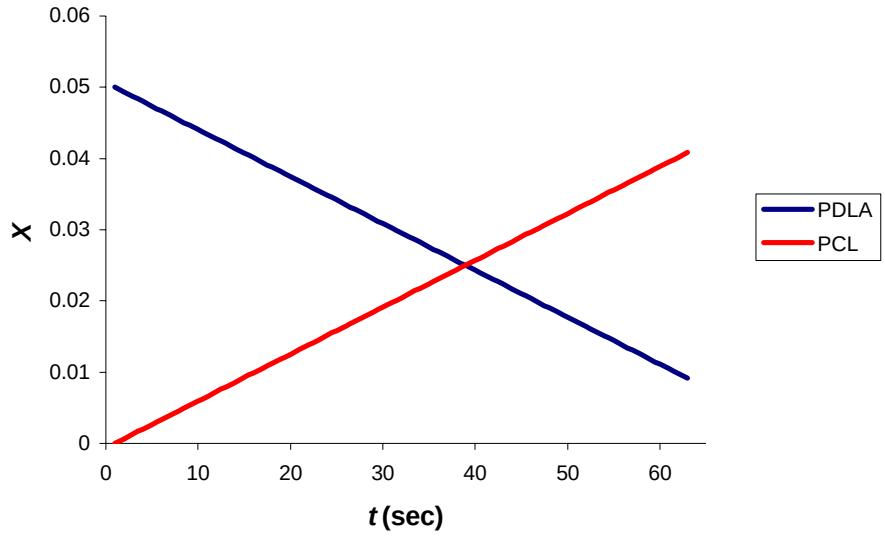

Figure A.1. Evolution of PCL and PDLA mass fractions during the mixing step.

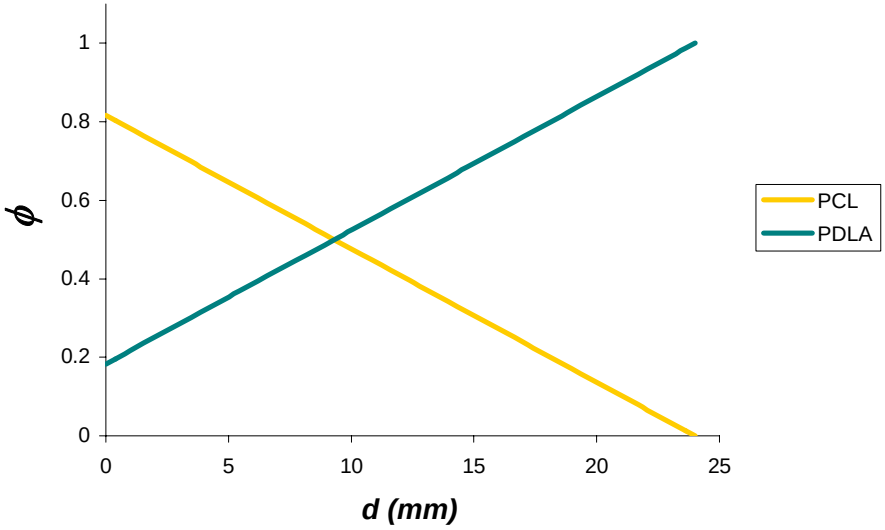

Figure A.2. Relative PCL and PDLA mass fractions over a 24 x 24 mm silicon substrate as a function of position. $X_{A,0} = X_{B,0} = X_0 = 0.5$ (PCL and PDLA solutions with identical mass fractions).

Relative mass fractions calculated using equation 3.5 are tabulated in table A.4. The respective linear PCL/PDLA gradient profile created over the silicon substrate is shown in figure A.2.

Table A.4. PCL and PDLA relative mass fractions after film casting.

Position on chip (mm)	$\phi_{B,t}$ (chip)	$\phi_{A,t}$ (chip)	Position on chip (mm)	$\phi_{B,t}$ (chip)	$\phi_{A,t}$ (chip)
24	1	0	11.61290323	0.5783226	0.4216774
23.61290323	0.9868226	0.0131774	11.22580645	0.5651452	0.4348548
23.22580645	0.9736452	0.0263548	10.83870968	0.5519677	0.4480323
22.83870968	0.9604677	0.0395323	10.4516129	0.5387903	0.4612097
22.4516129	0.9472903	0.0527097	10.06451613	0.5256129	0.4743871
22.06451613	0.9341129	0.0658871	9.677419355	0.5124355	0.4875645
21.67741935	0.9209355	0.0790645	9.290322581	0.4992581	0.5007419
21.29032258	0.9077581	0.0922419	8.903225806	0.4860806	0.5139194
20.90322581	0.8945806	0.1054194	8.516129032	0.4729032	0.5270968
20.51612903	0.8814032	0.1185968	8.129032258	0.4597258	0.5402742
20.12903226	0.8682258	0.1317742	7.741935484	0.4465484	0.5534516
19.74193548	0.8550484	0.1449516	7.35483871	0.433371	0.566629
19.35483871	0.841871	0.158129	6.967741935	0.4201935	0.5798065
18.96774194	0.8286935	0.1713065	6.580645161	0.4070161	0.5929839
18.58064516	0.8155161	0.1844839	6.193548387	0.3938387	0.6061613
18.19354839	0.8023387	0.1976613	5.806451613	0.3806613	0.6193387
17.80645161	0.7891613	0.2108387	5.419354839	0.3674839	0.6325161
17.41935484	0.7759839	0.2240161	5.032258065	0.3543065	0.6456935
17.03225806	0.7628065	0.2371935	4.64516129	0.341129	0.658871
16.64516129	0.749629	0.250371	4.258064516	0.3279516	0.6720484
16.25806452	0.7364516	0.2635484	3.870967742	0.3147742	0.6852258
15.87096774	0.7232742	0.2767258	3.483870968	0.3015968	0.6984032
15.48387097	0.7100968	0.2899032	3.096774194	0.2884194	0.7115806
15.09677419	0.6969194	0.3030806	2.709677419	0.2752419	0.7247581
14.70967742	0.6837419	0.3162581	2.322580645	0.2620645	0.7379355
14.32258065	0.6705645	0.3294355	1.935483871	0.2488871	0.7511129
13.93548387	0.6573871	0.3426129	1.548387097	0.2357097	0.7642903
13.5483871	0.6442097	0.3557903	1.161290323	0.2225323	0.7774677
13.16129032	0.6310323	0.3689677	0.774193548	0.2093548	0.7906452
12.77419355	0.6178548	0.3821452	0.387096774	0.1961774	0.8038226
12.38709677	0.6046774	0.3953226	0	0.183	0.817
12	0.5915	0.4085			

Figure A.3 shows the effect of using polymer solutions with dissimilar mass fractions. The polymer mass fraction evolution during the mixing step remains linear as the infusion rate is not affected by changes in the composition of the polymer solutions. However, the relative mass fraction of each polymer is greatly affected once the solvent has evaporated after casting the library film, supporting the requirement of solutions of equal mass fraction to prepare libraries with linear composition gradients.